

DISSERTATION

GPS EQUATORIAL IONOSPHERIC SCINTILLATION SIGNALS SIMULATION,
CHARACTERIZATION, AND ESTIMATION

Submitted by

Dongyang Xu

Department of Electrical and Computer Engineering

In partial fulfillment of the requirements

For the Degree of Doctor of Philosophy

Colorado State University

Fort Collins, Colorado

Summer 2019

Doctoral Committee:

Advisor: Yu Morton

Charles Rino
Frank van Graas
Olivier Pinaud

Copyright by Dongyang Xu 2019

All Rights Reserved

ABSTRACT

GPS EQUATORIAL IONOSPHERIC SCINTILLATION SIGNALS SIMULATION, CHARACTERIZATION, AND ESTIMATION

Strong equatorial ionospheric scintillation is characterized with simultaneous deep amplitude fading and fast phase fluctuations, which can severely degrade GNSS receiver performance and impact a variety of GNSS applications. This dissertation addresses the equatorial ionospheric scintillation effects on GNSS signals in three aspects: simulation, characterization, and estimation. The first part of the dissertation presents a physics-based, strong scintillation simulator that requires only two scintillation indicators as input parameters, with validation results using a large amount of real scintillation data. In order to improve the accuracy of carrier phase estimation, a semi-open loop algorithm is developed in the second part of the dissertation. The performance of this algorithm is evaluated using the developed simulator against two other state-of-the-art algorithms and shows improved performance in terms of reduced cycle slip occurrences and estimation error. In the third part, the scintillation signal characterization is conducted using a large amount of real strong scintillation data from Ascension Island. Statistical summaries are obtained, including the temporal characteristics of and correlation between fast phase changes and deep fades and the statistical relationship between the data bit decoding error occurrences and the intensity of amplitude scintillation.

ACKNOWLEDGEMENTS

My sincere thanks and gratitude to the following people for their assistance, support, and kindness during my PhD study:

My advisor, Dr. Jade Morton, for her patient mentoring, insightful guidance, and unwavering support during my master's and PhD research. Her work ethic and generosity have demonstrated an exemplary researcher to me and my fellow students.

One of my committee members, Dr. Charles L. Rino, for his patient tutoring and thoughtful help during my PhD research. It was his generosity in sharing his knowledge and code that made part of this dissertation possible.

All my other committee members, Dr. Frank van Graas and Dr. Olivier Pinaud, for their help and constructive advice in my PhD exams.

My current and past colleagues and friends in the CSU GPS Lab and CU SeNSE Lab, Rong Yang, Yu Jiao, Zhe Yang, Steve Taylor, Harrison Bourne, Jun Wang, Yang Wang, Yunxiang Liu, Pai Wang, Brian Breitsch, Ian Collett, and Bo Han, for their kindness, loyalty, and support that make us an intimate group.

My parents for their unconditional love and support during my life here in the U.S.

My PhD research is funded through startup grants from Colorado State University and University of Colorado Boulder, and a grant from NASA (NNX15AT54G).

TABLE OF CONTENTS

ABSTRACT.....	ii
ACKNOWLEDGEMENTS	iii
LIST OF TABLES	vii
LIST OF FIGURES	viii
1. CHAPTER 1 –INTRODUCTION	1
1.1. Background	1
1.2. Ionospheric Scintillation Indicators	3
1.3. Literature Research	4
1.3.1. Previous Research on GNSS Scintillation Signal Simulation	4
1.3.2. Previous Research on GNSS Scintillation Signal Characterization	6
1.3.3. Previous Research on Signal Estimation during Strong Equatorial Scintillation	7
1.4. Motivations and Contributions of Dissertation Research	12
1.4.1. Development of a Two-parameter Scintillation Signal Simulator.....	13
1.4.2. Algorithm Development and Evaluation Using Simulated Data	15
1.4.3. Scintillation Signal Characterization	16
1.5. Dissertation Outline.....	18
2. CHAPTER 2 – GPS CIVIL SIGNALS	19
2.1. GPS Signal Structures	19
2.2. PRN Code Properties	23
3. CHAPTER 3 – A TWO-PARAMETER SIGNAL SIMULATOR FOR STRONG EQUATORIAL SCINTILLATION.....	26
3.1. Scintillation Signal Simulator Routine Description.....	26
3.2. Phase Screen Realization and Wave Propagation	30
3.3. Parameter Estimation	34
3.3.1. IPE.....	34
3.3.2. S_4 and τ_0 Calculation.....	37
3.4. Data Description.....	37
3.5. Real Data Analysis	40
3.5.1. IPE Triple-frequency Consistency Evaluation.....	40
3.5.2. Spectral Parameter Characterization.....	45
3.5.3. Parameter Mappings and Real Data Evaluation	46
3.6. Concluding Remarks on Simulator Development.....	52
4. CHAPTER 4 – DEVELOPMENT AND EVALUATION OF ADVANCED CARRIER TRACKING ALGORITHMS FOR SCINTILLATION SIGNALS.....	54
4.1. Fundamentals of GNSS Receiver Processing	54
4.1.1. Correlators.....	58
4.1.2. Discriminators.....	59
4.1.3. Loop Filters	61
4.1.4. KF and the State-space Representation.....	62
4.1.5. Ionospheric Scintillation Measurements.....	65
4.2. Overview of Advanced Carrier Tracking Algorithms.....	67
4.3. SOL	69

4.3.1.	Propagation Time Prediction	71
4.3.2.	Carrier Doppler Prediction.....	73
4.3.3.	Moving Window Processing.....	74
4.3.4.	SOL Carrier Phase and Signal Intensity Estimation	75
4.3.5.	VDFLL Implementation	76
4.4.	OT.....	80
4.5.	AR	83
4.5.1.	AR Scintillation Amplitude and Phase Models	83
4.5.2.	AR State and Measurement Models	85
4.6.	Simulation Evaluations for SOL, OT, and AR.....	87
4.6.1.	Stationary Platform Data Set	87
4.6.2.	Dynamic Platform Data Set	91
4.7.	Simulation Evaluations for Different VDFLL Implementations	94
4.7.1.	Different Satellite-weighting Implementations.....	94
4.7.2.	Simulation Configuration.....	96
4.7.3.	Evaluation Results	99
4.8.	Concluding Remarks	102
5.	CHAPTER 5 – SIMULATING AND TRACKING SCINTILLATION SIGNALS ON LEO SATELLITES	104
5.1.	Scintillation Signal Simulation on LEO Satellites	104
5.1.1.	LEO Propagation Geometry Setup	105
5.1.2.	Simulation Results for Different LEO Scenarios.....	107
5.2.	Scintillation Signal Tracking on LEO Satellites	111
5.2.1.	Tracking Results of Scenario 1 (b)(c).....	112
5.2.2.	Tracking Results of Scenario 2.....	115
5.3.	Concluding Remarks on LEO Scintillation Signal Simulation.....	116
6.	CHAPTER 6 – RESULTS ON SCINTILLATION SIGNALS CHARACTERIZATION..	117
6.1.	Scintillation Data Collection System	117
6.2.	Characterization on Deep Fading and Fast Phase Changes	118
6.2.1.	Comparison of Real Data Tracking Results Using SOL and Conventional PLL ..	119
6.2.2.	Fast Phase Changes and Deep Fading Statistical Summary	121
6.3.	Characterization on GPS L1 BDE.....	126
6.3.1.	GPS L1 Bit Decoding Error Example.....	126
6.3.2.	BDE Processing Results and Statistical Analysis.....	129
6.4.	Concluding Remarks on Scintillation Signal Characterization.....	134
7.	CHAPTER 7 – CONCLUSION.....	135
	REFERENCES	137
	APPENDIX: SIMULATOR PROGRAM CONFIGURATION AND EXECUTION	148

LIST OF TABLES

Table 2-1 GPS signal structure information [US Air Force, 2012, 2013]	20
Table 2-2 List of GPS satellites of three blocks	20
Table 2-3. Auto-correlation $R \cdot$ and cross-correlation $C \cdot$ isolation for different civil signals [Tran and Hegarty, 2002]	24
Table 4-1. The $S4$ and $\tau0$ values (on L1) for the three scenarios of scenario set 1	88
Table 4-2. The receiver velocity vectors, $S4$ and resulting $\tau0$ values on the L1 signal in four simulated dynamic scenarios	91
Table 4-3. Three configurations of scintillation satellites used in the simulation of evaluation data	97
Table 4-4. RMSE results using three VTL implementations for three configurations of simulated data	100
Table 4-5. RMSE results using VTL2 and VTL3 for the simulated data with amplitude fading and no scintillation phase	102
Table 5-1. Different scenarios of geometric and dynamics setup and the resulting rp and $\rho F/v_{eff}$ values	106
Table 5-2. Summary of occurrences of cycle slip and RMSE for the tracking results using AKF-1ms and 5ms in all 10 realizations of data of Scenario 1 (b) and (c)	114
Table 5-3. Summary of total occurrences of cycle slip and RMSE in the carrier tracking of 10 realizations of data of Scenario 2 using the 10Hz-PIF implementations and the AKF implementations with all three integration times	115
Table 6-1. Summary of number of fades and fast phase changes occurred in the Ascension Island data	122
Table 6-2 Duration of phase changes of full cycles and of combined full and half cycles	124
Table 6-3 Percentage of fades and concurrent fast phase changes within four different ranges of minimum C/N_0 values for the scintillation data listed in Table 6-1	125
Table 6-4. Summary of the number of BDE and the amplitude scintillation parameters during the selected scintillation periods in the Ascension Island data	129
Table 6-5. Number and percentage of the $S4$ estimate samples and of the BDE, and the probability of BDE occurrence under different $S4$ levels	131
Table 6-6. Number and percentage of the fades and of the BDE, and the probability of occurrence under different fading levels	132

LIST OF FIGURES

Figure 1-1. Relationships of the three major topics in this dissertation.....	12
Figure 1-2. Illustration of contribution part 1 in this dissertation, which is the development of a two-parameter scintillation signal simulator.....	14
Figure 1-3. Illustration of contribution part 2 in this dissertation, which is algorithm development and evaluation using simulated data.	15
Figure 1-4. Illustration of contribution part 3 in this dissertation.....	17
Figure 2-1. GPS L1 C/A signal structure.....	20
Figure 2-2. GPS C/A-Code Correlation Functions. The L1 C/A auto-correlation isolation and cross-correlation isolation are both better than $20\log_{10}(65/1023) = -23.9\text{dB}$	24
Figure 3-1. Flow chart of the scintillation signal simulator. The parallelograms on the left side depict the parameters to be specified by users, while the rectangular components are the different steps within the scintillation simulation. The simulator outputs IF samples of GNSS scintillation signal.	27
Figure 3-2. 50-minute processing results on March 5, 2014 in Hong Kong with strong scintillation observed on all three frequencies on GPS PRN 1, starting at 13:27:00 UTC. The triangles mark the center of each 5-minute segment that the intensity results are divided into. ..	38
Figure 3-3. SDF and ACF for intensity scintillations observed on GPS triple-frequency signals from segment 7 in Figure 3-2. The SDFs and AFCs for the measurements are shown in blue, while those for the fitted model are shown in red. The dashed, double-sided arrow on each top panel indicates the frequency range over which the IPE fitting was performed.	40
Figure 3-4. The inter-frequency relationships for all five parameters, each with three pairs (L1-L2, L1-L5, and L2-L5). Real data results are plotted in blue markers, and the least-square-fitted and the model-prescribed ones are in red and black, respectively. The correlation coefficients, the differences in the slope (Δa) and offset (Δb) between the linear-fitted and the model relationships are also listed.....	44
Figure 3-5. Distributions of the IPE-estimated spectral parameters from the three data groups (group 1 in green, group 2 in blue, and group 3 in red), with the mean values listed in the legends.	46
Figure 3-6. The numerically evaluated relationship (denoted as model, in red) and the scatter plot of the $S4$ index and U estimates from the combined scintillation data set (denoted as data, in black markers), as well as the relationship that resulted from fitting the $p1, p2, \mu0$ to optimal values that satisfy the LSE criteria w.r.t the data (denoted as fitted, in blue).....	48
Figure 3-7. The numerically evaluated relationships between $\tau0$ and ρFv_{eff} color coded w.r.t the corresponding U values.....	49
Figure 3-8. The scatter plot of the $\tau0$ versus ρFv_{eff} estimates from the four categories of the real data distinguished by color and marker shapes. The numerical relationship conditioned on the mean U value of each data category is plotted as a straight line in the same color as the corresponding category. The U range and its mean value of each data category are listed in the legend.....	50
Figure 3-9. Comparison of the signal intensity in the simulated data and real data.	51
Figure 4-1. A fundamental GNSS receiver.....	55
Figure 4-2. STL-based receiver architecture.	56

Figure 4-3. Internal structure of a conventional STL.	57
Figure 4-4. Block diagram of a traditional (a) PLL/FLL and (b) DLL.....	58
Figure 4-5. Three carrier phase estimation approaches, i.e., SOL, OT, and AR. The shared components are plotted in black, while the components of different approaches are plotted in green, blue, and red for SOL, OT, and AR, respectively. The dashes lines indicate inputs obtained from other frequencies (for OT) or satellites (for SOL).	68
Figure 4-6. SOL-based SDR receiver architecture used in this study. The box with the dashed outline is the moving window processing procedure [Xu <i>et al.</i> , 2015].....	69
Figure 4-7. Illustration of propagation time prediction used in the SOL algorithm for a stationary receiver platform [Xu and Morton, 2015].....	71
Figure 4-8. Illustration of Δt^2 linear approximation procedure in SOL algorithm. The dotted slant line indicates transmission times of the signal received at the corresponding receiving times marked on the horizontal axis [Xu and Morton, 2015].....	73
Figure 4-9. SOL moving window processing diagram. Moving window integration is performed on the recorded 1-ms correlator outputs with NWM -ms window size and 1-ms step in this study. The MW integration outputs are then sent to calculate SI_{norm} and $d\phi$	75
Figure 4-10. Vector tracking architecture used in this thesis. An EKF is implemented as the navigation filter in the receiver VDFLL structure. The bar accent ‘-’ denote discriminator outputs/measured quantities, whereas the hat accent ‘^’ denotes predicted quantities.	77
Figure 4-11. Sample PAF of $\delta\phi$ (left panel) and δA (right panel) under scintillation scenario $\{S_4=0.9, \tau_0=1.5s\}$ for AR model order selection.	84
Figure 4-12. SDF of $\delta\phi$ (left panel) and δA generated under scintillation scenario $\{S_4=0.9, \tau_0=1.5s\}$ and of the realizations generated with fitted AR model.....	85
Figure 4-13. Examples of triple-frequency SI (left panels) and $\delta\phi$ (right panels) of the three scenarios (1a in top row, 1b in middle row, and 1c in bottom row). The results of different frequencies are plotted in different colors: L1 in blue, L2 in green, and L5 in red.	88
Figure 4-14. Zoom-in of the SI in Scenario 1a.	89
Figure 4-15. Cycle slip occurrence rate (per minute) and RMSE on ϕ_s using different algorithms for Scenario 1a-c.	90
Figure 4-16. Simulated Doppler for the four dynamic scenarios.....	92
Figure 4-17. Cycle slip occurrence rate (per minute) on the estimation error of ϕ_s using different algorithms for Scenario 2ab and 3ab.....	93
Figure 4-18. RMSE on the estimation error of ϕ_s using different algorithms for Scenario 2ab and 3ab.	93
Figure 4-19. Sky view plots of all visible satellite (SV) tracks during 11:00 PM–12:30 AM UTC on March 10 on Ascension Island with an elevation mask of 10° . The tracks are color-coded by the values of the S_4 index on L1. The ends with PRN numbers represent the starting points of the tracks. The track segments defined by the rectangles correspond to the duration of the initialization data.....	97
Figure 4-20. The platform velocity vector during the 10-min-trajectory.	98
Figure 4-21. The simulated scintillation phase ($\delta\phi$) and SI of the 5 satellites with strong scintillation based on initialization data.....	99
Figure 4-22. Comparison between the errors in positioning (in ENU coordinates) and clock bias using the three implementations under Config. 3.	99
Figure 4-23. A segment of δf and SI results of the PRN 6 signal in the simulation data.....	101

Figure 5-1. One-dimensional illustration of the propagation geometry of the two scenarios of scintillation signals received on LEO satellites. The distance between the GPS satellite and the phase screen is greatly understated for easy visualization.....	105
Figure 5-2. Normalized SI results of the simulated data for all cases listed in Table 5-1.	108
Figure 5-3. Relationship between the average S_4 and rp under Scenario 1.....	109
Figure 5-4. $\delta\phi$ of the simulated data for all cases listed in Table 5-1.	110
Figure 5-5. The scintillation phase change rate of the simulated data for all cases listed in Table 5-1. Zoomed in between 123s and 124s.....	110
Figure 5-6. Tracked C/N_0 and phase error results using AKF with 1ms and 5ms integration time from one realization of Scenario 1 (b) and (c).....	113
Figure 6-1. Schematic diagram of the wideband reconfigurable multi-GNSS data collection system setup at Ascension Island on March 7-10, 2013 [<i>Xu and Morton, 2017</i>].....	118
Figure 6-2. March 8th data tracking result examples using three tracking methods, showing deep fades associated with different kinds of fast phase changes. Results in (a) and (b) are from L1 signal on PRN 31, occurred at UTC 23:18:13 and 23:15:05, respectively, while (c) shows L5 results on PRN 24, occurred at UTC 20:58:41.	120
Figure 6-3. Comparison of duration distributions of half-cycle phase changes between signals across GPS bands.....	124
Figure 6-4. Comparison of fading duration distributions between extremely deep fades (minimum C/N_0 below 5 dB-Hz) with and without phase changes.....	126
Figure 6-5. BDE example processed using PIF and AKF-based algorithms on GPS PRN 6 L1 signal at Ascension Island, starting at 22:29:16 UTC.....	128
Figure 6-6. Relationships between the BDE frequency of occurrence and the average S_4 results (left panel) and the number of fades per minute (right panel) derived from the processing results of 14 hours of scintillation data.	130
Figure 6-7. Distribution of the extremely deep fades ($C/N_0, SI < 5B$ -Hz) w.r.t. the number of BDE occurred during each of them.	133
Figure 6-8. Relationship between the number of BDE occurred during an extremely deep fade and the corresponding fading duration	133

1. CHAPTER 1 –INTRODUCTION

The subject of this PhD dissertation is equatorial ionospheric scintillation effects on Global Navigation Satellite System (GNSS) signals and mitigation techniques for GNSS receivers. This chapter begins by giving an introduction to equatorial ionospheric scintillation phenomenon, and its challenges on GNSS receiver processing and applications. The research on the subject of this dissertation were conducted around three main topics: realistic and user-friendly simulation tools, receiver signal processing techniques that can mitigate the scintillation effects, and characterization of the scintillation effects in GNSS signals. In addition, previous related research is presented, and the motivations and contributions of this PhD dissertation are clarified.

1.1. Background

Plasma irregularities in the ionosphere can cause trans-ionospheric radio signal amplitude and phase fluctuations, which are collectively referred to as ionospheric scintillation [Yeh and Liu, 1982]. Ionospheric scintillation most frequently occurs in equatorial and high latitude areas, while the strongest effects are often observed in equatorial areas during the post-sunset and pre-midnight period characterized with simultaneous deep amplitude fading and fast phase fluctuations [Aarons,1982; Aarons and Basu, 1994; Jiao and Morton, 2015]. Research also shows that equatorial ionospheric scintillation is more frequent and intense around equinoxes, and subsides in the summer [Aarons, 1982; Kintner et al., 2007; Akala et al., 2015].

These combined effects degrade GNSS receiver carrier tracking performance in terms of increased error, carrier phase cycle slips, and even loss of lock of signals [Kintner et al., 2007; Seo et al., 2009; Myer and Morton, 2018]. In the real data analysis presented in [Jiao et al., 2016; Myer and

Morton, 2018], cycle slips and loss of lock are frequently observed in commercial receivers in the equatorial region, some of which can last more than two hours. In addition, plasma irregularities causing strong scintillation of signals over a large area of the sky has been reported in numerous previous studies [e.g., *Carroll and Morton, 2014; Jiao et al., 2016*]. When this happens, receivers may lose lock of multiple satellite signals simultaneously, which will degrade or disrupt navigation solutions.

The scintillation-induced performance degradation greatly impacts traditional GNSS applications, including remote sensing [*Arras et al., 2008; Buchert et al., 2015; Yue et al., 2016; Xiong et al., 2016*], high accuracy positioning [*Aquino et al., 2005; Jacobsen and Schäfer, 2012; Morton, 2014*] and applications that rely on Satellite-Based Augmentation System [*Conker et al., 2003; Seo et al., 2011a; Lee et al., 2017*], etc.

The magnitude and temporal characteristics of scintillation are not only dependent on the ionospheric irregularity structures and dynamics. They are also dependent on the receiver platform trajectories. Most of the previous studies have focused on stationary ionospheric monitoring receivers. In recent years, due to the popularity of low-Earth-orbit (LEO) satellite for various scientific applications, there have reports of the scintillation experienced by LEO-borne receivers. [*Buchert et al., 2015; Xiong et al., 2016; Sust et al., 2014*] reported total loss-of-lock navigation signals received from the zenith-pointing precise orbit determination (POD) antenna on the ESA Swarm satellites when travelling inside ionospheric plasma bubbles. [*Sust et al., 2014*] reported some of the loss-of-lock incidents showed strong phase scintillation with no discernable fluctuations on the carrier-to-noise ratio (C/N_0) estimation. Increased tracking error and cycle slips

occur in the LEO RO data due to the simultaneous amplitude and phase scintillation as analyzed in [Yue *et al.*, 2016]. The focus of this thesis research is on strong equatorial scintillation effects experienced by stationary and dynamic receiver platforms, their characterization, and receiver mitigation techniques. This introduction chapter will provide an overview of the basic scintillation indicators, a literature review of progresses made in relevant areas, and organization of the thesis.

1.2. Ionospheric Scintillation Indicators

The S_4 index and σ_ϕ index are the widely used indicators for amplitude and phase scintillation, respectively. S_4 is the standard deviation of the received signal power normalized to the average signal power, while σ_ϕ is defined as the standard deviation of the de-trended signal phase [Yeh and Liu, 1982]:

$$S_4 = \sqrt{\frac{\langle I^2 \rangle - \langle I \rangle^2}{\langle I \rangle^2}} \quad (1-1)$$

$$\sigma_\phi = \sqrt{\langle \phi^2 \rangle - \langle \phi \rangle^2} \quad (1-2)$$

where $\langle \cdot \rangle$ represents the average value over the interval of interest. I is the detrended signal intensity, and ϕ is the detrended carrier phase [Van Dierendonck *et al.*, 1993]. It should be noted that based on evaluation of several time intervals between 10s and 60s presented in [Pelgrum *et al.*, 2011], an average interval of 10s has been shown to best highlight the scintillation features and will be used in this study. Also a sliding window is often used, so that the rate of the indices can be as small as 1 Hz.

As a normalized indicator, S_4 typically falls into the range of 0 to 1, with values greater than 0.6 often defined as strong amplitude scintillations. The range of σ_ϕ is limited by the receiver's carrier

tracking pull-in range. For scintillation that cause phase fluctuations beyond such a range, the receiver will very likely introduce cycle slips or even lose lock of the signal, and the resulting σ_ϕ will either need to be repaired or discarded.

1.3. Literature Research

1.3.1. Previous Research on GNSS Scintillation Signal Simulation

Although in recent years, there have been increased availability of real scintillation intermediate-frequency (IF) data collected globally [Morton *et al.*, 2015a; Xu *et al.*, 2015], a scintillation simulator is still a necessary tool for the scientific, engineering, and GNSS application community to study the physical mechanism and effects of scintillation and to develop receivers that can mitigate these effects.

The scintillation models that have been studied and implemented for GNSS signal simulation include statistical models and physics-based models. Statistical models simplify the scintillation effects as a stochastic process, which is parameterized by a small number of scintillation indicators. The corresponding probability distribution functions (PDF) and spectral density functions (SDF) are obtained from empirical scintillation data through statistical analysis and spectrum shaping [Cervera and Knight, 1998; Hegarty *et al.*, 2001; Humphreys *et al.*, 2009]. The statistical modeling approaches are straightforward and simple to configure. However, these models do not preserve the information on the ionospheric irregularity structures and propagation geometry that are responsible for causing the scintillation effects observed in the empirical data [Rino *et al.*, 2018]. Therefore, they are unable to retain the correlated effects between multi-frequency scintillation, and they cannot simulate scintillation effects experienced on dynamic platforms. In addition, the

empirical-data-derived PDF and SDF of the scintillation signal amplitude may not truthfully reflect how the characteristics of the real scintillation signals vary w.r.t the scintillation strength, and they may be distorted by the receiver processing.

The physics-based scintillation models are based on theory of radio wave propagation through the ionospheric plasma structures. The most commonly used are the power-law phase screen models, which employs phase screens to abstract irregularity structures in a statistical sense and allows oblique signal propagation in an anisotropic medium. The phase screens are spectrally characterized with a power-law model, which is typically implemented as one-component or two-component power laws. The one-component power-law model was implemented and demonstrated suitable for weak to moderate scintillation simulation in [*Ghafoori and Skone, 2015; Chartier et al., 2016; Deshpande et al., 2016*], while strong equatorial scintillation effects are better captured by the two-component power-law phase screen model (TPPSM) as studied in [*Rino and Carrano, 2013; Rino et al., 2014; Carrano and Rino, 2016*]. The specification of physics-based models requires knowledge of a large number of parameters involved in the calculation of propagation geometry and the propagation signal's ionospheric piercing point (IPP) scan velocity, which made them cumbersome to work with in the past.

A compact TPPSM was presented in [*Rino et al., 2018*], where a space-to-time scaling parameter (ρ_F/V_{eff}) was introduced that can absorb all dependency on the propagation geometry and IPP scan velocity. This scaling parameter, along with a strength parameter (U), and three spectral parameters (p_1, p_2, μ_0) form the set of parameters that defines the scintillation model. Given a segment of real scintillation data, an irregularity parameter estimation (IPE) method developed in

[Carrano *et al.*, 2012a; Carrano and Rino, 2016] extracts the values of the entire parameter set to generate statistically equivalent scintillation effects. No explicit specification of the propagation geometry is needed since the geometry is already embedded in the extracted value of ρ_F/V_{eff} . This model also enabled the study of scintillation effects on GNSS signals observed on dynamic platforms such as aircraft and LEO satellites as presented in [Jiao *et al.*, 2018] and [Xu *et al.*, 2018a], respectively. In both references, $\{U, p_1, p_2, \mu_0\}$ were extracted from real scintillation data segment using the IPE to specify the ionospheric structure realization, while ρ_F/V_{eff} was calculated for various user platform dynamics to investigate the platform dynamics impact on scintillation signal propagation.

In summary, the statistical modeling approaches are straightforward and simple to configure, whereas the physics models are intrinsically more realistic but requires certain understanding of the model parameters. For users focused on developing receivers that can mitigate the adverse scintillation effects, it is much desirable that the simulator has both merits. This motivates the development of a two-parameter, physics-based scintillation simulator for receiver testing in this dissertation.

1.3.2. Previous Research on GNSS Scintillation Signal Characterization

The availability of ground-measured and in-situ scintillation data has led to data-driven methods that are focused on the statistical characterization of the scintillation signal amplitude and phase. The understanding of the scintillation signal characteristics is a pre-requisite for developing receiver techniques that can effectively mitigate ionospheric scintillation effects and for improving robustness of receiver tracking loop and navigation solution accuracy. For example, the concept of multi-frequency tracking under ionospheric scintillation was motivated by the dispersive nature

of the ionosphere and that the deep amplitude fading tends to not occur simultaneously on all frequencies transmitted from the same satellite. This finding was reported with characterization results on triple-frequency signal amplitude fading in [Jiao *et al.*, 2016].

Such understanding will enable GNSS signals to be used as a viable means to study the sources and processes that create the scintillation, or it can be directly applied to drive scintillation simulation. The statistical models discussed in the previous section are themselves products of scintillation signal characterization. The two scintillation models presented in [Cervera and Knight, 1998] and [Hegarty *et al.*, 2001] are based on the Nakagami-m distribution, which was first presented in [Nakagami, 1960] and have been found as a suitable fit for the variability of amplitude scintillation [Fremouw *et al.*, 1980; Rino, 1980]. The model presented in [Humphreys *et al.*, 2009] is based on the Rice model, which assume the in-phase and quadrature components are jointly Gaussian [Fremouw *et al.*, 1980] and therefore simplifies the simulation implementation. In addition to the PDFs of the scintillation signals, much effort has been devoted to characterizing various temporal or spectral properties of scintillation signal parameters. For instance, in [Zhang *et al.*, 2010a], the authors investigated the correlations between the amplitude and phase spectrum and the amplitude and phase scintillation indices (S_4 index and σ_ϕ), respectively. Fading characteristics and correlations among multiple frequencies were investigated in [Zhang *et al.*, 2010a; Jiao *et al.*, 2016].

1.3.3. Previous Research on Signal Estimation during Strong Equatorial Scintillation

In order to make sense of the various characterization results discussed in the previous section, it is necessary to separate artifacts of receiver signal processing from features associated with scintillation effects. Previous research has addressed some of these issues to some extent. For

example, an earlier study [Van Dierendonck, 2005] provided an insightful analysis of tracking loop filtering effects on phase scintillation indicators and proposed a means to minimize the effects by adding discriminator residuals onto filtered estimations. An inverse filtering technique is presented in [Zhang and Morton, 2013] to restore the scintillation carrier phase spectrum. Simulated scintillation signals were used in [Mao and Morton, 2013] to demonstrate receiver carrier tracking loop over-estimation of signal amplitude fading.

However, when it comes to strong scintillation, most GNSS receivers, including ionosphere scintillation monitoring (ISM) receivers, cannot maintain carrier phase measurement quality or even lock of signals [Kassabian and Morton, 2013; Xu et al., 2014; Carroll and Morton, 2014]. This explains the lack of data and studies on carrier phase variations during strong equatorial scintillation prior to the work conducted in this dissertation. The conventional GNSS carrier processing typically implements a closed loop tracking (CLT) algorithm based on the proportional integral filter (PIF) approach [Ward et al., 2005; Tsui, 2005]. The PIF discrete-time transfer function is defined by its equivalent noise bandwidth and integration time, which are in most cases empirically chosen as a compromise between the practical requirements on dynamic and noise performances under relatively benign signal conditions. Another popular CLT implementation is the Kalman filter-based (KF) algorithms [Psiaki et al., 2007; Yang et al., 2017ab]. KF is the optimal filter for signals having white Gaussian noise with *a priori* knowledge, which is not the case for strong scintillation signals. The PIF- and KF-based phase-lock loop (PLL) are actually equivalent in terms of their fundamental architectures [Driessen, 1994; Yang et al., 2017ab]. Both implementations require careful tuning of design parameters in order to track strong equatorial scintillation signals due to the conflicting demands imposed by the simultaneous deep amplitude

fading and fast carrier phase variations. While there have been a number of other CLT algorithms intended to handle scintillation in the literature, they are either not effective for strong equatorial scintillation, or there is a lack of widespread implementations of these algorithms to collect field data. For example, an adaptive KF-based PLL (AKF-PLL) is presented in [Susi *et al.*, 2014], which makes use of signal condition indicators such as the C/N_0 to adaptively adjust the KF parameters. This algorithm has only been proven efficient for moderate scintillation, because the large phase changes during strong equatorial scintillation were not addressed. An extended Kalman Filter-based (EKF) algorithm is presented in [Vilà-Valls *et al.*, 2015, 2018]. In this algorithm, scintillation-induced phase and amplitude fluctuations are included in the state-space formulation as two additional sets of variables based on autoregressive process (AR) models fitted from a scintillation signal model. All of these above algorithms are scalar tracking loops (STL) that independently tracks the signal of an individual carrier from a signal satellite.

Several algorithms based on vector processing concepts [Spilker, 1995] have also been developed to improve carrier tracking performance in the presence of ionosphere error by exploiting GNSS signal spatial diversity [Lashley *et al.*, 2009; Peng *et al.*, 2012] and/or frequency diversity [Henkel *et al.*, 2009; Yin *et al.*, 2014]. These algorithms utilize an EKF [Lashley *et al.*, 2009; Henkel *et al.*, 2009] or AKF [Peng *et al.*, 2012] as the central navigation filter, in which the receiver-generated PVT information is used as feedback to update and estimate the parameters of all tracking channels. For example, a multi-frequency vector PLL was proposed in [Henkel *et al.*, 2009] to incorporate the ionospheric delay error into the receiver state vector, and a multi-dimensional filter was used to reduce the noise in the estimated state parameters. Whereas ionospheric scintillation is indeed often associated with delay errors, the major complications lie in amplitude and carrier phase

fluctuations which were not addressed in this algorithm. An adaptive multi-frequency carrier tracking algorithm was presented in [Yin *et al.*, 2014]. As mentioned in the previous section, it utilized the dispersive nature of the ionosphere and took into consideration that deep amplitude fading tends to not occur simultaneously on all frequencies transmitted from the same satellite [Jiao *et al.*, 2016]. Doppler frequency estimations from one or two healthy frequency channels were used to infer the Doppler frequency of the fading channel from the same satellite. The fading threshold used in [Yin *et al.*, 2014] was empirically selected without theoretical investigation. A multi-frequency optimal tracking (OT) algorithm was later presented in [Yang *et al.*, 2019] that combines the measurements from different frequencies with a linear weight, which is optimized based on each carrier's signal C/N_0 .

A vector-assisted scalar tracking method was discussed in [Peng *et al.*, 2012] in which receiver-generated PVT solutions were used to only estimate and update the parameters of compromised channels. This approach prevents errors experienced in a scintillation channel from affecting tracking accuracy in other healthy channels.

An open-loop (OL) architecture designed for an ISM receiver was presented in [Curran *et al.*, 2014]. The OL architecture predicts signal parameters by making use of known receiver position and model prediction of the time correction information. The OL architecture is intrinsically robust and can thereby record measurements continuously throughout severe scintillation. However, the effectiveness of the oscillator correction models remains to be evaluated. In addition, [Curran *et al.*, 2014] only compares performance between the OL-based receiver and other commercial receivers in terms of estimated scintillation indices with coarse temporal resolutions, which did

not reflect the improvement of the OL architecture on carrier phase tracking during simultaneous deep fading and fast phase changes.

A semi-open loop (SOL) algorithm was developed based on the vector-assisted scalar tracking concept. The SOL was originally designed for a stationary platform [Xu and Morton, 2018], where the prior surveyed receiver position is used instead of the receiver-generated position, and the time solution is the only feedback to the carrier tracking loop for signal Doppler frequency prediction. In addition, the SOL approach benefits the carrier phase estimation, as its open-loop architecture allows correlation to be performed over a moving window spanning a relatively long integration period with small time increments. This moving window procedure reduces noise contribution while preserving the fine temporal structures of carrier phase estimates during a deep fade [Xu and Morton, 2018]. The SOL is later extended to a dynamic platform in [Xu et al., 2019b]. The PVT solutions are first obtained from a vector tracking loop (VTL) using healthy satellites to update the scintillation satellite parameters. The moving window procedure can then be applied in the same manner as for the stationary platform.

To sum up, much effort has been devoted to developing advanced carrier estimation methods to improve the robustness and estimation accuracy during scintillation in the literature. However, one of the challenges remains the algorithm performance validation and evaluation, as there is a lack of convincing validation results via field data and/or simulated data with realistic strong equatorial scintillation features in literature. Among the algorithms discussed above, the AR, OT, and SOL algorithms all showed respective promising features in their design for scintillation carrier tracking. However, none of the three methods have been comprehensively evaluated using a realistic strong

scintillation signal simulator. In [Yang *et al.*, 2019], OT’s effectiveness was only validated using real data, whereas AR was evaluated with simulation signals generated using the same autoregressive process-based signal model [Vilà-Valls *et al.*, 2018]. In [Xu and Morton, 2018], the SOL was evaluated using real data and only one realization of simulated scintillation data. This issue in turn motivates the development of the physics-based scintillation signal simulator in this dissertation.

1.4. Motivations and Contributions of Dissertation Research

This PhD dissertation includes three major topics: scintillation signal simulation, scintillation signal characterization, and receiver algorithm development and evaluation for better scintillation signal estimation and mitigation. The enabler of this PhD research is a large collection of real GPS scintillation data from different equatorial locations. The relationships of the three major topics are depicted in Figure 1-1. The three topics are closely related, and one assists the development of the others.

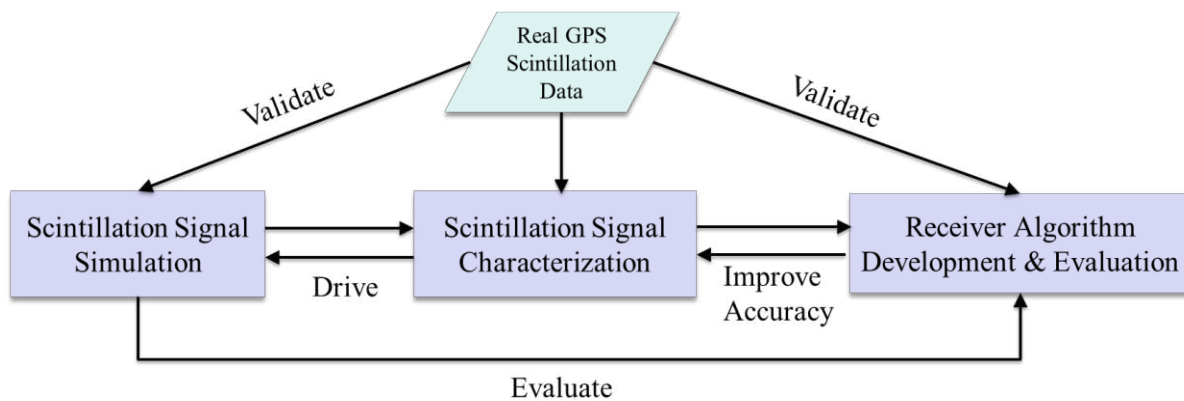


Figure 1-1. Relationships of the three major topics in this dissertation.

The real scintillation data facilitate the study of ionospheric scintillation phenomenon in various ways as discussed in previous sections. Real data is indispensable for the purpose of validating the

effectiveness of the scintillation signal simulator and receiver processing algorithms. By characterizing the statistics of real scintillation signals, a better understanding can be gained regarding the sources and processes that create the ionospheric scintillation and in turn used to drive the scintillation simulation. Such statistics is also a pre-requisite for developing receiver techniques that can effectively mitigate ionospheric scintillation effects and for improving robustness and estimation accuracy of receiver tracking loop. Simulated signals can be used to study the characteristics of scintillation signals, especially for circumstances where scintillation signals are difficult to collect, such as on a dynamic platform. Advanced receiver processing algorithms can also in turn help improve the scintillation signal characterization by providing more accurate estimation results of the scintillation signal parameters. Last but not least, the scintillation simulator is a necessary tool to comprehensively evaluate receiver algorithms under ionospheric scintillation because of its capability to create various scintillation scenarios of controlled, consistent scintillation levels and characteristics with known reference truth and statistically significant data quantity.

This dissertation's contributions can be divided into three parts and are summarized in the following sections.

1.4.1. Development of a Two-parameter Scintillation Signal Simulator

This part of contribution is illustrated in Figure 1-2.

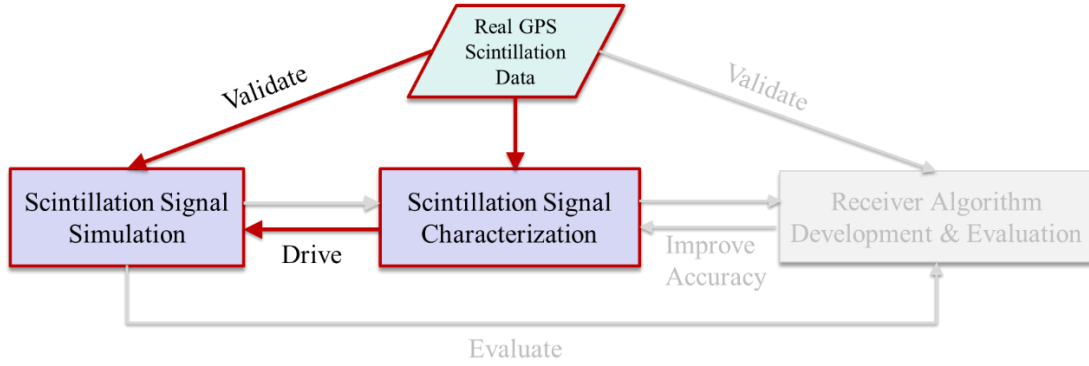


Figure 1-2. Illustration of contribution part 1 in this dissertation, which is the development of a two-parameter scintillation signal simulator.

A physics-based, multi-frequency, strong scintillation simulator has been modified to require only two input parameters: the expected scintillation index S_4 and the intensity decorrelation time τ_0 . Both parameters are widely used indicators that directly reflect the amplitude fluctuation severity and the temporal variability of the scintillation effects on the signals, respectively. They also capture the stress of receiver tracking loop under scintillation conditions, which make this simulator more practical for receiver algorithm testing. This simulator is developed based on the compact TPPSM, which is specified by five parameters $\{U, p_1, p_2, \mu_0, \rho_F/V_{eff}\}$ as mentioned in section 1.3.1. In [Carrano and Rino, 2016], $\{U, \rho_F/V_{eff}\}$ were shown numerically to be more closely related to the temporal characteristics of the scintillation signals (i.e., $\{S_4, \tau_0\}$) than the three spectral parameters $\{p_1, p_2, \mu_0\}$. In this study, by defaulting three of the model parameters $\{p_1, p_2, \mu_0\}$ to representative values, numerical mappings from the user input parameter set S_4 and τ_0 to the remaining model parameter subset of two parameters, U_0 and ρ_F/V_{eff} , can be established through numerical evaluation. Therefore, the scintillation simulation model can be controlled by user-specified expected S_4 and τ_0 .

To obtain the representative values for the three default model parameters and to validate the numerical mappings for strong equatorial scintillation scenario, we first apply IPE to a large group of strong scintillation data (with $S_4 > 0.6$) from two equatorial sites to establish the profiles of the model parameters. The representative values for the three default model parameters are then determined based on their respective profiles. Based on the estimates of U_0 and ρ_F/V_{eff} and S_4 and τ_0 obtained from this multi-site real scintillation data set, we validated that the numerical mappings are generally accurate to represent the case in the observed strong equatorial scintillation. In addition, this study also presents the evaluation results of the IPE method in terms of triple-frequency consistency using real scintillation data set with triple-frequency scintillation. Finally, a MATLAB implementation of this two-parameter simulator is made available for public access.

1.4.2. Algorithm Development and Evaluation Using Simulated Data

This part of contribution is illustrated in Figure 1-3.

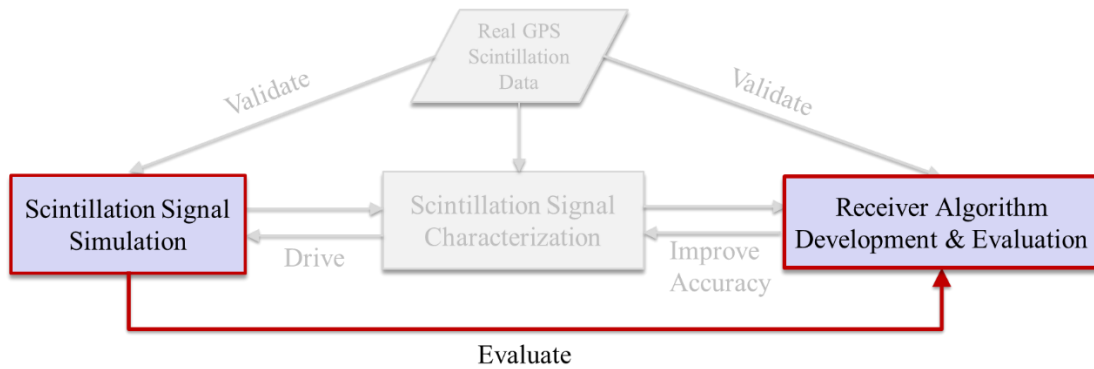


Figure 1-3. Illustration of contribution part 2 in this dissertation, which is algorithm development and evaluation using simulated data.

In order to better estimate the fast carrier phase changes concurrent with deep signal fading during strong equatorial scintillation, the SOL algorithm has been developed. Two other advanced carrier tracking algorithms, AR and OT, have been implemented. A comparative performance analysis

has been conducted using simulated data of different scintillation scenarios, which were generated by the scintillation signal simulator developed in contribution 1. The SOL outperformed the other two algorithms in terms of cycle slip occurrences and carrier phase estimation root-mean-square error (RMSE). Since the SOL tracking on dynamic platform relies on the VTL to obtain the receiver PVT solutions, the VTL PVT estimation performance is also evaluated using simulated data under scenarios where different numbers of satellites are simultaneously experiencing strong scintillation. Different satellite-weighting strategies were implemented to investigate the interaction between the satellite geometry worsening and scintillation-induced error on the VTL performance.

As a special case of scintillation affected applications, simulation results were for the first time obtained for the scintillation signals observed on a LEO satellite platform. Two different scenarios were simulated, where the scintillation signal is received: 1) on the zenith-looking POD antenna when traveling close to or inside the ionospheric structures; 2) on the limb-scanning RO antenna. The simulation results showed significantly different characteristics of scintillation between the two scenarios. The simulation data of these two scenarios were then used to evaluate an AKF-based algorithm against a conventional PLL of different integration times and bandwidths.

1.4.3. Scintillation Signal Characterization

This part of contribution is illustrated in Figure 1-4.

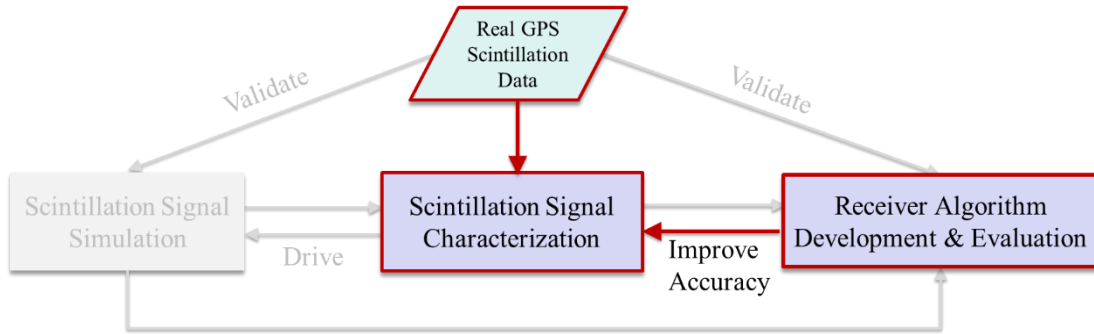


Figure 1-4. Illustration of contribution part 3 in this dissertation.

This part of contribution contains characterization on two kinds of processing results obtained both using data collected at Ascension Island: the fast phase changes concurrent with signal amplitude fading and the GPS L1 navigation bit decoding error (BDE).

For the fast phase changes characterization, SOL was used to process a subset of four days of IF data collected in Ascension Island, 2013 March, in order to ensure carrier phase estimation accuracy with a high resolution. The data subset contains only strong scintillation events, which are by having σ_ϕ or S_4 index on GPS L1 signal exceeding 0.15 cycles or 0.75, respectively. Based on statistical analysis of the processing results, we established the probability distributions of concurrent deep signal fading and fast carrier phase changes and the duration of the fast phase changes on GPS triple-frequency signals.

The navigation message being broadcast by GPS satellites contains information on satellite orbital and timing information needed to compute PVT solutions, as well as correction parameters to improve the solutions' accuracy. During equatorial scintillation, it is known that there is increased navigation data BDE which degrades the accuracy of the receiver's navigation solutions, especially when multiple satellites experience strong scintillation [Carroll and Morton, 2014; Zhang et al.,

2010a]. However, the quantitative dependence of the BDE on the scintillation level has not been studied. Such analysis is necessary because the degraded decoding performance can negatively impact high accuracy applications and differential systems where rover receivers and their corresponding ground correction networks share the same satellite orbital and timing parameters. In this study, the processing results were obtained based on a larger subset of the same Ascension Island data using a conventional 3-order PLL (PIF-based), in order to assess the BDE typically experienced by commercial receivers in the field. Based on statistical analysis of the processing results, we established correlations between the BDE distributions and the amplitude scintillation and fading characteristics such as fading level and duration.

1.5. Dissertation Outline

This dissertation starts with an overview of background in Chapters 1 and 2, which introduce ionospheric scintillation phenomenon, GPS civil signals, and previous literature related to the topics in this dissertation. Chapter 3 presents the first part of the dissertation contributions, i.e., the development and validation of the two-parameter scintillation simulator. Part 2 of the dissertation contributions will be presented in Chapter 4 and Chapter 5. Chapter 4 presents the details of SOL algorithm, and its evaluation against AR and OT. As part of the SOL, the PVT estimation performance of VTL will also be evaluated under strong scintillation on a dynamic platform in Chapter 4. In Chapter 5, scintillation signals received on a LEO satellite platform is simulated and tracked. Chapter 6 presents the characterization results on the fast carrier phase changes concurrent with deep fading and the GPS L1 BDE occurrences during ionospheric scintillation. Finally, Chapter 7 concludes the dissertation.

2. CHAPTER 2 – GPS CIVIL SIGNALS

The knowledge of the signal structure of GPS signals is fundamental to the work covered in this dissertation, especially for the task of scintillation signal simulation. This chapter summarizes the major structures of the three GPS civil signals that are currently available for the sake of completeness: L1 C/A, L2C, and L5. Most details can be found in the interface control documents (ICDs) published at <http://www.gps.gov>.

2.1. GPS Signal Structures

GPS signals consist of three components: radio-frequency (RF) carrier wave, pseudo random noise (PRN) code sequence unique to each satellite, and navigation data, which carries information about satellite orbits, clocks, satellite status information, etc. An example of the most widely used GPS L1 band C/A signal (stands for the coarse/acquisition signal) is illustrated in Figure 2-1. The carrier component is bi-phase shift key (BPSK) modulated with a bit train. The bit train is obtained by the modulo-2 sum of the PRN code sequence and navigation data. The three signal components are synchronized by the same on-board frequency standard [US Air Force, 2013]. In the time domain, signals broadcast from GPS satellites on carrier band L_i ($i=1, 2, 5$) are represented as:

$$s_{Li}(t) = \sum_j \alpha_{Li}^j D_{Li}^j(t) C_{Li}^j(t) \cos(2\pi f_{Li}t + \phi_{Li}^j) \quad (2-1)$$

where the subscript j denotes the satellite number; α^j is the signal amplitude; D^j is the navigation data bit; C^j is the PRN code; f_{Li} is the carrier frequency of band L_i ; ϕ^j is the initial phase carrier component.

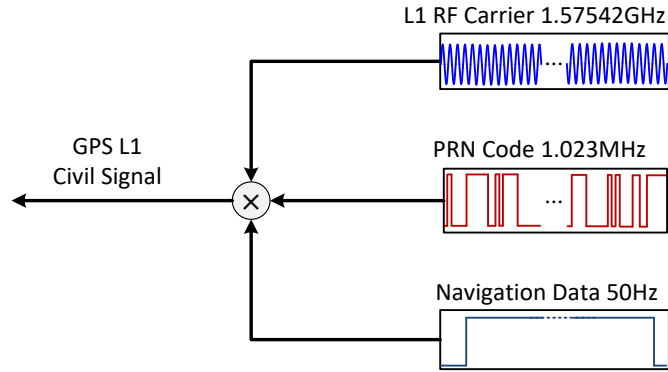


Figure 2-1. GPS L1 C/A signal structure.

There are currently five civil signals broadcasted on three bands of GPS (L1, L2, and L5). Table 2-1 contains signal specifications for these signals, while Table 2-2 lists the satellite numbers of three categories: the Block IIR satellites which only broadcast civil signals on L1, the Block IIR-M satellites which broadcast civil signals on L1 and L2 bands, and the Block IIF ones which broadcast civil signals on all three bands.

Table 2-1 GPS signal structure information [US Air Force, 2012, 2013]

Signal	Carrier Frequency (GHz)	Code Length (chips)	Code Frequency (MHz)	Navigation Data Rate (symbol s ⁻¹)	Secondary Code	Minimum Received Signal Power (dBW)	Satellite Blocks (First Launch Time)
L1 C/A	1.57542	1023	1.023	50	None	-158.5	All (7/23/98)
L2 CM	1.2276	10230	5.115	50	None	-160*	From IIR-M (9/26/05)
L2 CL		767,250	5.115	None	None		
L5I	1.17645	10230	10.23	100	NH10	-158	From IIF (5/28/10)
L5Q		10230	10.23	None	NH20	-158	

*: L2 CM signal and CL signal are time-multiplexed.

Table 2-2 List of GPS satellites of three blocks

Satellite Blocks	PRN Number
------------------	------------

IIR (L1 Only)	2, 11, 13, 14, 16, 18~23, 28
IIR-M (L1, L2C)	5, 7, 12, 15, 17, 29, 31
IIF (L1, L2C, L5)	1, 3, 6, 8~10, 24~27, 30, 32

The legacy L1 C/A signal is broadcast on all 31 of currently operational GPS satellites and provides coarse ranging for civil applications. It can also be used to facilitate a faster acquisition of the other signals in Table 2-1 which are modulated with longer codes and/or higher code frequency.

On L2 band, there are two civil signals broadcast on Block IIR-M satellites onward (currently 19 in total): the civil moderate (CM) signal modulated with navigation data and the civil long (CL) signal without. These two signals are time-multiplexed together during transmission and collectively referred to as the L2C signal. The CM code has a period of 20 ms and CL has a period of 1.5 seconds. Different from the legacy navigation message (LNAV) which is modulated on L1 C/A signal, the CM signal is modulated with a new type of navigation message (termed civil NAV or CNAV). The CNAV message data bit rate is 25Hz, but after applying the forward error correction (FEC) it is transmitted at 50 symbols per second (sps) [US Air Force, 2013]. The CNAV message was first broadcast in a test-mode for two weeks from June 15 to 29, 2013 [US Air Force, 2013]. Then, the implementation of the official CNAV broadcast was conducted in two phases: the continuous transmission of CNAV message began on April 28, 2014, on the L2C and L5 signals but at a reduced data accuracy and update frequency compared to LNAV; in December 31, 2014, it was announced that the CNAV data updates had been increased to a daily rate.

A detailed analysis of the differences between the formats of CNAV and LNAV was given in [Yin *et al.*, 2015], in which a more computationally efficient method for CNAV decoding was also presented. In addition, based on the data collected during the two weeks of CNAV test-mode broadcast, a comparison in terms of the orbit solution accuracy between the CNAV and LNAV ephemeris precision was conducted and presented. The results showed the CNAV message generated slightly more accurate satellite orbit estimation. In [Steigenberger and Montenbruck, 2015], based on a much larger amount of data collected after the official broadcast, the evaluation of the orbit and clock performance between CNAV and LNAV was presented. The results showed virtually identical overall orbit accuracy over the 60 days of data in 2015, but a smoother short-term orbit representation with the CNAV message was observed on the scale of one day.

For IIF (12 satellites) and future blocks of satellites, two civil signals are transmitted on L5 band: the in-phase (L5 I) signal and the quadrature (L5 Q) signal. L5 I and Q carrier waves are in quadrature with each other and modulated with different PRN code sequences of the same duration of 1ms. Therefore, the L5 signals can also be collectively viewed as one quadrature phase shift key (QPSK) signal. The L5 I and Q codes are further encoded with a 10-bit and 20-bit Neuman-Hoffman (NH) codes clocked at 1 KHz, respectively, which makes the total period of L5 I code 10ms and L5 Q 20ms. L5 I is modulated with the same CNAV data encoded with FEC as L2 CM is despite a higher symbol rate at 100 sps, whereas L5 Q is a data-less pilot channel.

The specified minimum received signal powers listed in Table 2-1 are around 10^{-16} Watts, which means the GPS signals received at antenna are buried under the thermal noise floor in normal operating conditions. For C/A signals, the peak value of its power spectral density (PSD) is

typically 15 dB below the noise PSD floor [Misra and Enge, 2011]. The PRN codes modulated on GPS signals are designed with remarkable correlation properties that can accumulate signal power during the correlation stage of signal processing.

It should be noted that the newer civil signals are added in order to satisfy the increasing demands for improved GPS performance for civil users. The L5 signal is intended mainly to support safety-of-life applications, such as aviation navigation. Both new civil signals are designed with longer code sequences to provide improved cross-correlation protection compared with the C/A-code. The benefits introduced by multi-frequency civil signals include improved ionospheric delay correction capability, facilitated carrier integer ambiguity resolution, and etc. The L5 signal will also provide improved multipath performance and protection against narrowband interference due to its wider spectrum and finer ranging code chips [Tran and Hegarty, 2002; Tran, 2004].

2.2. PRN Code Properties

The PRN codes for these signals are generated by performing modulo-2 sum on the outputs of two or more linear shift registers, and the PRN codes modulated on different satellite signals are almost orthogonal to each other. The correlation properties of L1 C/A code are shown in Figure 2-2. As can be seen in Figure 2-2, the code sequence will result in a sharp correlation peak only when it is correlated with a replica code aligned within one chip. Therefore, by transmitting a unique PRN code, a GPS satellite can be distinctly identified from the rest of the satellites, and the signal power can be effectively accumulated during correlation if the local replica code is properly aligned with the incoming code. The PRN code is also referred to as the ranging code, implying its usage in deriving range measurements from the satellite to the user.

As has been stated earlier, PRN codes on L2C and L5 signals are designed to have better correlation properties. The correlation properties of PRN codes on L1, L2C, and L5 signals are summarized in Table 2-3 [Tran and Hegarty, 2002].

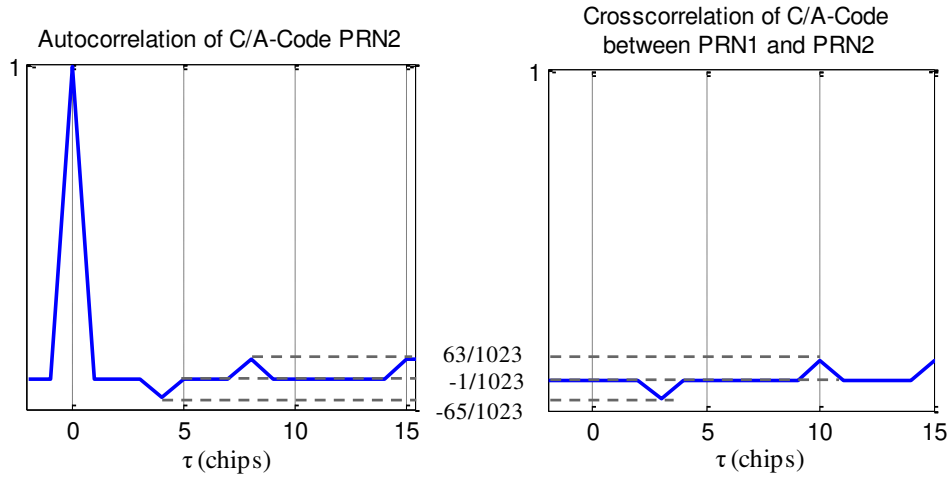


Figure 2-2. GPS C/A-Code Correlation Functions. The L1 C/A auto-correlation isolation and cross-correlation isolation are both better than $20\log_{10}(65/1023) = -23.9\text{dB}$.

Table 2-3. Auto-correlation $R(\cdot)$ and cross-correlation $C(\cdot)$ isolation for different civil signals [Tran and Hegarty, 2002]

L1	$R(CA, CA)(\tau > 1)$		$C(CA_i, CA_j)$		
Isolation < (dB)	-23.9		-23.9		
L2	$R(CM, CM)$	$R(CL, CL)$	$C(CM_i, CM_j)$	$C(CM, CL)$	$C(CL_i, CL_j)$
Isolation < (dB)	-26.9	-44.2	-25.4	-44.3	-43.9
L5	$R(I, I)$	$R(Q, Q)$	$C(I_i, I_j)$	$C(I, Q)$	$C(Q_i, Q_j)$
Isolation < (dB)	-29.2	-29.0	-26.4	-62.1	-26.4

As can be seen in Table 2-3, when compared with L1 C/A code:

- 1) The auto-correlation isolation of L2 CM code is improved by around 3dB, respectively, while the L2 CL code with a period of up to 1.5s theoretically (if coherently integrated over the whole period) has an improvement of over 20 dB. The cross-correlation of CM codes between different satellites is improved by 1.5dB, and the cross-correlation between CM

and CL codes also showed over 20dB improvement if integrated over the whole CL code period.

- 2) As for the PRN codes on L5 I and Q channels, the auto-correlation are both improved by around 5dB. The cross-correlation isolation between different satellites is improved by 2.5dB, while the cross-correlation between I and Q PRN codes on the same satellite are down to -62.1dB.

3. CHAPTER 3 – A TWO-PARAMETER SIGNAL SIMULATOR FOR STRONG EQUATORIAL SCINTILLATION

This chapter presents the development and validation of the two-parameter scintillation simulator. A brief summary of the phase screen realization and wave propagation under the TPPSM is first given, which define the five model parameters. Descriptions are then provided for the IPE method and the real scintillation data set processed by the IPE to establish the model parameter profiles. Based on the processing results, analysis is conducted to assess the IPE estimation consistency among triple-frequency scintillation signals, to obtain the representative values of three of the model parameters $\{p_1, p_2, \mu_0\}$, and to validate the numerical mappings between the user input parameter set $\{S_4$ and $\tau_0\}$ to the remaining model parameter subset $\{U_0$ and $\rho_F/V_{eff}\}$.

3.1. Scintillation Signal Simulator Routine Description

This section gives a description of the two-parameter scintillation signal simulator architecture. Figure 3-1 depicts the flow chart of the simulation routine, which outputs IF samples of GNSS scintillation signal. The parallelograms on the left side depict the user inputs, and the rectangular components show the different steps of simulation. The area outlined with red dashed line is the scintillation generator, which outputs the scintillation complex field time series ψ ($\psi = \delta_A e^{j\delta\phi}$). δ_A and δ_ϕ are the scintillation amplitude and phase, respectively.

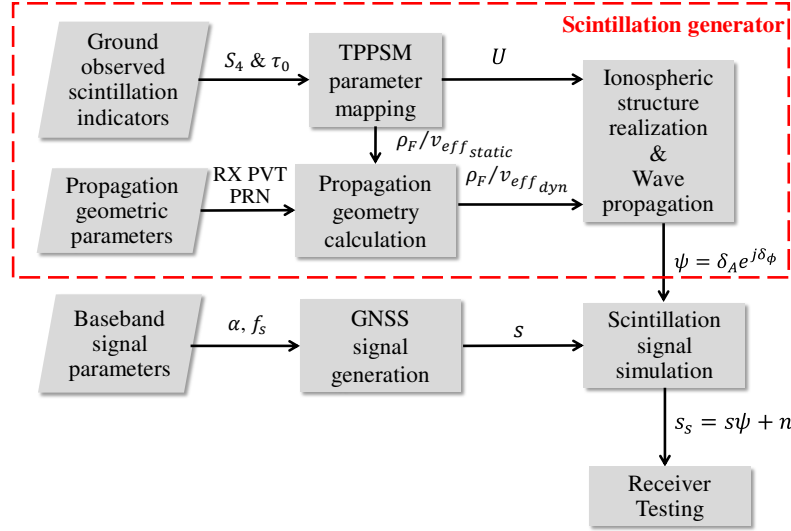


Figure 3-1. Flow chart of the scintillation signal simulator. The parallelograms on the left side depict the parameters to be specified by users, while the rectangular components are the different steps within the scintillation simulation. The simulator outputs IF samples of GNSS scintillation signal.

As can be seen in Figure 3-1, the parameters to be specified by users include three categories: ground observed scintillation indicators, propagation geometric parameters, and baseband signal parameters. The static ground observed scintillation indicators are the S_4 index and intensity decorrelation time τ_0 . The S_4 index is the standard deviation of the normalized signal intensity. In this study, we shall focus on strong scintillation where $S_4 > 0.6$. The intensity decorrelation time τ_0 is defined as the time delay where the normalized autocorrelation function of the signal intensity decreases to e^{-1} .

The user-input $\{S_4, \tau_0\}$ are first converted to $\{U, \rho_F/v_{eff_static}\}$ in the parameter mapping step. The ρ_F/v_{eff_static} is the time scaling factor of the static ground observed scintillation and will be used in the propagation geometry calculation step. As mentioned earlier, the three spectral parameters $\{p_1, p_2, \mu_0\}$ required to completely specify the phase screen realization are defaulted to their typical values, which will be determined in detail in section 3.5.2. Based on the mapped

value of U and the defaulted spectral parameters, a realization of phase screen is then generated to represent the ionospheric plasma structure responsible for ground observed scintillation effects. A brief description of the phase screen realization will be given in the next section.

For stationary platforms, the users only need to specify the two ground observed scintillation indicators, and the simulator will generate scintillation effects with S_4 and τ_0 values that match the user input. To simulate scintillation effects experienced on dynamics platforms, the users will need to specify the propagation geometric parameters to enable the calculation of ρ_F/v_{eff} for the user-defined dynamic platform. The propagation geometric parameters include the platform position and velocity (PV), date and time, and satellite PRN number. Based on the user specified PRN, date and time, the satellite orbit is calculated using the corresponding ephemeris, which is automatically downloaded from *Crustal Dynamics Data Information System* (CDDIS) of NASA.

All the geometric and dynamic dependencies are encapsulated in the calculation of the scaling factor ρ_F/v_{eff} in the compact TPPSM [Jiao et al., 2018]. The quantities involved in this calculation include the angle between the signal propagation direction and the geomagnetic field vector, the satellite scan velocity and receiver scan velocity at the phase screen, and the drift velocity of the ionospheric irregularities (V_{drift}) [Rino, 2011]. Among these quantities, the only unknown is V_{drift} , while the other ones can be calculated with the user-input propagation geometric parameters (satellite orbit and receiver PV) and existing models (such as the IGRF model). In this simulator, in order to obtain the ρ_F/v_{eff} value for user-defined dynamic platform ($\rho_F/v_{eff_{dyn}}$), the value of V_{drift} is first numerically solved using the $\rho_F/v_{eff_{static}}$ value from ground observed scintillation.

Finally, a plane wave is propagated through the phase screen realization, following the user specified geometry and dynamics embedded in $\rho_F/v_{eff_{dyn}}$ (or $\rho_F/v_{eff_{static}}$ for stationary-platform scintillation). This gives simulated scintillating wave fields at the receiver $\psi = \delta_A e^{j\delta\phi}$. A description of the wave propagation step will be given in the next section.

The simulated scintillation effects are then modulated onto nominal GNSS baseband samples to generate GNSS scintillation signals for receiver processing. By modifying equation (2-1), a generic non-scintillating GNSS baseband complex signal model can be expressed as:

$$s_k = \alpha_k D(k\Delta t - \tau_k) C(k\Delta t - \tau_k) e^{j\phi_k} \quad (3-1)$$

where k stands for the sample number, and Δt is the sampling interval. τ_k and ϕ_k denote the code delay and the nominal carrier phase delay, respectively. Carrier phase $\phi_k = 2\pi f_{d,k}\Delta t + \phi_{k-1} + \varepsilon_k$, where $f_{d,k}$ is the carrier Doppler frequency, and ε_k is the contribution from various phase noise and error sources other than scintillation. The user can specify signal amplitude α and sampling rate ($f_s = \frac{1}{\Delta t}$) for the GNSS baseband signal generation. The satellite-receiver geometric range yielded during the propagation geometry calculation is used to produce the carrier and code phase delays in the baseband signal samples.

The simulated scintillation amplitude ($\delta_{A,k}$) and phase ($\delta_{\phi,k}$) are modulated onto nominal GNSS baseband signal s_k to generate scintillation signals $s_{s,k}$ for receiver testing:

$$s_{s,k} = s_k \delta_{A,k} e^{j\delta_{\phi,k}} + n_k \quad (3-2)$$

where n_k represents the thermal noise, which is generated as white Gaussian in this thesis.

Ignoring the code and navigation message components, the received scintillation signal samples can then be rewritten as:

$$s_{s,k} = \alpha_k \delta_{A,k} e^{j\phi_{s,k}} + n_k \quad (3-3)$$

where $\phi_{s,k} = \phi_k + \delta_{\phi,k}$ is the composite carrier phase of the scintillation signal.

3.2. Phase Screen Realization and Wave Propagation

The propagation theory behind the scintillation generator depicted in Figure 3-1 was mainly developed in [Rino, 2011] and updated in [Rino *et al.*, 2018]. This section summarizes the fundamental mathematics for the phase screen realization step and wave the propagation step in this simulator. Readers are referred to [Rino *et al.*, 2018] and [Rino, 2011] for more details.

In the equatorial region, ionospheric irregularities are typically highly elongated along the geomagnetic field lines [Kintner, 2004; Takahashi *et al.*, 2016]. The phase screen structure is simplified to be two-dimensional, namely, the only variant crossing the field-aligned direction at a given height. Based on this approximation, the complex field ψ at a propagation distance x from the phase screen is generated by the following forward and inverse discrete Fourier transforms (DFTs) [Rino *et al.*, 2018]:

$$\hat{\psi}(0; n\Delta q) = \sum_{m=0}^{N-1} \exp\{i\phi(m\Delta y)\} \exp\left\{-\frac{2\pi inm}{N}\right\} \quad (3-4)$$

$$\psi(x; m\Delta y) = \frac{1}{N} \sum_{n=0}^{N-1} \hat{\psi}(0; n\Delta q) \exp\left\{-\frac{ik(n\Delta q/k)^2 x}{2}\right\} \exp\left\{\frac{2\pi inm}{N}\right\} \quad (3-5)$$

where y is the geomagnetic eastward direction, $\phi(y)$ is the path-integrated phase structure, q is the wavenumber along the y direction with Δq being its resolution, k is the signal carrier's wavenumber, and N is the size of the DFTs.

The path-integrated phase structure is characterized by a one-dimensional, two-component power-law SDF as follows:

$$\Phi_\phi(q) = C_p \begin{cases} q^{-p_1}, & q \leq q_0 \\ q_0^{p_2-p_1} q^{-p_2}, & q > q_0 \end{cases} \quad (3-6)$$

where C_p is the turbulence strength, p_1 and p_2 are the spectral indices, and q_0 is the break wavenumber.

Simplification is achieved by scaling the wavenumber q with the Fresnel scale ρ_F ($\rho_F = \sqrt{\frac{x}{k}}$) to a normalized unit such that $\mu = q\rho_F$. After such normalization, the SDF of the phase screen can be re-written as

$$P(\mu) = \Phi_\phi(q)/\rho_F = \begin{cases} U_1 \mu^{-p_1}, & \mu \leq \mu_0 \\ U_2 \mu^{-p_2}, & \mu > \mu_0 \end{cases} \quad (3-7)$$

where $U_1 = C_p \rho_F^{p_1-1}$, $U_2 = C_p q_0^{p_2-p_1} \rho_F^{p_2-1}$, and $\mu_0 = q_0 \rho_F$. Thus, the universal scattering strength U can be defined as:

$$U = \begin{cases} U_1, & \mu_0 \geq 1 \\ U_2, & \mu_0 < 1 \end{cases} \quad (3-8)$$

U is essentially the normalized phase spectral power at the Fresnel scale as $U \equiv P(\mu = 1)$ [Carrano and Rino, 2016].

A statistically equivalent phase screen realization can then be generated by imposing the above desired SDF on white noise:

$$\bar{\phi}_m = \sum_{n=0}^{N-1} \sqrt{\frac{P(n\Delta\mu)\Delta\mu}{2\pi}} \eta_n \exp\left\{-\frac{2\pi inm}{N}\right\} \quad (3-9)$$

where η_n is a zero-mean Gaussian random process with the Hermitian property.

Applying the phase screen realization $\bar{\phi}_m$ and substituting x with the Fresnel scale, the propagation equations (3-4) and (3-5) from the phase screen to the observation plane can be implemented in the simulation as:

$$\hat{\psi}(0; n\Delta\mu) = \sum_{m=0}^{N-1} \exp\{i\bar{\phi}_m\} \exp\left\{-\frac{2\pi inm}{N}\right\} \quad (3-10)$$

$$\psi\left(\rho_F; \frac{m\Delta y}{\rho_F}\right) = \frac{1}{N} \sum_{n=0}^{N-1} \hat{\psi}(0; n\Delta\mu) \exp\left\{-\frac{i(n\Delta\mu)^2}{2}\right\} \exp\left\{\frac{2\pi inm}{N}\right\} \quad (3-11)$$

To convert the complex field ψ from space to time domain, an effective scan velocity v_{eff} is used such that $y = v_{eff}t$. The calculation of v_{eff} involves knowledge of the ionosphere anisotropy, propagation geometry including different angles formed between the line-of-sight signal and the geomagnetic field, and velocities including the effective scan velocities of satellite and receiver at the phase screen and the drift velocity of the ionosphere irregularities v_{drift} . For detailed v_{eff} calculation procedure, readers are referred to [Rino, 2011].

The conversion from Doppler frequency to normalized wavenumber is

$$\mu = 2\pi f_D (\rho_F / v_{eff}) \quad (3-12)$$

where f_D is the Doppler frequency. A sampled phase screen constructed with $P(\mu_n)2\pi\Delta f_D/\Delta\mu = P(\mu_n)\rho_F/v_{eff}$ where $\Delta f_D = 1/N\Delta t$ and $\mu_n = n\Delta\mu$ will generate a

realization of time series (with an update rate of $1/\Delta t$) that are statistically equivalent of the scintillation defined by the phase screen structure. Intuitively, the ρ_F/v_{eff} directly determines how much compression or decompression the scintillation variations have over the temporal domain and is therefore tightly related to the decorrelation time of the scintillation intensity τ_0 , which will be shown in section 3.5.3.

The time series of the scintillation induced phase and amplitude are then obtained from the propagated complex field as:

$$\delta_\phi = \text{unwrap}\{\text{atan2}[\text{imag}(\psi), \text{real}(\psi)]\} \quad (3-13)$$

$$\delta_A = |\psi| = \sqrt{\psi\psi^*} \quad (3-14)$$

To summarize, a GNSS complex-field scintillation realization can be generated by specifying the TPPSM parameters $\{U, p_1, p_2, \mu_0 \text{ and } \rho_F/v_{eff}\}$ and the sampling parameters Δt and N . Among the TPPSM parameters, U , μ_0 , and ρ_F/v_{eff} are dependent on the signal carrier frequency, whereas p_1 and p_2 remain the same for different frequencies. To construct the same phase screen for different frequencies, these three parameters are scaled from one frequency (denoted as the reference frequency f_r) to another (denoted as the frequency with scaled parameters f_s) using the following equations:

$$\mu_0(f_s; f_r) = \mu_0(f_r) \sqrt{\frac{f_r}{f_s}} \quad (3-15)$$

$$\rho_F/v_{eff}(f_s; f_r) = \rho_F/v_{eff}(f_r) \sqrt{\frac{f_r}{f_s}} \quad (3-16)$$

$$U(f_s; f_r) = \begin{cases} U(f_r) \left(\frac{f_r}{f_s}\right)^{\frac{1}{2}p_1 + \frac{3}{2}}, & \text{if } \mu_0(f_r) \geq 1, \mu_0(f_s) \geq 1 \\ U(f_r) \frac{1}{\mu_0(f_r)^{p_2 - p_1}} \left(\frac{f_r}{f_s}\right)^{\frac{1}{2}p_1 + \frac{3}{2}}, & \text{if } \mu_0(f_r) < 1, \mu_0(f_s) \geq 1 \\ U(f_r) \mu_0(f_s)^{p_2 - p_1} \left(\frac{f_r}{f_s}\right)^{\frac{1}{2}p_1 + \frac{3}{2}}, & \text{if } \mu_0(f_r) \geq 1, \mu_0(f_s) < 1 \\ U(f_r) \left(\frac{f_r}{f_s}\right)^{\frac{1}{2}p_2 + \frac{3}{2}}, & \text{if } \mu_0(f_r) < 1, \mu_0(f_s) < 1 \end{cases} \quad (3-17)$$

Using TPPSM parameters of different frequencies that satisfy the relationships in equations (3-15) through (3-17) and the same white noise realization η_n in (3-9), the simulator generates realistic multi-frequency scintillation in terms of consistent scintillation level and correlated scintillation effects. This inter-frequency consistency of the simulated scintillation is essential for the evaluation of multi-frequency receiver algorithms [Yang *et al.*, 2018] and the study of multi-frequency scintillation characteristics [Rino *et al.*, 2018]. To assess the performance of the model and the parameter estimation method, the parameters estimated from real multi-frequency scintillation data are used to validate the relationships represented in equations (3-15) through (3-17). This part of work will be presented in section 3.5.1.

3.3. Parameter Estimation

3.3.1. IPE

As mentioned earlier, the IPE technique is used in this study to extract the TPPSM parameters from real scintillation data and establish their distributions under a strong equatorial scintillation scenario. The IPE technique method was developed in [Carrano *et al.*, 2012a; Carrano and Rino, 2016], while a brief introduction is provided in this section for completeness.

The IPE technique is essentially an iterative fitting procedure to obtain the TPPSM parameter estimates that yield the best match to the intensity SDF of the real scintillation data under the least square error criteria. It should be mentioned that the IPE technique is applied to the intensity SDF rather than the phase SDF due to the higher quality obtained in the signal intensity measurements than that in the phase measurements during strong scintillation [Skone *et al.*, 2001].

The intensity SDF $I(\mu)$ observed on the receiver plane from a given phase screen can be theoretically evaluated as follow [Carrano and Rino, 2016]:

$$I(\mu; p1, p2, \mu_0, U) = 2 \int_0^{\infty} \exp\{-\gamma(\eta, \mu; p1, p2, \mu_0, U)\} \cos(\eta\mu) d\eta \quad (3-18)$$

where $\gamma(\cdot)$ is the so-called structure interaction function defined in [Carrano and Rino, 2016]. $\gamma(\cdot)$ is prescribed by the phase screen SDF $P(\mu)$ in equation (3-7) and, therefore, is also parameterized by the model parameter subset $\{p1, p2, \mu_0, U\}$.

Conversion for the intensity SDF from the normalized wavenumber domain (in μ) in (3-18) to the temporal frequency domain (in f_D) is achieved through:

$$\Phi_{I,model}(f_D; p1, p2, \mu_0, U, \rho_F/v_{eff}) = I\left(\frac{\mu}{2\pi \rho_F/v_{eff}}; p1, p2, \mu_0, U\right) * \frac{2\pi\rho_F}{v_{eff}} \quad (3-19)$$

where $\Phi_{I,model}$ is the intensity SDF in the temporal frequency domain.

The metric used to measure the fitting error between the model SDF $\Phi_{I,model}$ and the measured SDF $\hat{\Phi}_{I,data}$ (the periodogram estimate of the real intensity measurement) is then defined as follows [Carrano *et al.*, 2012a]:

$$\chi^2(p1, p2, \mu_0, U, \rho_F / v_{eff}) = \frac{2}{f_{max} - f_{min}} \int_{f_{min}}^{f_{max}} [\log \Phi_{I,model}(f) - \log \hat{\Phi}_{I,data}(f)]^2 df \quad (3-20)$$

where f_{min} and f_{max} indicate the frequency range $[f_{min}, f_{max}]$ of the SDF over which the IPE fitting is performed upon, which is limited by the length N and update interval Δt of the intensity measurement by: $\frac{1}{N\Delta t} < f_{min} < f_{max} < \frac{1}{2\Delta t}$.

A highly efficient algorithm for numerically computing $I(\mu)$ using equation (3-18) as a function of $\{p1, p2, \mu_0, U\}$ is presented in [Carrano and Rino, 2016]. Using equation (3-19) the model intensity SDF in time frequency domain $\Phi_{I,model}$ can then be evaluated as a function of all five model parameters. Given an initial guess for the intensity SDF, the IPE program then iterates to obtain the optimal estimates of these parameters which provide the best fit of $\Phi_{I,model}$ to $\hat{\Phi}_{I,data}$ by minimizing χ^2 . This multi-dimensional minimization is performed with the Nelder-Mead simplex method conveniently implemented in the Matlab function **fminsearch**.

The current IPE obtains the TPPSM parameter estimates from intensity measurements of different frequencies separately. This provides a means to evaluate the accuracy of the IPE method in terms of inter-frequency consistency, which are prescribed by equations (3-15) through (3-17) with real multi-frequency data. This part of the work will be presented in section 3.5.1.

3.3.2. S_4 and τ_0 Calculation

As mentioned earlier, S_4 and τ_0 are the input for the simulator. To validate the parameter mappings, S_4 and τ_0 for both model and real data can be calculated from the intensity SDF as [Rino *et al.*, 2018]:

$$S_4 = \sqrt{2 * \int_{f_{min}}^{f_{max}} \Phi_I(f) df} \quad (3-21)$$

$$\tau_0 = find\{\tau | R_{SI}(\tau) = e^{-1}\} \quad (3-22)$$

where $\Phi_I = \Phi_{I,model}$ is the model intensity SDF (can be obtained using (3-19)), and $\Phi_I = \hat{\Phi}_{I,data}$ is the real measurement intensity SDF. $R_{SI}(\cdot)$ is the normalized autocorrelation function (ACF) of the intensity measurements, which can be obtained as the DFT of Φ_I . It should be noted, the S_4 value calculated from equation (3-21) should be the same as that from equation (1-1), as these two equations are mathematically equivalent.

3.4. Data Description

The real scintillation GPS data set used in this study were collected at two equatorial sites: Hong Kong (geographic: 22.2 ° N, 114.3° E; geomagnetic: 16° N, 187.0° E) and Ascension Island (geographic: 7.9° S, 14.4 ° W; geomagnetic: 12.3° S, 57.0° E) using Septentrio PolaRxs ISM receivers. The receivers are part of the global GNSS network deployed by the authors' group for ionospheric scintillation monitoring and studies [Morton *et al.*, 2015a]. For GPS civilian signals, the ISM receiver tracks L1 C/A signal, L2 CL signal and L5Q signal, and outputs various types of measurements including 100Hz update rate carrier phase and signal intensity. Both receiver locations are close to the equatorial anomaly (around geomagnetic latitude 15 °) where scintillation is known to be frequent and strong [Kintner *et al.*, 2007]. Using a machine learning-based

scintillation detection approach, we were able to identify a large amount of strong scintillation events collected from both sites as presented in [Liu *et al.*, 2018].

The signal intensity measurements are first divided into 5-minute segments and then selected to extract the TPPSM parameters using IPE and $\{S_4, \tau_0\}$ values using equations (3-21) and (3-22) for later analysis. The segment length of 5 minutes is heuristically chosen based on our experience working with a large amount of scintillation data. It is short enough to assume stationarity in scintillation effects, but also long enough to generate a reasonable intensity SDF estimate. Figure 3-2 shows 50-minute data on March 5, 2014 from Hong Kong with strong scintillation observed on all three frequencies on GPS PRN 1. Strong scintillation with frequent deep fading exceeding 40dB can be observed in the signal intensity on the top panel. The center of each 5-minute segment is marked with the segment numbers 1-9 at the bottom of the panel. The average S_4 index of each segment is plotted in the middle panel, while the bottom panel shows the elevation of PRN 1.

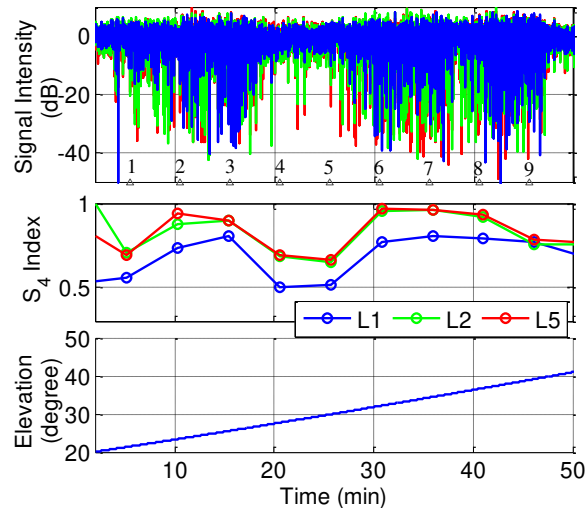


Figure 3-2. 50-minute processing results on March 5, 2014 in Hong Kong with strong scintillation observed on all three frequencies on GPS PRN 1, starting at 13:27:00 UTC. The triangles mark the center of each 5-minute segment that the intensity results are divided into.

To ensure the measurement quality for IPE processing, we imposed three criteria in data segment selection: 1) the segment average elevation is above 25° ; 2) the average S_4 index is over 0.6 on the L1 signal; 3) the segment contains consistent signal fading to meet a good stationarity assumption. For example, among the 9 segments shown in Figure 3-2, it can be seen that segments 3, 6, 7, and 9 meet all three criteria.

Based on these three criteria, the following three groups of scintillation intensity segments (forming a total of 174 segments) are selected from our scintillation data archives for IPE processing:

- 1) *Hong Kong spring data*: selected from 11 days during March 2014, containing 85 segments from 7 satellites;
- 2) *Hong Kong fall data*: selected from 8 days during September through early November 2014, containing 55 segments from 4 satellites;
- 3) *Ascension Island spring data*: selected during 8 days of March 2013, containing 34 segments from 4 satellites.

It can be seen that all three groups of data were collected during the maximum of solar cycle 24. These three groups of data were chosen for comparison so that potential seasonal and location dependency of the model spectral parameters can be observed. A subset of the data containing 45 segments with triple-frequency scintillation from groups 1 and 2 (on PRN 1, 3, 24, and 25) were selected to evaluate the IPE's performance, which will be presented in the following subsection.

3.5. Real Data Analysis

3.5.1. IPE Triple-frequency Consistency Evaluation

Figure 3-3 shows an example where the triple-frequency signal intensity from segment 7 in Figure 3-2 have been fitted using the IPE method. The top panels plot the data intensity SDFs (blue) and the fitted SDFs (red). Only the mid-frequency sections of the data intensity SDFs are used for the fitting, as indicated in the figure with the dashed, double-sided arrows. The lowest frequencies may be distorted by large-scale departures from stationarity, and the highest frequencies may be contaminated by receiver noise [Carrano and Rino, 2016]. Both are therefore excluded from the fitting. The S_4 and τ_0 values estimated from the data and fitted model are also listed. The bottom panels plot the data intensity ACFs and the fitted ACFs.

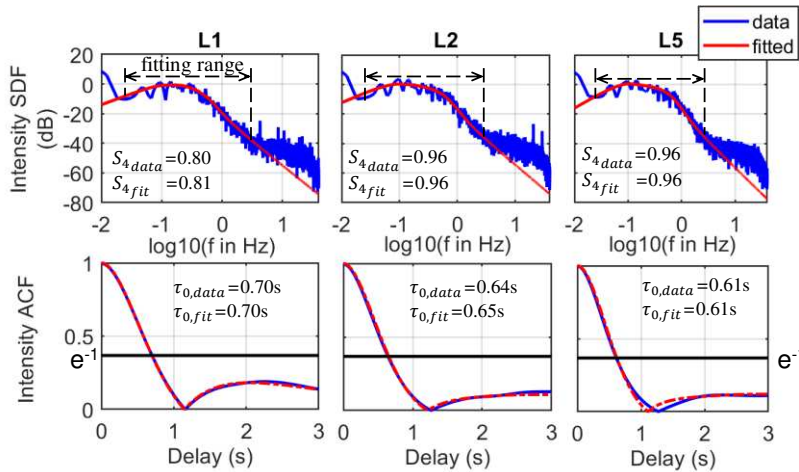


Figure 3-3. SDF and ACF for intensity scintillations observed on GPS triple-frequency signals from segment 7 in Figure 3-2. The SDFs and AFCs for the measurements are shown in blue, while those for the fitted model are shown in red. The dashed, double-sided arrow on each top panel indicates the frequency range over which the IPE fitting was performed.

From Figure 3-3, it can be seen that the shapes of the IPE-derived SDF and ACF are both very good fits to those of the data for all three frequencies, and the S_4 and τ_0 values of the IPE results

and of the data are also all in good agreement. This example shows that IPE is effective in fitting the observed data's SDF with TPPSM.

In order to evaluate the IPE method's performance in estimating these model parameters, the consistency across the carriers in the IPE-generated results were assessed using the triple-frequency data set. As mentioned in section 3.2 with equations (3-15) through (3-17), the five model parameters have different theoretical inter-frequency relationships, which can be summarized as follows:

1) p_1 and p_2 : These two parameters are not frequency dependent. In order to evaluate their frequency independence, three 2-D scatter plots can be formed with IPE estimates of three pairs of frequencies (L1-L2, L1-L5, and L2-L5). A linear relationship is then fitted with slope a and vertical offset b . This linear relationship is compared against the theoretical linear function with slope of 1 and offset 0. The resulting deviation can be described by the differences in the slopes ($\Delta a = a - 1$) and vertical offset ($\Delta b = b$);

2) μ_0 and ρ_F/v_{eff} : According to equations (3-15) and (3-16), these two parameters have the same frequency dependency of $g(Lj) = g(Li) \sqrt{\frac{f_{Li}}{f_{Lj}}}$, with $g = \mu_0$ or ρ_F/v_{eff} . Again, 2-D scatter plots are shown for each of the three pairs of frequencies for μ_0 and ρ_F/v_{eff} . A linear relationship can be fitted for each scatter plot. For a certain pair Li - Lj , the deviation between the fitted relationship and the theoretical relationship can be expressed

$$\text{as } \Delta a = a - \sqrt{\frac{f_{Li}}{f_{Lj}}} \text{ and } \Delta b = b;$$

3) U : the inter-frequency relationship of U is the most complicated one according to equation (3-17). It has four different forms depending on the μ_0 values on both frequencies in question. For the triple-frequency data subset used in this study, the IPE-estimated μ_0 values were all smaller than 1 for all three frequencies. This result limits U 's theoretical inter-frequency relationship to the fourth form in equation (3-17) as

$$U(Lj) = U(Li) \left(\frac{f_{Li}}{f_{Lj}} \right)^{\frac{1}{2}p_2 + \frac{3}{2}}.$$

This relationship is dependent on the frequencies and the p_2 value of the phase screen spectrum, which obviously varies among different data segments. Let's denote the IPE estimates of U from real data segments of a certain frequency Li as $\hat{U}(Li)$. As a result of the p_2 dependency, the estimate inter-frequency pairs $\hat{U}(Li)$ - $\hat{U}(Lj)$ from different data segments of the set cannot be directly combined into a scatter plot to fit a linear relationship for L1-L2, L1-L5, and L2-L5.

In order to assess the inter-frequency consistency of U estimation with a similar fashion as the other four parameters, for a certain frequency pair $Li - Lj$, a scatter plot is shown with $\hat{U}(Lj)$ still assigned to the vertical axis. For the horizontal axis, instead of directly using $\hat{U}(Li)$, a $\hat{U}(Li)$ -based prediction of $U(Lj)$ (denoted as $\hat{U}(Li \rightarrow j)$) is employed.

$$\hat{U}(Li \rightarrow j) \text{ is yielded using } \hat{U}(Li \rightarrow j) = \hat{U}(Li) \left(\frac{f_{Li}}{f_{Lj}} \right)^{\frac{1}{2}\hat{p}_2 + \frac{3}{2}},$$

where \hat{p}_2 is the p_2 estimate from each data segment. $\hat{U}(Li \rightarrow j)$ and $\hat{U}(Lj)$ should then be theoretically equivalent, and a linear relationship can be fitted from the resulting scatter plot. The corresponding correlation coefficient and deviation (as $\Delta a = a - 1$ and $\Delta b = b$) in turn reflect how close the $\hat{U}(Li)$ - $\hat{U}(Lj)$ relationship agrees with theory. It should be mentioned that, \hat{p}_2

used in the calculation of $\hat{U}(Li \rightarrow j)$ is the mean value of the triple-frequency p_2 estimates, in order to minimize the p_2 estimation error introduced into the calculation.

In Figure 3-4, the inter-frequency scatter plots summarized above for all five parameters are plotted with blue markers, each with three pairs (L1-L2 in the left panel, L1-L5 in the middle panel, and L2-L5 in the right panel). Within each panel, the least-square-fitted linear relationship and the model-prescribed relationships are plotted in red and black, respectively, with the correlation coefficients, the deviation Δa and Δb between the linear-fitted and the model relationships listed.

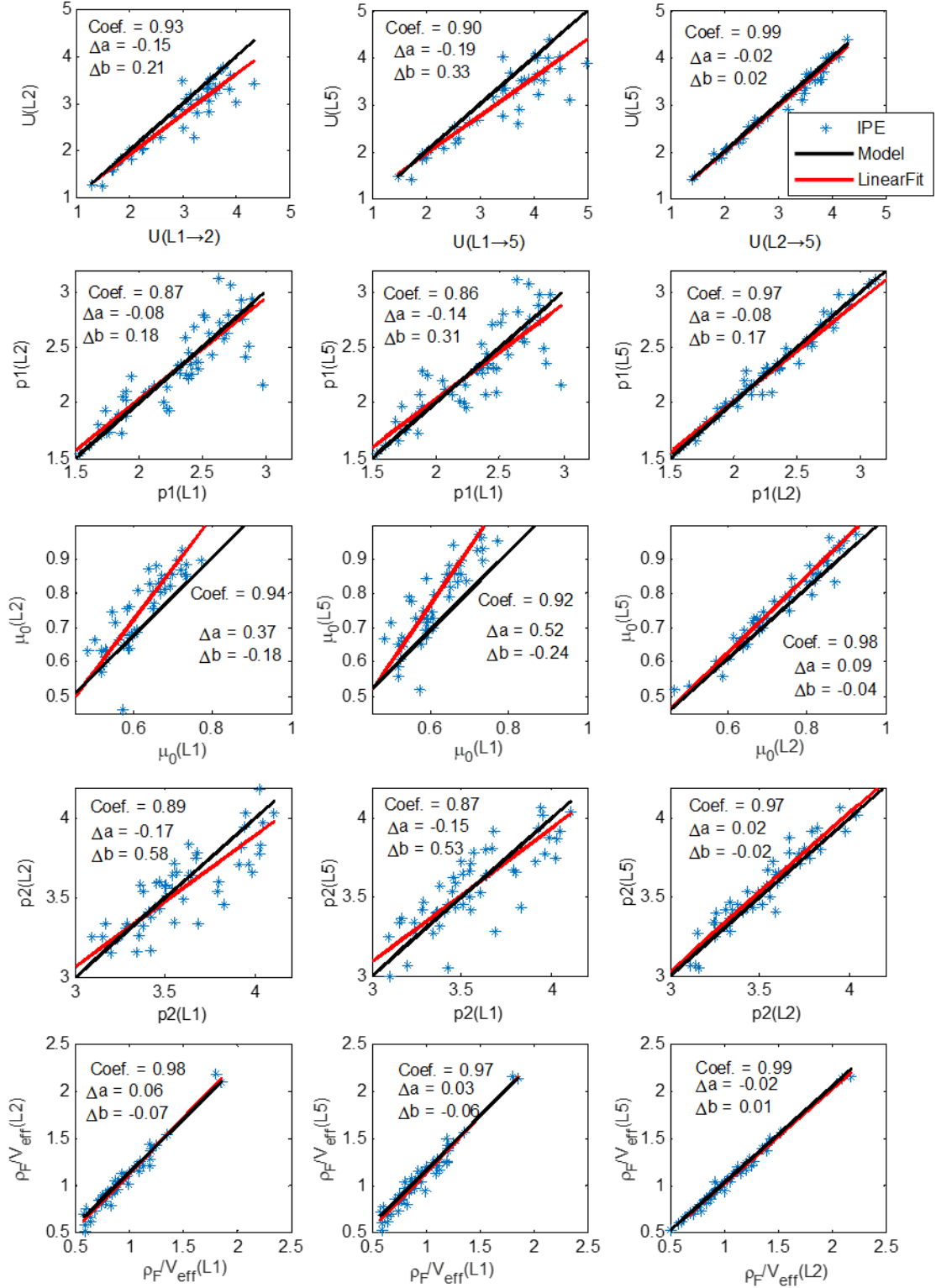


Figure 3-4. The inter-frequency relationships for all five parameters, each with three pairs (L1-L2, L1-L5, and L2-L5). Real data results are plotted in blue markers, and the least-square-fitted and the model-prescribed ones are in red and black, respectively. The correlation coefficients, the differences in the slope (Δa) and offset (Δb) between the linear-fitted and the model relationships are also listed.

As can be seen in Figure 3-4, all five parameters have in general high correlation coefficients among all three pairs of carriers results and small deviations (Δa and Δb) from the model, which validate the model prescribed linear relationships and IPE's performance. Among the results of three different frequency pairs, the L2-L5 pair generates the best results in both correlation coefficients and model deviations for all five parameters. This is most likely because L2 and L5 have stronger scintillation effects than L1, and, therefore, lead to a more dominant contribution in their own intensity SDFs over other error sources, which improves the IPE fitting accuracy. Among the results of the five parameters, the ρ_F/v_{eff} showed the best results in both correlation coefficients and model deviations, suggesting the highest sensitivity in fitting. This finding sheds light on the promising usage of the IPE as a way of inferring ionospheric background information such as V_{drift} for a standalone receiver, as has been mentioned in [Carrano and Rino, 2016; Rino et al., 2018].

3.5.2. Spectral Parameter Characterization

This section presents the distributions of the L1 signal spectral parameters $\{p1, p2, \mu_0\}$ obtained by IPE from the three groups of data sets to determine their most representative values and potential seasonal and location dependency. Figure 3-5 plots the distributions of $p1$ (left panel), μ_0 (middle panel), and $p2$ (right panels) from group 1 (denoted as G1 in green), group 2 (as G2 in blue), and group 3 (as G3 in red) with their mean values listed in the corresponding legends.

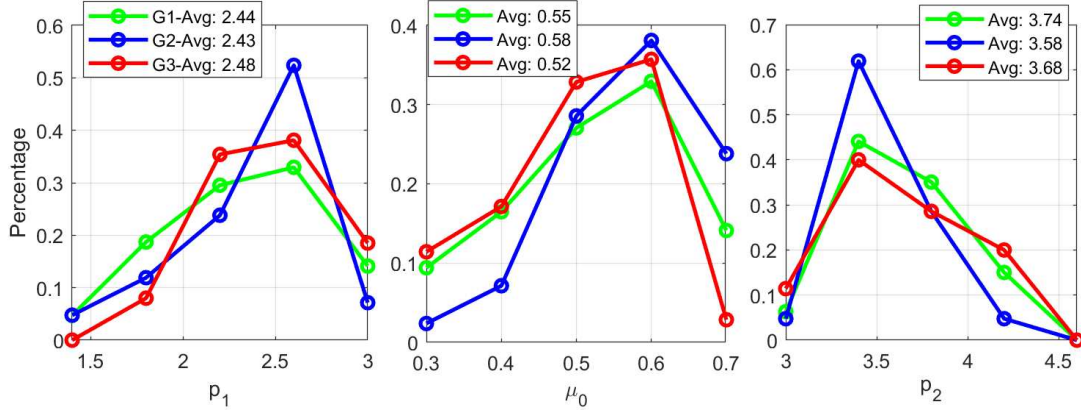


Figure 3-5. Distributions of the IPE-estimated spectral parameters from the three data groups (group 1 in green, group 2 in blue, and group 3 in red), with the mean values listed in the legends.

By examining Figure 3-5, there are no considerable discrepancies among the distributions of the parameters from three data groups for all three parameters, suggesting no apparent seasonal or location dependency of these parameters. The ranges for p_1 and μ_0 lie between 1.4 to 3 and 0.3 to 0.7, respectively, while p_2 generally ranges between 3 and 4.6. The results from all three groups are, therefore, combined to calculate the mean for each parameter as their representative values for the general strong equatorial scenario ($p_1 = 2.45$, $\mu_0 = 0.55$, and $p_2=3.70$).

It should be mentioned that the authors have investigated the correlation between parameter pairs for all five parameters in all three data groups, and no apparent correlations have been observed (the highest correlation coefficient was 0.41, which was between p_1 and U estimates in group 3).

3.5.3. Parameter Mappings and Real Data Evaluation

After defaulting the spectral parameters to their representative values obtained from the previous subsection, the mappings between $\{S_4, \tau_0\}$ and $\{U, \rho_F/v_{eff}\}$ can be established by numerically evaluating equations (3-18)(3-19)(3-21)(3-22).

By examining equations (3-18)(3-19)(3-21), how the S_4 index calculation is affected by different parameters from the model parameter set $\{U, p1, p2, \mu_0, \rho_F/v_{eff}\}$ can be broken down as follows:

- 1) according to (3-21), the S_4 value is directly determined by the shape and magnitude of $\Phi_I(f)$;
- 2) by looking at equation (3-19), $\Phi_I(f)$ is obtained by linearly mapping $I(\mu)$ into the time frequency domain with the space-to-time scaling factor of ρ_F/v_{eff} ;
- 3) $\{p1, p2, \mu_0, \text{ and } U\}$ then affect the calculation of S_4 as the shape of $I(\mu)$ is jointly determined by $\{p1, p2, \mu_0, \text{ and } U\}$, while its magnitude is directly determined by U , as demonstrated in [Carrano and Rino, 2016];
- 4) The value of ρ_F/v_{eff} affects the calculation of S_4 as it determines which part of the $I(\mu)$ corresponds to the part of $\Phi_I(f)$ being integrated over the range of $[f_{min}, f_{max}]$ in equation (3-21). This is indeed the case for scintillation effects on platforms with high dynamics and in an orbit close to the ionosphere (such as LEO satellites), where the value ρ_F/v_{eff} may have a small magnitude of 10^{-3} and become the dominant factor within equation (3-21) [Xu et al., 2018a]. However, since these numerical mappings are meant to relate stationary ground-observed scintillation indicators to the model parameters, the range of ρ_F/v_{eff} is limited to 0.5 to 2.0 as observed in the three data groups. Such limited variability does not affect the $I(\mu)$ to $\Phi_I(f)$ mapping sufficiently to impact the outcome of equation (3-21). Therefore, in the numerical mapping established for this simulator, the S_4 index is considered to be independent of ρ_F/v_{eff} and only related to U .

Figure 3-6 shows the numerically evaluated relationship (denoted as model, in red) and the scatter plot of the S_4-U estimate pairs from the combined scintillation data set (denoted as data, in black markers). In addition, an iterative fitting is performed in search for the optimal $\{p1, p2, \mu_0\}$ values that can achieve the least square error (LSE) w.r.t the real data's $S_4 - U$ pairs. The resulting $S_4 - U$ numerical relationship is also plotted in Figure 3-6 in blue, and the optimal $\{p1, p2, \mu_0\}$ values under LSE are listed in the legend.

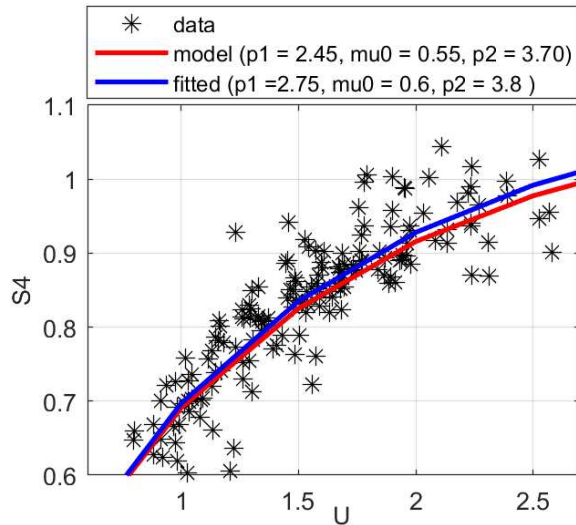


Figure 3-6. The numerically evaluated relationship (denoted as model, in red) and the scatter plot of the S_4 index and U estimates from the combined scintillation data set (denoted as data, in black markers), as well as the relationship that resulted from fitting the $p1, p2, \mu_0$ to optimal values that satisfy the LSE criteria w.r.t the data (denoted as fitted, in blue).

As can be seen in Figure 3-6, the LSE fitted values for $\{p1, p2, \mu_0\}$ are very close to their corresponding representative values obtained in the previous subsection, and the resulting two relationships are in close agreement with each other and appear to lie in the center of the variation range of the real data's $S_4 - U$ pairs. This validates the numerical mapping between the S_4 index and U .

As for τ_0 , the numerical evaluation shows that the ρ_F/v_{eff} is linearly correlated with τ_0 , and the slope of this linear relationship varies considerably w.r.t the variations of U within its typical range (usually 1~3 for strong L1 scintillation). Figure 3-7 plots the numerically evaluated relationships between τ_0 and ρ_F/v_{eff} color coded w.r.t different U values.

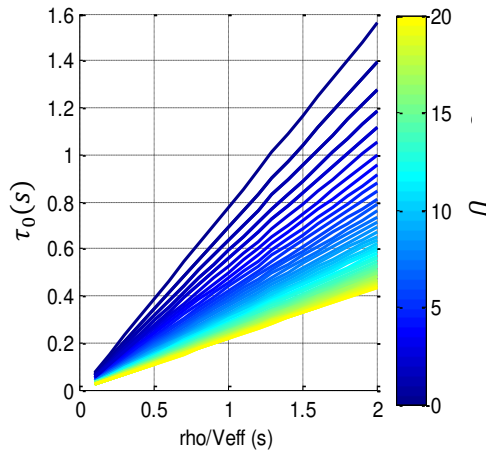


Figure 3-7. The numerically evaluated relationships between τ_0 and ρ_F/v_{eff} color coded w.r.t the corresponding U values.

As can be seen in Figure 3-7, the τ_0 and ρ_F/v_{eff} are linearly correlated with a slope that is determined by the value of U . As U increases, the slope becomes smaller, which means that under the same ρ_F/v_{eff} value, more severe scintillation will result in faster decorrelation. In order to validate these linear relationships between τ_0 and ρ_F/v_{eff} , the real data set is divided into four categories according to their ranges in U : [0.6~1], [1.0~1.5], [1.5~2.0], and [2.0~]; For each category, a numerical relationship between τ_0 and ρ_F/v_{eff} is obtained under the mean U value of the data samples within the corresponding category.

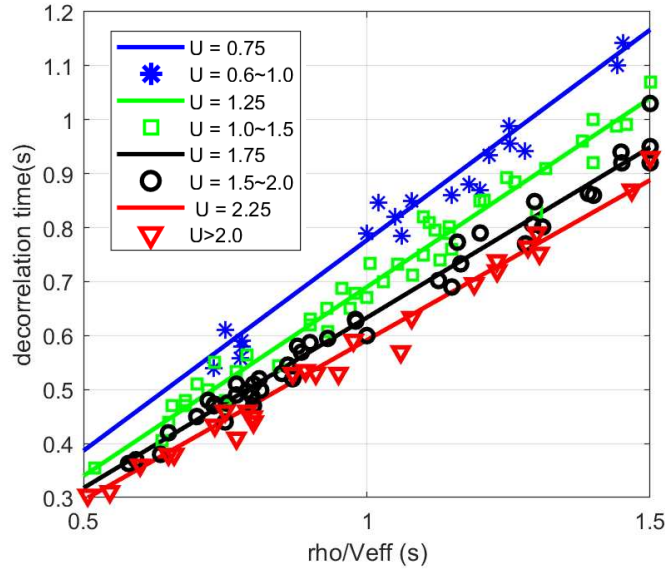


Figure 3-8. The scatter plot of the τ_0 versus ρ_F/v_{eff} estimates from the four categories of the real data distinguished by color and marker shapes. The numerical relationship conditioned on the mean U value of each data category is plotted as a straight line in the same color as the corresponding category. The U range and its mean value of each data category are listed in the legend.

Figure 3-8 plots the scatter plot of the τ_0 versus ρ_F/v_{eff} estimates from the four categories of the real data distinguished by color and marker shapes. The numerical relationship conditioned on the mean U value of each data category is plotted as a straight line in the same color as the scatter plot of the corresponding category. The U range and its mean value of each data category is listed in the legend. Figure 3-8 clearly shows close agreement between the model evaluated relationship and the τ_0 and ρ_F/v_{eff} relationship in real data, despite the variability of U within each data category.

After obtaining the representative values to default the model spectral parameter subset $\{p1, p2, \mu_0\}$ and the numerical mappings between $\{S_4, \tau_0\}$ and $\{U, \rho_F/v_{eff}\}$, the simulator can now be controlled by only specifying the expected $\{S_4, \tau_0\}$ values. An example of triple-frequency signal intensity is simulated using the same $\{S_4, \tau_0\}$ values as estimated from the real data segment

shown in Figure 3-3. Both the simulated signal intensity and the detrended intensity of the real data in Figure 3-3 are shown in Figure 3-9 with the corresponding $\{S_4, \tau_0\}$ values for each signal listed in the legend. The simulated signal intensity does not contain any low-frequency trend and, therefore, does not need detrending operations, while the detrending for the real data intensity was performed with a wavelet method as described in [Jiao *et al.*, 2016]. The phase scintillation between the real and simulated data are not shown here, because the triple-frequency phase measurements in the real data experienced numerous large cycle slips due to strong scintillation that require advanced cycle slip repair procedures, which is outside the scope of this study [Breitsch *et al.*, 2019].

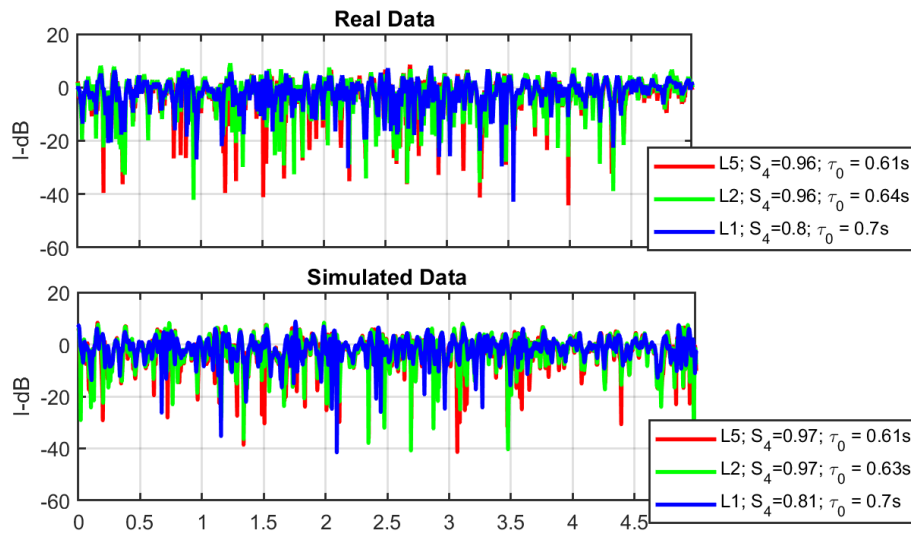


Figure 3-9. Comparison of the signal intensity in the simulated data and real data.

As can be seen in Figure 3-9, the simulation data and the real data show very similar characteristics in a statistical sense. The $\{S_4, \tau_0\}$ values between the real and simulator-generated data are also in good agreement for signals of all three frequencies. This validates the effectiveness of the two-parameter scintillation generator in simulating realistic, coherent triple-frequency scintillation according to the users' expected scintillation condition.

3.6. Concluding Remarks on Simulator Development

This chapter presented a TPPSM-based multi-frequency strong scintillation simulator that requires only the expected scintillation index S_4 and the intensity decorrelation time τ_0 . This simulator was developed by defaulting three of the TPPSM spectral parameters $\{p1, p2, \mu_0\}$ to representative values and therefore obtaining numerical mappings from the user input parameter set $\{S_4, \tau_0\}$ to the remaining parameter subset $\{U_0, \rho_F/V_{eff}\}$. The numerical evaluation shows that the S_4 has a one-to-one mapping relationship with U_0 , whereas τ_0 is linearly correlated with ρ_F/V_{eff} with a slope dependent on U_0 's value. Based on these numerical mappings, the scintillation model can then be controlled by specifying the expected S_4 and τ_0 values from scintillation measurements obtained from a stationary ground-based receiver. The simulator can generate statistically equivalent realizations of the scintillation effects. Using this basic two-parameter set, the simulator can also generate realistic scintillation effects that are observed on platforms with user-defined dynamics under the same ionospheric phase screen responsible for producing the ground received scintillation.

A total of 174 5-minute segments of strong scintillation data (with $S_4 > 0.6$) from two equatorial sites were processed using IPE to establish the profiles of the model parameters. Based on the profiles of the three spectral parameters from data collected from different locations and seasons, the distributions of the three parameters indicate that there are no clear location and seasonal dependencies. Therefore, the profiles are then combined to yield the defaulting values of the three spectral parameters $\{p1, p2, \mu_0\}$ used in obtaining the parameter numerical mappings, which are eligible to represent the most typical equatorial strong scintillation scenario. Based on the estimates of $\{U_0, \rho_F/V_{eff}\}$ and $\{S_4, \tau_0\}$ obtained from this multi-site real scintillation data set, numerical

mappings were validated to be generally accurate to represent the case in observed strong equatorial scintillation.

4. CHAPTER 4 – DEVELOPMENT AND EVALUATION OF ADVANCED CARRIER TRACKING ALGORITHMS FOR SCINTILLATION SIGNALS

This chapter first provides the fundamentals of GNSS receiver processing. The different stages of receiver software processing are briefly described, including signal processing, navigation processing, and applications. A summary is then given regarding the various components and conventional implementations in the signal processing stage. We then present the development and evaluation of the SOL algorithm using the scintillation simulator developed in Chapter 3. The two CLT algorithms (AR and OT) which will be evaluated against the SOL are also described. Different scintillation scenarios will be simulated to evaluate the carrier estimation accuracy of these three algorithms in terms of cycle slip occurrences and carrier phase RMSE. As the aiding source used in the SOL tracking on a dynamic platform, the performance of the VTL PVT estimation is also evaluated using simulated data containing strong scintillation on multiple satellites.

4.1. Fundamentals of GNSS Receiver Processing

A basic GNSS software-defined-radio (SDR) receiver block diagram is given in Figure 4-1. The RF signals transmitted from GNSS satellites are received by the antenna, and then amplified and down-converted to an IF signal through the RF chain. After being digitized by the Analog-to-Digital Converter (ADC), the IF digital signal is processed by software, which consists of signal processing, navigation processing, and potentially subsequent application specified processing functions. In the signal processing function, the input signal is first acquired and tracked. After the tracking reaches a steady state, the navigation message can then be decoded from the navigation data bit transitions on the signals, and the ranging code phase and carrier frequency are estimated

by the tracking loops. In the navigation processing function, the ephemeris and signal time stamps are first obtained from the navigation message, the code phase estimate is converted to the pseudorange estimate $\hat{\rho}$ based on the time stamp, and the carrier frequency estimate generates the pseudorange rate estimate $\hat{\dot{\rho}}$. If pseudoranges and pseudorange rates from more than 4 satellites are available, PVT solutions can be computed from them [Spilker, 1996].

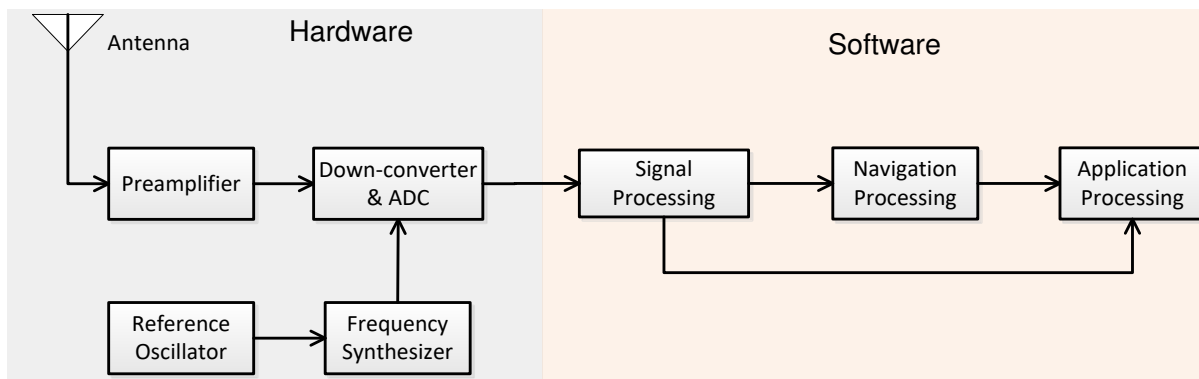


Figure 4-1. A fundamental GNSS receiver

Not all GNSS receivers perform the traditional navigation processing. Often, navigation processing is integrated into specific applications such as static and kinematic surveying, ionosphere remote sensing and scintillation monitoring, differential systems, and GPS satellite signal integrity monitoring. In addition, depending on the specific application of the receiver, the application processing may make direct use of the measurements recorded during the signal processing stage rather than the PVT solutions. For these special application receivers, the structure and implementation of the signal processing function may vary and the interaction between the signal processing function and the application processing function may be different.

In the signal processing function of a conventional receiver, the tracking of different satellite signals is typically performed in several parallel STL's that operate independently. The architecture of a STL-based receiver is given in Figure 4-2.

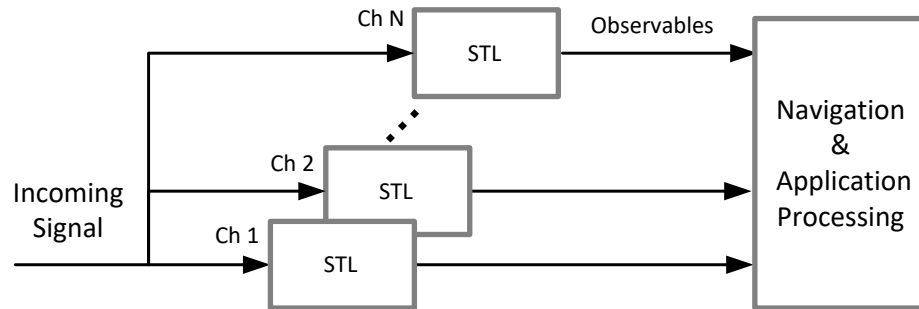


Figure 4-2. STL-based receiver architecture.

A STL comprises a code tracking loop and a carrier tracking loop. The carrier tracking loop can be a PLL, frequency-lock loop (FLL), or a combination of both. The code tracking loop is typically a delay-lock loop (DLL). The PLL tracks the carrier phase and frequency, while FLL is essentially differential carrier phase tracking. Due to its sensitivity in phase measurement, the PLL is generally more accurate than the FLL but more prone to cycle slips and potential loss of lock in high dynamic scenarios. FLLs, on the other hand, ignore absolute phase error and allow relative phase rotations between the received signal and the local carrier replica. Therefore it is often employed for the tracking of signals subject to severe dynamics, when the signal experiences sudden, random Doppler offsets and higher order dynamic effects [Ward *et al.*, 2005].

The DLL tracks the code phase and is usually implemented with a lower order filter than the PLL, because the code has a much smaller frequency compared to the carrier and is less susceptible to the impact of dynamics. A DLL sometimes makes use of the less noisy carrier loop outputs as an

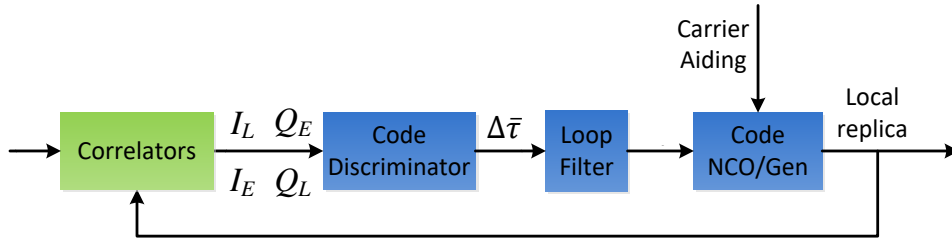


Figure 4-4. Block diagram of a traditional (a) PLL/FLL and (b) DLL.

4.1.1. Correlators

In Figure 4-3, all the components and flow paths share a common component, the correlator. First, the IF signal carrier is wiped off by in-phase (I) and quadra-phase (Q) replica carriers generated by the carrier generator with a frequency of the sum of IF and Doppler, and then the two channels of signals are correlated with the early (E), prompt (P), and late (L) code replicas that are generated by code generator to wipe the code off of the signal. A total of six correlator products ($I_E, Q_E, I_P, Q_P, I_L, Q_L$) are generated after the correlation function. The E and L code replicas are separated in phase by a spacing of typically 0.5 to 1 chip, with P in the middle.

Ignoring the cross-correlation from signals of other satellites and the impact that the limited pre-detection bandwidth has on the autocorrelation of the ranging code, the six correlation products over one code period can be expressed as follows:

$$\begin{aligned}
I_E &= \alpha \cdot N_T \cdot D \cdot \text{sinc}(\pi\Delta fT) \cdot R(\Delta\tau - d) \cdot \cos(\Delta\phi) + \text{noise}_{I,E} \\
Q_E &= \alpha \cdot N_T \cdot D \cdot \text{sinc}(\pi\Delta fT) \cdot R(\Delta\tau - d) \cdot \sin(\Delta\phi) + \text{noise}_{Q,E} \\
I_p &= \alpha \cdot N_T \cdot D \cdot \text{sinc}(\pi\Delta fT) \cdot R(\Delta\tau) \cdot \cos(\Delta\phi) + \text{noise}_{I,P} \\
Q_p &= \alpha \cdot N_T \cdot D \cdot \text{sinc}(\pi\Delta fT) \cdot R(\Delta\tau) \cdot \sin(\Delta\phi) + \text{noise}_{Q,P} \\
I_L &= \alpha \cdot N_T \cdot D \cdot \text{sinc}(\pi\Delta fT) \cdot R(\Delta\tau + d) \cdot \cos(\Delta\phi) + \text{noise}_{I,L} \\
Q_L &= \alpha \cdot N_T \cdot D \cdot \text{sinc}(\pi\Delta fT) \cdot R(\Delta\tau + d) \cdot \sin(\Delta\phi) + \text{noise}_{Q,L}
\end{aligned} \tag{4-1}$$

where α is signal amplitude, T is coherent integration time, N_T is the number of samples within T , D is the current message bit (+1 or -1), Δf is the Doppler frequency error, $\Delta\tau$ is code phase error of prompt replica code, d is the code phase spacing that separates E , P , and L , $R(\cdot)$ is the autocorrelation function of ranging code, and $\Delta\phi$ is the phase error.

As can be seen in (4-1), the correlation process stripped the code and carrier modulations from the signal, leaving the accumulated signal amplitude over the correlation period, navigation data bits, factors due to the code phase error $\Delta\tau$ and carrier phase error $\Delta\phi$, and noise. The term $\text{sinc}(\pi\Delta fT)$ can usually be considered as 1 for a small ΔfT during steady-state tracking. The correlation products that contain the “raw” code and carrier phase error information are the inputs to the DLL and the PLL/FLL to keep tracking the signal.

4.1.2. Discriminators

After correlation, the correlator outputs are first passed into a discriminator, where the error information $(\Delta\phi, \Delta f, \Delta\tau)$ between the incoming signal and the local replica are estimated. There are a number of different discriminators that can be applied to estimate the error. Among these discriminators, the ones that are insensitive to the presence of data modulation is usually called

Costas discriminators, which have a pull-in range of $[-\pi/2, +\pi/2]$, whereas the ones that have a range of a full cycle of $[-\pi, +\pi]$ are termed pure PLL discriminators in [Ward *et al.*, 2005]. Among these discriminators, arctangent function based Costas and pure discriminator have the widest linear zone within their corresponding pull-in ranges where the phase error $\Delta\phi$ can be linearly extracted from the correlator output pair I_p and Q_p , as given in (4-2) and (4-3), respectively:

$$\Delta\bar{\phi} = ATAN\left(\frac{Q_p}{I_p}\right) \quad (4-2)$$

$$\Delta\bar{\phi} = ATAN2(Q_p, I_p) \quad (4-3)$$

It should be mentioned here, the discriminator output $\Delta\bar{\phi}$ is an estimate of the average phase error during the integration period, which is why the accent bar ‘ $\bar{}$ ’ is used, which also applies to the frequency and code phase discriminators introduced later.

A FLL discriminator extracts the carrier frequency error Δf by operating on two adjacent pairs of I_p and Q_p samples. Different types of FLL discriminators are compared in [Ward *et al.*, 2005]. Similar to the PLL discriminators, the *ATAN*-based discriminators have the largest linear pull-in range. They are represented in (4-4) and (4-5):

$$\Delta\bar{f} = ATAN(\text{cross}/\text{dot})/T \quad (4-4)$$

$$\Delta\bar{f} = ATAN2(\text{cross}, \text{dot})/T \quad (4-5)$$

where $\text{dot} = I_{p1} * I_{p2} + Q_{p1} * Q_{p2}$, $\text{cross} = I_{p1} * Q_{p2} - Q_{p1} * I_{p2}$, the pair I_{p1} and Q_{p1} and the pair I_{p2} and Q_{p2} denote adjacent correlator output pairs.

In a DLL, the code phase error $\Delta\tau$ is estimated based on the shape of the autocorrelation function of the ranging code, $R(\Delta\tau)$. When $\Delta\tau$ is within the range of $(-1+d \text{ chip}, +1-d \text{ chip})$, there is a

linear relationship between $\Delta\tau$ and $R(\Delta\tau)$. A DLL discriminator is designed based on this linear relationship. For example, a normalized early minus late envelope discriminator is:

$$\Delta\bar{\tau} = (1 - d) \frac{E - L}{E + L} \quad (4-6)$$

where $E = \sqrt{I_E^2 + Q_E^2}$, $L = \sqrt{I_L^2 + Q_L^2}$.

4.1.3. Loop Filters

As depicted in Figure 4-4, the discriminator output is fed to a loop filter. The objective of the loop filter is to reduce noise in order to produce an accurate estimate of the original signal at its output.

There are many filter approaches adopted in digital loop filter designs for FLL/PLL, such as PIF, Wiener filter (WF), and KF [Yang Rong *et al.*, 2017ab], while for DLL the PIF, which is the most conventional design approach and simple to implement, is most widely used because code tracking is generally less fragile than carrier tracking.

The PIF derives the z-domain transfer function of a discrete-time tracking loop from the corresponding s-domain analog loop [Tsui, 2005; Ward *et al.*, 2005]. The resulting loop transfer function is defined by its loop natural frequency and loop coefficients, which jointly determine its response to dynamics and noise performance. The choice of loop natural frequency is inversely related to the loop steady-state error under dynamic stress, whereas the PIF loop coefficients in GNSS receivers are in most cases fixed to the typical values, which were derived from solving the steady-state gain of a KF of the same order, as demonstrated in [Christiansen, 1994; Jwo, 2001].

As the optimal filter in white Gaussian noise environments with feasibility for iterative implementation, KF is widely adopted both for scalar carrier tracking in challenging scenarios such as weak signals, high platform dynamics, and ionospheric scintillation [*O'Driscoll and Lachapelle, 2009; Peral-Rosado et al., 2010; Zhang et al, 2010b*] and for vector tracking as described in Chapter 1.

The architectural equivalence between a PIF and a KF was first presented in [*Driessen, 1994*], and then discussed in a GNSS tracking context in several later studies [e.g., *O'Driscoll and Lachapelle, 2009; Won et al., 2012*]. In the more recent paper [*Yang et al., 2017a*], a generalized GNSS signal carrier tracking loop architecture was established as a state space and state feedback control system representation for PLL and FLL.

In the following subsection, the KF-based PLL implementation is given, which summarizes the state-space representation of the KF framework presented in [*Yang et al., 2017a*]. This framework will serve as the basis for the two advanced KF-based tracking algorithms OT and AR, which will be presented later.

4.1.4. KF and the State-space Representation

The state-space representation of the KF-based PLL consists of a system model and a measurement model. The system model defines the state vector, state evolution, and the modeling of system noise. The measurement model defines how the state vector relates to the measurements.

The state vector \mathbf{x} for a single carrier is modeled as [*Yang et al., 2017ab*]:

$$\mathbf{x} = [\phi_0 \quad \omega \quad \dot{\omega}]^T \quad (4-7)$$

where ϕ_0 is the fractional phase in rad at the beginning of every epoch, ω is the carrier Doppler frequency in rad/s, and $\dot{\omega}$ is the frequency rate in rad/s².

The discrete system state model is given as:

$$\mathbf{x}_{k+1} = \mathbf{F} \mathbf{x}_k + \mathbf{v}_k \quad (4-8)$$

where \mathbf{F} is the state transition matrix:

$$\mathbf{F} = \begin{bmatrix} 1 & T & \frac{T^2}{2} \\ 0 & 1 & T \\ 0 & 0 & 1 \end{bmatrix} \quad (4-9)$$

In the basic KF-based framework, the system noise vector $\mathbf{v}_k \sim \mathcal{N}(\mathbf{0}, \mathbf{Q})$ takes into consideration the effects of the receiver local oscillator noise and the satellite-receiver line-of-sight (LOS) dynamics [Brown and Hwang, 1996]. The former is typically modelled on ϕ_0 and ω of the state vector. Its contribution to \mathbf{Q} is calculated using the oscillator h parameters, which can be derived from the noise spectral characteristics given in the oscillator datasheet [Van Dierendonck, 1993]. The LOS dynamics is modeled as a Gaussian random walk process due to the satellite-receiver LOS acceleration changes and is, therefore, modeled on all three state elements (ϕ_0 , ω , and $\dot{\omega}$). For detailed representations of the system noise models, please refer to [Yang et al., 2017ab].

The measurement model is given as:

$$\Delta \bar{\phi}_k = \mathbf{H} \cdot \Delta \mathbf{x}_k + w_k \quad (4-10)$$

where the matrix \mathbf{H} is the measurement matrix:

$$\mathbf{H} = \begin{bmatrix} 1 & \frac{T}{2} & \frac{T^2}{6} \end{bmatrix} \quad (4-11)$$

As mentioned earlier, for pilot channel signals, an *ATAN2* discriminator can be implemented to obtain $\Delta\bar{\phi}_k$, while for signals modulated with navigation data, typically an *ATAN* discriminator is used. $\Delta\mathbf{x}_k = \mathbf{x}_k - \hat{\mathbf{x}}_k$ is the error between the state vector truth and the KF prediction. w_k represents the measurement noise in the discriminator output, which is considered to be thermal noise as $w_k \sim \mathcal{N}(0, \sigma_{w,k}^2)$ and uncorrelated with the system noise \mathbf{v}_k . The measurement noise variance $\sigma_{w,k}^2$ due to thermal noise can be calculated using real-time estimates of signal C/N_0 as given in [Razavi et al., 2008; Yang et al., 2017a].

When combining the KF state prediction and update procedures, the KF-based PLL is then represented as:

$$\mathbf{x}_{k+1} = \mathbf{F}(\mathbf{x}_k + \mathbf{K}_k \Delta\bar{\phi}_k) \quad (4-12)$$

where \mathbf{K}_k is the KF gain.

For a KF-based tracking loop with fixed system and measurement noise covariance matrices, the KF will reach a steady-state when the Kalman gain converges to the steady-state Kalman gain. If the system and measurement models are accurate for the stable signal condition, the steady-state Kalman gain will be the optimal gain for the minimum mean square error (MMSE) criteria. During strong scintillation, frequent deep fades causes drastic changes in C/N_0 . Consequently, the measurement noise covariance needs to be updated at every epoch, and the filter gain should, therefore, also be promptly adjusted. A procedure was described in [O'Driscoll and Lachapelle, 2009; Yang et al., 2017ab] to address this issue. At a given epoch k , instead of recursively

computing the Kalman gain through the conventional KF prediction procedure to reach its steady-state value, the steady-state Kalman gain is obtained numerically by solving a discrete algebraic Riccati equation. The equation is formed with \mathbf{F} , \mathbf{H} , \mathbf{Q} , and the updated $\sigma_{w,k}^2$ based on the real-time estimate of C/N_0 . By applying this adaptively obtained Kalman gain, the KF therefore turns into an AKF.

4.1.5. Ionospheric Scintillation Measurements

In Chapter 1, the S_4 index and σ_ϕ were introduced as the widely used indicators for amplitude and phase scintillation, respectively. S_4 is the standard deviation of the signal intensity normalized over its trend. σ_ϕ is the standard deviation of the de-trended signal carrier phase. In this subsection, the calculation of de-trended signal carrier phase and signal intensity are introduced.

In order to obtain the de-trended carrier phase, the accumulated carrier phase measurements need to be obtained first. As has been discussed above, the loop filter drives the carrier phase NCO/generator to output “smoothed” carrier phase measurement, which is continuously counted by the accumulator. But for ionospheric scintillation monitoring applications, it is necessary to preserve phase scintillation effects in the carrier phase measurement. Therefore, as depicted in Figure 4-3, the accumulated carrier phase output $\hat{\phi}$ is obtained with adding the raw discriminator estimation $\Delta\bar{\phi}$ back to prior iteration accumulated loop NCO outputs $\hat{\phi}_{STL}$ [Van Dierendonck, 2005]. For the same reason, in such applications, navigation data bits need to be wiped off and an *ATAN2* carrier phase discriminator is implemented to accommodate larger phase variations:

$$\hat{\phi}_k = \hat{\phi}_{STL,k} + \Delta\bar{\phi}_k = \hat{\phi}_{STL,k} + ATAN2(Q_{p_k}, I_{p_k}) \quad (4-13)$$

where the subscript k denotes time instance.

The conventional approach to remove the satellite-receiver range variation, multipath, and other potential phase errors due to satellite orbit or clock instabilities is to filter $\hat{\phi}$ through a 6th order high-pass Butterworth filter with a cutoff frequency of 0.1Hz [Van Dierendonck, 2005; Niu, 2012].

The filtered output is the so-called detrended phase $d\phi$:

$$d\phi = BF_{6th}(\hat{\phi}, 0.1Hz) \quad (4-14)$$

The calculation of normalized signal intensity follows the process outlined in the following steps [Van Dierendonck, 1993]:

$$WBP = \sum_{k=1}^M (I_{p,1ms_k}^2 + Q_{p,1ms_k}^2) \quad (4-15)$$

$$NBP = \left(\sum_{k=1}^M I_{p,1ms_k} \right)^2 + \left(\sum_{k=1}^M Q_{p,1ms_k} \right)^2 \quad (4-16)$$

$$SI_{raw} = NBP - WBP \quad (4-17)$$

$$SI_{norm} = \frac{SI_{raw}}{SI_{trend}} \quad (4-18)$$

where WBP and NBP denotes narrow and wide band power, respectively. SI_{raw} is the raw signal intensity which is normalized by its own low frequency trend SI_{trend} to obtain the normalized signal intensity SI_{norm} . SI_{trend} can be generated using a 4th order polynomial fitting on SI_{raw} . M is typically set to 20ms for GPS L1 C/A signals due to the 50Hz navigation message modulated but can be extended in this study with the implementation of navigation bit wipe off.

As mentioned in section 4.1.4, the real-time estimate of C/N_0 is needed in the calculation of the AKF gain to adapt to fast signal fading during scintillation. However, the update interval for conventional C/N_0 estimation is much larger than the duration of a typical deep fade, rendering it inadequate to promptly detect the beginning of a signal fade [Xu et al., 2015]. To overcome this problem, we used a high update rate estimate of C/N_0 based on SI_{norm} in this study, which can be obtained at every tracking epoch, given as:

$$C/N_{0,SI} = SI_{norm} + C/N_{0,nominal} \quad (4-19)$$

where $C/N_{0,nominal}$ is the signal nominal C/N_0 , which varies for different frequencies and different satellites and can be easily obtained beforehand by examining the corresponding quiet-time C/N_0 values during the same time of day on the day before or after the scintillation event.

It should be noted that common methods to detrending the measurements include the above-mentioned 6th order Butterworth filter, polynomial fitting, and wavelet transformations, and etc. [Niu, 2012]. In fact, the choice of detrending methods, as well as the specific filter parameter selections, have been ongoing topics of debate for the past decade, as the selection of detrending method actually affects the outcome values of the scintillation indices [Niu, 2012]. However, this is outside the scope of this thesis, and the choice of detrending approaches throughout the work conducted in this thesis has adapted to the research consensus in this area.

4.2. Overview of the Advanced Carrier Tracking Algorithms

Figure 4-5 illustrates the major differences among the three algorithms. Their common components are plotted in black colored text boxes, including the correlator and reference generator, while the components of different approaches are shown in other colors (green, blue,

and red for SOL, OT, and AR, respectively). The dashed lines indicate inputs obtained from other frequencies (for OT) or other satellites (for SOL). The parameters associated with different approaches are identified by their subscripts (SOL is further shortened as ‘SL’).

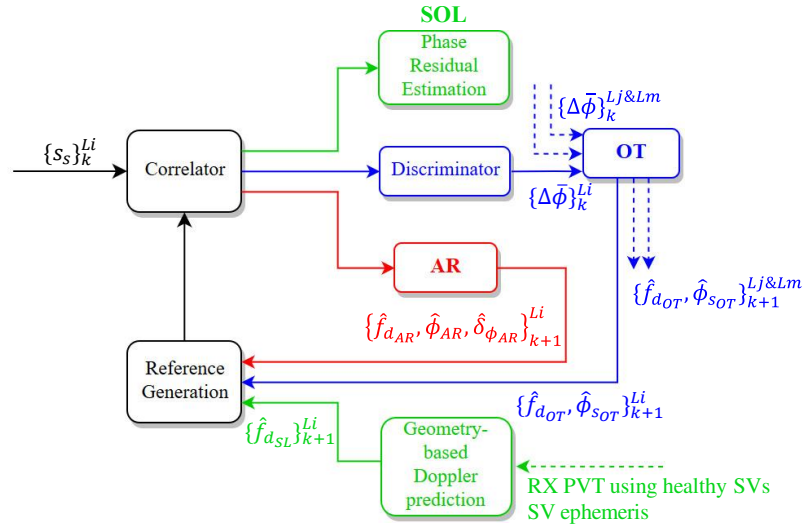


Figure 4-5. Three carrier phase estimation approaches, i.e., SOL, OT, and AR. The shared components are plotted in black, while the components of different approaches are plotted in green, blue, and red for SOL, OT, and AR, respectively. The dashes lines indicate inputs obtained from other frequencies (for OT) or satellites (for SOL).

The SOL is essentially a vector tracking system. It controls the reference generation using the predicted Doppler frequency $\hat{f}_{d_{SL}}^{Li}$ based on the geometry change due to receiver-satellite relative motion. The satellite motion can be obtained based on ephemeris, and the receiver PVT (or just time information for stationary platforms) are estimated from healthy satellites by a conventional VTL implementation with a vector first-order DLL and second-order FLL in this thesis (denoted as VDFLL).

The OT and AR are based on the same KF framework of PLL [Yang *et al.*, 2017a]. The OT combines the discriminator outputs from all available carrier frequency channels to estimate the

carrier states. OT updates both Doppler frequency \hat{f}_{dOT}^{Li} and the composite carrier phase $\hat{\phi}_{sOT}^{Li}$ for the reference generation. The AR is a scalar tracking loop which utilizes autoregressive process-based scintillation modelling to track the scintillation phase δ_{ϕ}^{Li} and the nominal carrier phase contribution ϕ^{Li} separately to improve robustness and accuracy.

In the following four subsections, we will first summarize the SOL algorithm and, for the sake of completeness, the VDFLL implementation. Brief descriptions are then provided for the implementation of OT and AR algorithms based on the state-space representation presented in section 4.1.4.

4.3. SOL

A SOL-based multi-frequency receiver for a stationary platform is depicted in Figure 4-6.

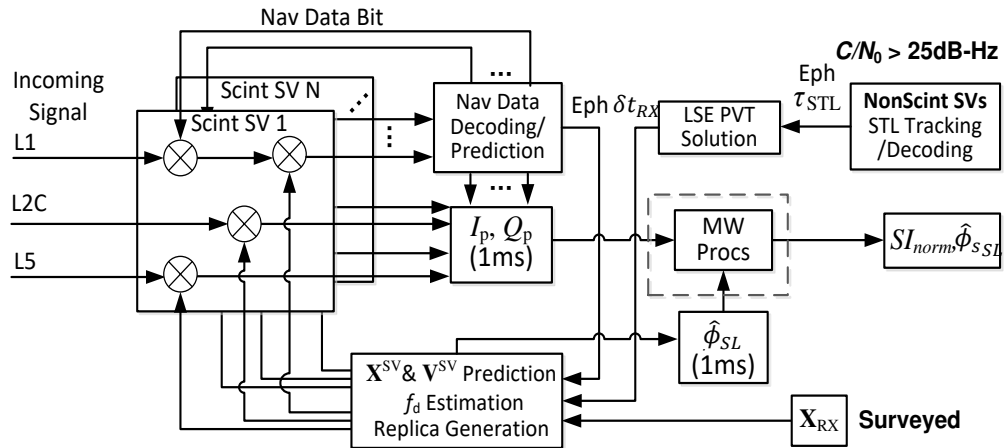


Figure 4-6. SOL-based SDR receiver architecture used in this study. The box with the dashed outline is the moving window processing procedure [Xu et al., 2015].

For stationary platforms, the only quantity that needs to be constantly updated is the receiver time bias, since the receiver position can be surveyed *a priori*. The receiver first generates PVT solutions by applying a conventional linearized LSE estimation procedure [e.g., Misra and Enge,

2011] using satellite signals that are not seriously compromised by scintillation. Then the clock bias estimation from the receiver-generated PVT solution is utilized along with the prior surveyed stationary receiver position for signal carrier Doppler frequency prediction. $C/N_0 > 25$ dB-Hz is the criterion used to select usable signals to generate the PVT solutions. An alternative approach for clock bias estimation was also implemented, which treats the receiver position as a known quantity and solve the range equation for each satellite signal to obtain the clock bias. The average bias from all usable satellite signals is then used to predict Doppler frequency. The two approaches yield similar clock bias estimation results. Since the SOL tracking process utilizes precise receiver position information, its outputs represent the upper bound of the VTL-tracking performance.

The signal parameters are then updated using the known receiver position, satellite ephemeris, and computed time information. Local replicas of carrier and PRN code are generated accordingly and used to correlate with incoming signals. The correlation is performed with a 1-ms integration time, and the prompt channel correlator outputs are then recorded, along with the carrier phase accumulated during the carrier replica generation. These measurements are then input to a moving window processing algorithm to generate SI_{norm} and carrier phase estimation $\hat{\phi}_{SL}$.

For dynamic platforms, both the receiver position and velocity estimation for each epoch need to be updated using measurements from healthy satellites. It should be mentioned, the accuracy in receiver PVT estimation using the linearized LSE estimation procedure is not only determined by the tracking accuracy from each healthy satellite, but also the satellite geometric distribution. During strong equatorial scintillation, multiple satellites can be simultaneously affected by scintillation effects. [Xu *et al.*, 2018b] evaluated the performance of a VDFLL implementation

under strong equatorial scintillation with limited healthy satellites. The results indicate that under practical scintillation conditions and due to the presence of a large number of available GNSS satellites, the degradation on the geometric dilution of precision (GDOP) is rather limited. Therefore, in this thesis, the same VDFLL implementation will be used to obtain the receiver PVT estimation for predicting $\hat{f}_{d_{SL}}$. This implementation has been well-documented in literature [e.g., Lashley et al., 2009; Xu et al., 2018b]. A brief summary will be provided shortly in section 4.3.5.

4.3.1. Propagation Time Prediction

The propagation time prediction method is based on code phase prediction technique presented in [Peng et al., 2012] and illustrated in Figure 4-7. This step is also necessary for later carrier Doppler frequency prediction. Therefore, before the on-set of a strong scintillation event, the receiver should be in steady-state tracking through another method, such as the PIF or KF, and have already achieved a valid receiver time solution. The time solution will be used to initialize the SOL.

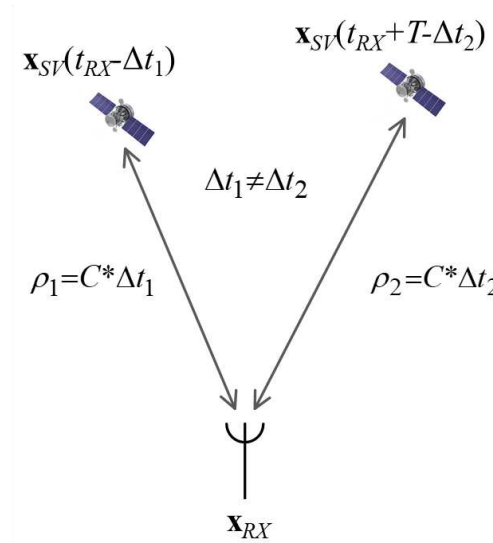


Figure 4-7. Illustration of propagation time prediction used in the SOL algorithm for a stationary receiver platform [Xu and Morton, 2015].

Assuming that at receiver time t_{RX} , the received signal was transmitted from a satellite at time $t_{RX} - \Delta t_1$, where Δt_1 is the signal propagation time. Δt_1 can be accurately computed by the code tracking loop. $\mathbf{x}_{SV}(t_{RX} - \Delta t_1)$ is the satellite position at the signal transmission time $t_{RX} - \Delta t_1$, and \mathbf{x}_{RX} is the receiver position. The signal arrived at the receiver at $t_{RX} + T$ was transmitted from the satellite at $t_{RX} + T - \Delta t_2$, where Δt_2 is the signal propagation time. Note that Δt_2 and Δt_1 may not be equal because the satellite has moved from $\mathbf{x}_{SV}(t_{RX} - \Delta t_1)$ to $\mathbf{x}_{SV}(t_{RX} + T - \Delta t_2)$. To predict the Doppler frequency at receiving time $t_{RX} + T$, the value for Δt_2 needs to be determined.

Because T is very small, the change in the pseudorange during the time period can be approximated as linearly dependent on T , and Δt_2 can then be obtained by a simple linear interpolation. The approximation procedure is illustrated in Figure 4-8, where the dotted slant line indicates the transmission times of the signal at the corresponding receiving times marked on the horizontal axis. t_x is the time when the signal transmitted at $t_{RX} - \Delta t_1 + T$ is received, and Δt_x is the corresponding propagation time. The procedure can be broken down into the following steps:

- 1) Calculate the satellite position $\mathbf{x}_{SV}(t_{RX} - \Delta t_1 + T)$ using the ephemeris;
- 2) $\Delta t_x = \|\mathbf{x}_{SV}(t_{RX} - \Delta t_1 + T) - \mathbf{x}_{RX}\|/C$;
- 3) $t_x = t_{RX} - \Delta t_1 + T + \Delta t_x$;
- 4) $\Delta t_2 = T \cdot \frac{(\Delta t_x - \Delta t_1)}{(t_x - t_{RX})} + \Delta t_1$.

where the notation $\|\cdot\|$ indicates the norm of a three-dimensional vector.

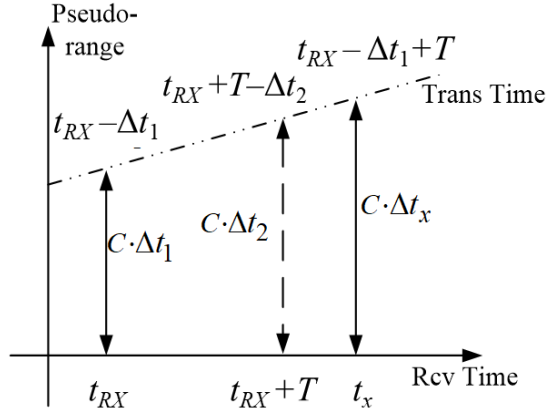


Figure 4-8. Illustration of Δt_2 linear approximation procedure in SOL algorithm. The dotted slant line indicates transmission times of the signal received at the corresponding receiving times marked on the horizontal axis [Xu and Morton, 2015].

4.3.2. Carrier Doppler Prediction

The above estimated value of Δt_2 is also used to predict the carrier Doppler frequency. With the known signal transmission time $t_{RX} + T - \Delta t_2$, the corresponding satellite velocity \mathbf{V}^{SV} at that time can be calculated using the ephemeris [Remodi et al., 2004], and the Doppler can then be estimated as:

$$\hat{f}_{d_{SL}} = \mathbf{I}_{RX \rightarrow SV} \cdot (\mathbf{V}^{SV} - \mathbf{V}^{RX}) / \lambda + \hat{f}_{clock} \quad (4-20)$$

where $\mathbf{I}_{RX \rightarrow SV}$ is the unit direction vector from the receiver to the satellite, \mathbf{V}^{SV} and \mathbf{V}^{RX} are the velocities of the satellite and receiver in the ECEF coordinate system, respectively; λ is the carrier wavelength; \hat{f}_{clock} is the receiver clock frequency offset estimation. \hat{f}_{clock} is slowly varying for an OCXO typically used in GNSS data collection systems for ionospheric monitoring and studies [Misra and Enge, 2011]. It can be estimated by averaging the Doppler residual between the geometry-induced Doppler and the tracked Doppler using any CLT tracking algorithm for the quiet period prior to the onset of scintillation. The Doppler residual is the difference between the

frequency estimated using the CLT algorithms and the frequency computed based on the receiver-satellite relative motion $\mathbf{I}_{RX \rightarrow SV} \cdot (\mathbf{V}^{SV} - \mathbf{V}^{RX})/\lambda$:

$$\hat{f}_{clock} = \langle \hat{f}_{d_{CLT}} - \mathbf{I}_{RX \rightarrow SV} \cdot (\mathbf{V}^{SV} - \mathbf{V}^{RX})/\lambda \rangle \quad (4-21)$$

where $\langle \cdot \rangle$ represents the average value over the interval of interest. This procedure can be applied for signals at all three-frequency bands.

If a less stable oscillator is used in the front end, \hat{f}_{clock} can be obtained from the velocity solutions [Misra and Enge, 2011] obtained using a VTL for all satellites whose signals were not severely contaminated by scintillation.

4.3.3. Moving Window Processing

The SOL correlator outputs generated at 1-ms integration interval are recorded. They are then coherently accumulated over N_{MW} ms to reduce noise and improve carrier phase estimation accuracy. Since navigation data bits have been wiped off of the correlator outputs for signals with data modulations, this coherent accumulation is achieved by summing the recorded 1-ms correlation outputs. Consecutive accumulation is applied through a moving window as indicated in Figure 4-9, leading to a small step size of 1 ms for the coherently integrated results. This moving window integration approach ensures a sufficiently high update rate and fine time resolution to capture fast carrier phase changes. The coherently accumulated correlator outputs through the moving window, denoted as I^{MW} and Q^{MW} , are then used to compute the detrended carrier phase $d\phi$ and SI_{norm} , which will be used for statistical analysis conducted in Chapter 6 to characterize fast phase changes and deep fades, respectively.

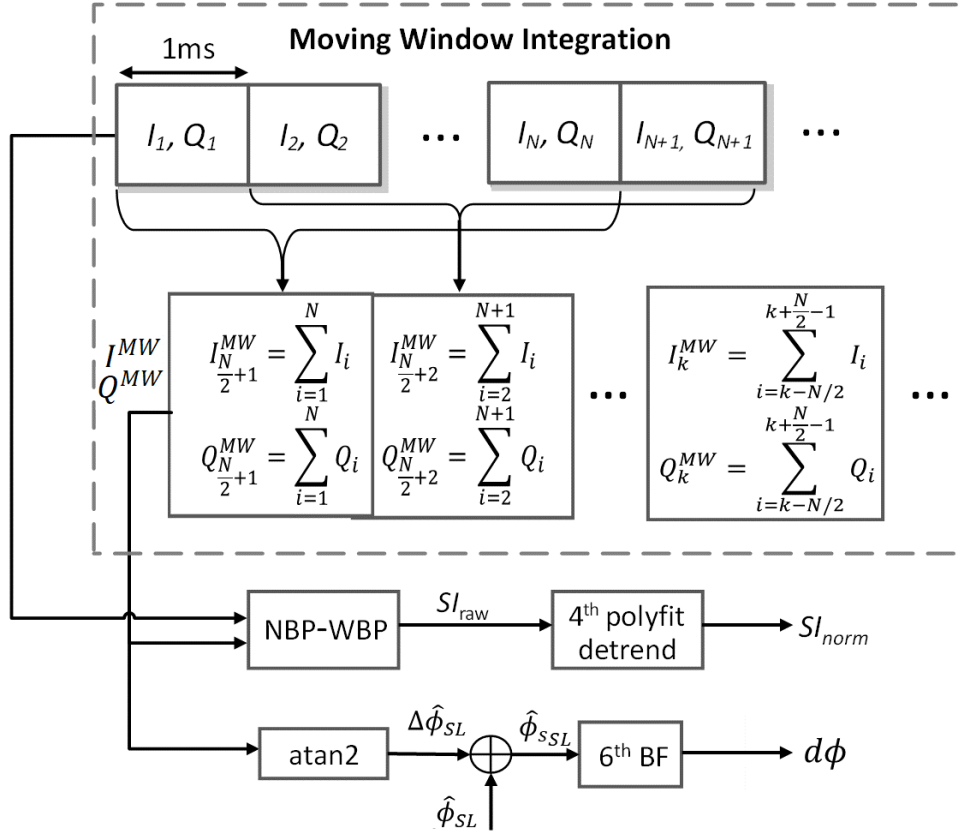


Figure 4-9. SOL moving window processing diagram. Moving window integration is performed on the recorded 1-ms correlator outputs with N_{WM} -ms window size and 1-ms step in this study. The MW integration outputs are then sent to calculate $S_{I_{norm}}$ and $d\phi$.

The moving window integration approach is feasible because for SOL, each correlator output is not affected by the carrier phase estimates from its previous time, as is the case for a CLT.

4.3.4. SOL Carrier Phase and Signal Intensity Estimation

To generate the estimate of the composite carrier phase ϕ_s (denoted as $\hat{\phi}_{sSL}$), the phase residual $\Delta\hat{\phi}_{sL}$ between the \hat{f}_{dSL} -integrated carrier phase $\hat{\phi}_{sL}$ and ϕ_s is first estimated from the correlator outputs I^{MW} and Q^{MW} . The composite carrier phase estimation $\hat{\phi}_{sSL}$ is then obtained by adding the discriminator output $\Delta\hat{\phi}_{sL}$ back to the \hat{f}_{dSL} -integrated carrier phase as follows:

$$\hat{\phi}_{s_{SL,k}} = \hat{\phi}_{SL,k} + \Delta\hat{\phi}_{SL,k} = \hat{\phi}_{SL,k} + ATAN2(Q_k^{MW}, I_k^{MW}) \quad (4-22)$$

The normalized signal intensity estimation for SOL follows the same process in equations (4-15) through (4-18), except that equations (4-15) and (4-16) need to be replaced by (4-23) and (4-24), respectively:

$$WBP_k = \sum_{i=k-N_{MW}/2}^{k+N_{MW}/2-1} (I_i^2 + Q_i^2) \quad (4-23)$$

$$NBP_k = (I_k^{MW})^2 + (Q_k^{MW})^2 \quad (4-24)$$

In order to obtain SI_{norm} with a high update rate and improved accuracy to better characterize the fading durations during deep fades, WBP and NBP are also calculated with a moving window integration of N_{MW} blocks of 1-ms correlation outputs. I_i and Q_i are 1-ms correlator outputs as shown in Figure 4-9.

4.3.5. VDFLL Implementation

As mentioned earlier, for SOL tracking on a dynamic platform, a conventional VDFLL implementation is used to estimate the receiver PVT based on measurements from healthy satellites. This section presents a summary on the VDFLL implementation for the sake of completeness. The VDFLL-based receiver architecture jointly tracks the code phases and carrier frequencies of different satellites in view, as depicted in Figure 4-10.

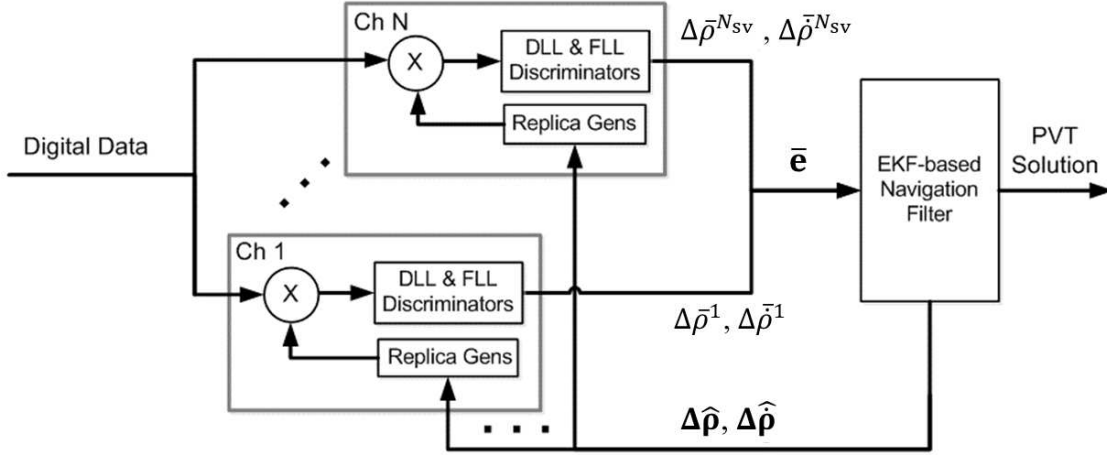


Figure 4-10. Vector tracking architecture used in this thesis. An EKF is implemented as the navigation filter in the receiver VDFLL structure. The bar accent ‘ $\bar{\cdot}$ ’ denote discriminator outputs/measured quantities, whereas the hat accent ‘ $\hat{\cdot}$ ’ denotes predicted quantities.

As can be seen in Figure 4-10, the measurement input to the EKF (denoted as $\bar{\mathbf{e}}$) are the scaled discriminator outputs $\Delta\bar{\rho}$ (in meters) and $\Delta\bar{\dot{\rho}}$ (in meters/second) from each satellite, which is given as:

$$\bar{\mathbf{e}} = [\Delta\bar{\rho}^1 \quad \Delta\bar{\dot{\rho}}^1 \quad \dots \quad \Delta\bar{\rho}^{N_{sv}} \quad \Delta\bar{\dot{\rho}}^{N_{sv}}] \quad (4-25)$$

where $\Delta\bar{\rho}$ is the pseudorange error estimate scaled from the code phase discriminator outputs $\Delta\bar{\tau}$ with the chip width, and $\Delta\bar{\dot{\rho}}$ is the pseudorange rate error estimate scaled from the carrier frequency discriminator outputs $\Delta\bar{f}$.

In this study, the EKF-based navigation filter adopted the most common design, which was referred to as the position-state formulation in [Lashley *et al.*, 2009]. In this design, the EKF state vector consists of the receiver’s position, velocity, and clock states, given as:

$$\mathbf{x}_E = [x_{RX}, \dot{x}_{RX}, y_{RX}, \dot{y}_{RX}, z_{RX}, \dot{z}_{RX}, \delta t_{RX}, \delta \dot{t}_{RX}]^T \quad (4-26)$$

where the first six elements are the receiver position (in meters) and velocity (in meters/second) in ECEF coordinates, whereas the δb_{RX} and $\delta \dot{b}_{RX}$ are the scaled clock bias (in meters) and clock drift (in meters/second), respectively.

The discrete system state model is given a [Lashley *et al.*, 2009]:

$$\mathbf{x}_{E,k+1} = \mathbf{F}_E \mathbf{x}_{E,k} + \boldsymbol{\gamma}_k \quad (4-27)$$

Where \mathbf{F}_E is the state transition matrix defined as:

$$\mathbf{F}_E = \begin{bmatrix} \boldsymbol{\Gamma} & \mathbf{0}_{2 \times 2} & \mathbf{0}_{2 \times 2} & \mathbf{0}_{2 \times 2} \\ \mathbf{0}_{2 \times 2} & \boldsymbol{\Gamma} & \mathbf{0}_{2 \times 2} & \mathbf{0}_{2 \times 2} \\ \mathbf{0}_{2 \times 2} & \mathbf{0}_{2 \times 2} & \boldsymbol{\Gamma} & \mathbf{0}_{2 \times 2} \\ \mathbf{0}_{2 \times 2} & \mathbf{0}_{2 \times 2} & \mathbf{0}_{2 \times 2} & \boldsymbol{\Gamma} \end{bmatrix} \quad (4-28)$$

$$\boldsymbol{\Gamma} = \begin{bmatrix} 1 & T \\ 0 & 1 \end{bmatrix}$$

The process noise vector $\boldsymbol{\gamma}_k$ is described as:

$$\boldsymbol{\gamma} = [\gamma_x, \gamma_{\dot{x}}, \gamma_y, \gamma_{\dot{y}}, \gamma_z, \gamma_{\dot{z}}, \gamma_{\delta t}, \gamma_{\delta \dot{t}}]^T \sim \mathcal{N}(\mathbf{0}_{8 \times 1}, \mathbf{Q}_\gamma) \quad (4-29)$$

In this study, the process noise is modeled with two noise sources, receiver dynamics $(\gamma_x, \gamma_{\dot{x}}, \gamma_y, \gamma_{\dot{y}}, \gamma_z, \gamma_{\dot{z}})$ and clock noise $(\gamma_{\delta t}, \gamma_{\delta \dot{t}})$. The dynamics of the receiver are modeled as a random-walk velocity process driven by a white noise. The white noise is input on the receiver velocity and then discretized by integration of time T into the noise terms $(\gamma_x, \gamma_{\dot{x}}, \gamma_y, \gamma_{\dot{y}}, \gamma_z, \gamma_{\dot{z}})$ on the position and velocity states. The platform-induced noise can be empirically obtained based on the expected maximum acceleration of the receiver. Details can be found in [Bar-Shalom *et al.*, 2004]. The terms $(\gamma_{\delta t}, \gamma_{\delta \dot{t}})$ represent the clock phase and frequency noise of the user's local oscillator, expressed in units of meters and meters/second, respectively. The corresponding

contribution on \mathbf{Q}_y can be obtained based on the oscillator h-parameters. Details can be found in [Brown and Hwang, 1996].

The measurement model can be written as:

$$\bar{\mathbf{e}}_{k+1} = \mathbf{G}_k(\mathbf{x}_{E,k} - \hat{\mathbf{x}}_{E,k}) + \mathbf{v}_{E,k} \quad (4-30)$$

where $\mathbf{x}_{E,k}$ is the state truth, and $\hat{\mathbf{x}}_{E,k}$ is the predicted state vector; $\mathbf{v}_{E,k}$ denotes the measurement noise with statistics as follows:

$$\mathbf{v}_{E,k} \sim \mathcal{N}(\mathbf{0}_{2N_{SV} \times 1}, \mathbf{R}_E)$$

$$\mathbf{R}_E = E[\mathbf{v}_{E,k}\mathbf{v}_{E,k}^T] = \begin{bmatrix} \mathbf{\Lambda}_1 & \mathbf{0}_{2 \times 2} & \mathbf{0}_{2 \times 2} \\ \mathbf{0}_{2 \times 2} & \ddots & \mathbf{0}_{2 \times 2} \\ \mathbf{0}_{2 \times 2} & \mathbf{0}_{2 \times 2} & \mathbf{\Lambda}_N \end{bmatrix}_{2N_{SV} \times 2N_{SV}} \quad (4-31)$$

$$\mathbf{\Lambda}_j = \begin{bmatrix} \sigma_{\rho_j}^2 & 0 \\ 0 & \sigma_{\dot{\rho}_j}^2 \end{bmatrix}, j = 1 \sim N_{SV}$$

The pseudorange and pseudorange rate noise variances $\sigma_{\rho_j}^2$ and $\sigma_{\dot{\rho}_j}^2$ can be estimated as [Lashley et al., 2009]:

$$\sigma_{\rho_i}^2 = (L_{chip})^2 \frac{d}{4TC/N_0} \left(1 + \frac{2}{(2-d)TC/N_0} \right) \quad (4-32)$$

$$\sigma_{\dot{\rho}_i}^2 = \frac{(\lambda)^2}{\pi(T)^3 C/N_0} \left(1 + \frac{1}{TC/N_0} \right)$$

where L_{chip} is the chip width in meters.

The geometry matrix \mathbf{G}_k is obtained as:

$$\mathbf{G}_k = \begin{bmatrix} l_x^1 & 0 & l_y^1 & 0 & l_z^1 & 0 & -1 & 0 \\ 0 & l_x^1 & 0 & l_y^1 & 0 & l_z^1 & 0 & -1 \\ \vdots & \vdots \\ l_x^{N_{SV}} & 0 & l_y^{N_{SV}} & 0 & l_z^{N_{SV}} & 0 & -1 & 0 \\ 0 & l_x^{N_{SV}} & 0 & l_y^{N_{SV}} & 0 & l_z^{N_{SV}} & 0 & -1 \end{bmatrix} \quad (4-33)$$

where $l_x^{1 \sim N_{SV}}$, $l_y^{1 \sim N_{SV}}$, and $l_z^{1 \sim N_{SV}}$ are the x,y,z elements in the LOS unit vectors of the N_{SV} satellites, respectively, given as:

$$\begin{aligned} l_x^j &= (x_{RX} - x^j) / \|\mathbf{x}_{SV}^j - \mathbf{x}_{RX}\| \\ l_y^j &= (y_{RX} - y^j) / \|\mathbf{x}_{SV}^j - \mathbf{x}_{RX}\| \\ l_z^j &= (z_{RX} - z^j) / \|\mathbf{x}_{SV}^j - \mathbf{x}_{RX}\| \end{aligned} \quad (4-34)$$

for $j \in 1$ to N_{SV} .

4.4. OT

The OT extends the basic KF-based PLL framework described in section 4.1.4 to a vectorized architecture with multi-frequency signals' measurements. The measurements are combined to update the states of the fundamental carrier. For GPS, its three carriers (L1, L2, L5) are generated by multiplying the fundamental carrier frequency f_0 ($f_0 = 10.23\text{MHz}$) by factors of $\eta^{L1} = 154$, $\eta^{L2} = 120$, and $\eta^{L5} = 115$, respectively [Kaplan and Hegarty, 2005]. To construct a fundamental carrier state vector for multi-frequency receivers, let us assume that the atmospheric and ionospheric propagation effects are negligible and a common oscillator reference for sampling the triple-frequency signals. The fundamental state vector at f_0 can be constructed (denoted as \mathbf{x}^{f_0}) and related to the individual carrier state vector \mathbf{x}^{Li} defined in (4-7) (the superscript Li is added to denote the state vector of the Li carrier) as follows:

$$\mathbf{x}^{f_0} = [\varphi^{f_0} \quad \omega^{f_0} \quad \dot{\omega}^{f_0}]^T = \mathbf{x}^{Li} / \eta^{Li} \quad (4-35)$$

The basic KF system model and measurement model can be extended to \mathbf{x}^{f_0} accordingly, as follows [Yang *et al.*, 2019]:

$$\mathbf{x}_{k+1}^{f_0} = \mathbf{F}\mathbf{x}_k^{f_0} + \mathbf{v}_k^{f_0} \quad (4-36)$$

$$\Delta\bar{\phi}_k^{Li} = \eta^{Li}\mathbf{H}\Delta\mathbf{x}_k^{f_0} + \mathbf{w}_k^{Li} \quad (4-37)$$

where $\mathbf{v}_k^{f_0}$ denotes the system noise for the fundamental carrier given as $\mathbf{v}_k^{f_0} = \mathbf{v}_k^{Li}/\eta^{Li}$. The corresponding system noise covariance \mathbf{Q}^{f_0} is therefore related to \mathbf{Q}^{Li} as $\mathbf{Q}^{f_0} = \mathbf{Q}^{Li}/(\eta^{Li})^2$. The fundamental state vector error $\Delta\mathbf{x}_k^{f_0}$ is related to $\Delta\mathbf{x}_k^{Li}$ as $\Delta\mathbf{x}_k^{f_0} = \mathbf{x}_k^{f_0} - \hat{\mathbf{x}}_k^{f_0} = \Delta\mathbf{x}_k^{Li}/\eta^{Li}$. The OT's state transition and measurement matrices are the same as in the basic KF, which were defined in (4-9) and (4-11), respectively.

In OT, the system noises for the carrier frequencies are considered to be linearly correlated as in equation (4-36), while the measurement noises are assumed to be uncorrelated. Under these assumptions and relationships, the measurements from all carriers are first combined to estimate the fundamental state, which is in turn scaled to each carrier frequency to drive their own reference generation. Let's denote the multi-carrier measurement input and noise vectors as $\mathbf{z}_k = [\Delta\bar{\phi}_k^{L1} \quad \Delta\bar{\phi}_k^{L2} \quad \Delta\bar{\phi}_k^{L5}]^T$ and $\mathbf{w}_k = [w_k^{L1} \quad w_k^{L2} \quad w_k^{L5}]^T$, respectively, and the frequency scale vector as $\mathbf{B} = [\eta^{L1} \quad \eta^{L2} \quad \eta^{L5}]^T$. The measurement model for the multi-carrier system is then presented in a vector form as [Yang *et al.*, 2019]:

$$\mathbf{z}_k = \mathbf{B}\mathbf{H}\Delta\mathbf{x}_k^{f_0} + \mathbf{w}_k \quad (4-38)$$

The multi-frequency measurement noise covariance matrix is given as:

$$\mathbf{R}_k = E[\mathbf{w}_k \mathbf{w}_k^T] = \begin{bmatrix} (\sigma_{w,k}^{L1})^2 & 0 & 0 \\ 0 & (\sigma_{w,k}^{L2})^2 & 0 \\ 0 & 0 & (\sigma_{w,k}^{L5})^2 \end{bmatrix} \quad (4-39)$$

In OT, at a given epoch k , \mathbf{z}_k is first passed into an aggregated filter, where the fundamental state is updated and propagated to the next epoch as follows:

$$\hat{\mathbf{x}}_{k+1}^{f_0} = \mathbf{F}(\hat{\mathbf{x}}_k^{f_0} + \mathbf{L}_k \mathbf{z}_k) \quad (4-40)$$

where \mathbf{L}_k is the Kalman gain matrix of this aggregated filter.

As mentioned in section 4.1.4, the steady-state Kalman gain for a single carrier AKF can be numerically solved by solving a discrete algebraic Riccati equation, which is formed by \mathbf{F} , \mathbf{H} , \mathbf{Q}^{Li} , and the real-time estimate of $\sigma_{w,k}^2$. This approach can be extended to obtain the steady-state value of \mathbf{L}_k , where the corresponding Riccati equation is formed by replacing $\{\mathbf{H}, \mathbf{Q}^{Li}, \text{ and } \sigma_{w,k}^2\}$ with $\{\mathbf{BH}, \mathbf{Q}^{f_0}, \text{ and } \mathbf{R}_k\}$, respectively.

$\hat{\mathbf{x}}_{k+1}^{f_0}$ is then scaled to yield the state vector prediction $\hat{\mathbf{x}}_{k+1}^{Li}$ on each individual carrier using $\hat{\mathbf{x}}_{k+1}^{Li} = \eta_{Li} \hat{\mathbf{x}}_{k+1}^{f_0}$. It should be mentioned, the ionospheric scintillation effects will cause phase divergence among different carrier frequencies in the multi-frequency carrier phase tracking, as discussed in [Yang *et al.*, 2019]. To address this issue, in the OT implementation, the phase element $\{\hat{\phi}_0\}_{k+1}^{Li}$ in the individual carrier state vector $\hat{\mathbf{x}}_{k+1}^{Li}$ is updated directly using its own discriminator output, while the Doppler and Doppler rate elements ($\hat{\omega}_{k+1}^{Li}$ and $\hat{\dot{\omega}}_{k+1}^{Li}$) are obtained from $\hat{\mathbf{x}}_{k+1}^{f_0}$. As a result, $\{\hat{\phi}_0\}_{k+1}^{Li}$ effectively becomes the estimate of the composite carrier phase $\{\hat{\phi}_{sOT}\}_{k+1}^{Li}$.

$\{\hat{\phi}_{sOT}\}_{k+1}^{Li}$ and $\hat{\omega}_{k+1}^{Li}$ are then used to drive the carrier reference generation as plotted in Figure 4-5 [Yang *et al.*, 2019].

4.5. AR

4.5.1. AR Scintillation Amplitude and Phase Models

In the AR, the time series of scintillation phase δ_ϕ and amplitude δ_A are approximated with AR(p) and AR(a) models, respectively, which are specified as follows:

$$\delta_{\phi,k} = \sum_{i=1}^p \beta_{\phi,i} \delta_{\phi,k-i} + \gamma_{\phi,k}; \gamma_{\phi,k} \sim \mathcal{N}(0, \sigma_{\gamma_\phi}^2) \quad (4-41)$$

$$\delta_{A,k} = \sum_{j=1}^a \beta_{A,j} \delta_{A,k-j} + \kappa + \gamma_{A,k}; \gamma_{A,k} \sim \mathcal{N}(0, \sigma_{\gamma_A}^2) \quad (4-42)$$

where $\beta_{\phi,k}$ and $\beta_{A,k}$ are the coefficients for the AR(p) and AR(a) processes, respectively. $\gamma_{\phi,k}$ and $\gamma_{A,k}$ are the process noises with variance of $\sigma_{\gamma_\phi}^2$ and $\sigma_{\gamma_A}^2$, respectively. κ is a constant value for the amplitude AR process.

In [Vilà-Valls *et al.*, 2018], the partial autocorrelation function (PAF) was used to investigate the proper order of the AR models for δ_ϕ and δ_A . To give an example, we generated a segment of δ_ϕ and δ_A time series under a strong scintillation scenario of $\{S_4=0.9, \tau_0=1.5s\}$. The sampling rate for both time series is 100Hz, corresponding to a 10ms integration time that will later be used for all the CLT implementations during evaluation. The corresponding PAFs for δ_ϕ and δ_A are plotted in the left panel and right panel of Figure 4-11, respectively. The plots show that the model orders for both processes are 3 by examining the PAF values at each lag w.r.t the confidence bound.

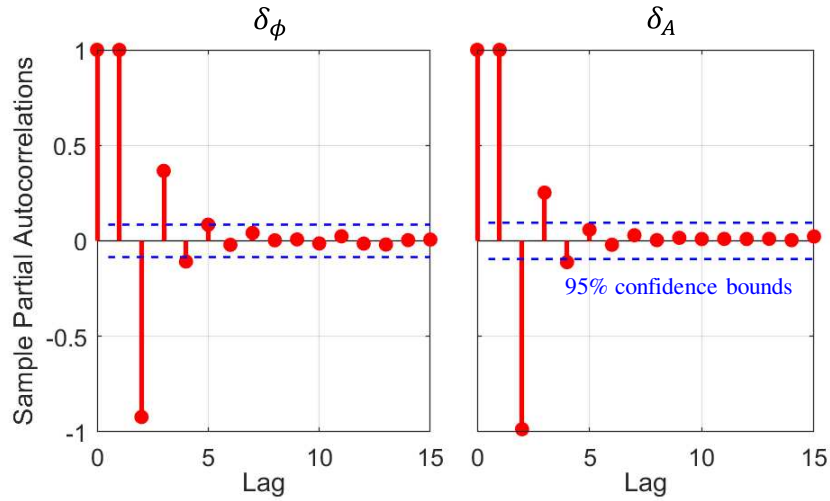


Figure 4-11. Sample PAF of δ_ϕ (left panel) and δ_A (right panel) under scintillation scenario $\{S_4=0.9, \tau_0=1.5s\}$ for AR model order selection.

With the AR model orders determined, the other parameters in (4-41) and (4-42) can be obtained by applying time-series analysis [e.g. Kay, 1993] to the simulated δ_ϕ and δ_A . To demonstrate the performance of the AR modelling for δ_ϕ and δ_A , Figure 4-12 plots the SDF of the simulated data (in blue) and the random realizations (in red) generated by AR models with parameters fitted from δ_ϕ (left panel) and δ_A (right panel). The SDF results showed reasonable agreements between the simulated δ_ϕ and δ_A and their corresponding AR models.

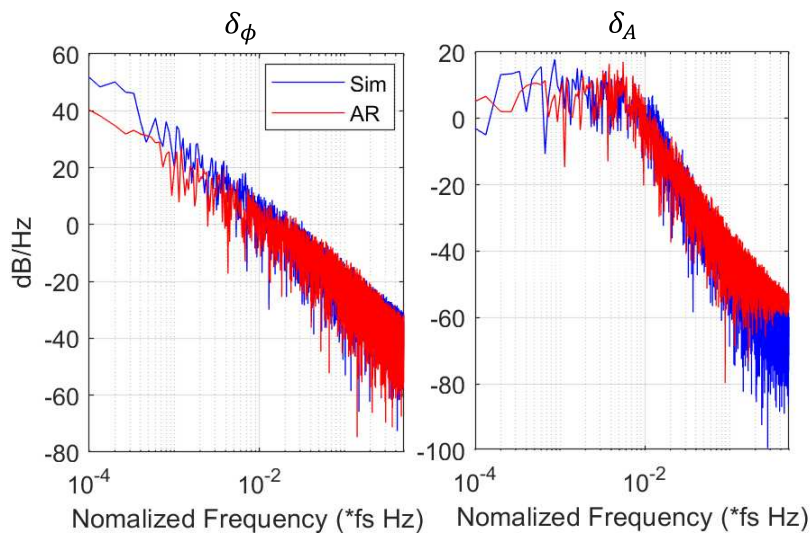


Figure 4-12. SDF of δ_ϕ (left panel) and δ_A generated under scintillation scenario $\{S_4=0.9, \tau_0=1.5s\}$ and of the realizations generated with fitted AR model.

4.5.2. AR State and Measurement Models

The AR state vector (denoted as \mathbf{x}_{AR}) is formulated by augmenting the basic KF state vector \mathbf{x}_k (defined in (4-7)) with the autoregressive process-based scintillation modelling presented in last subsection:

$$\mathbf{x}_{AR,k} = [\mathbf{x}_k \quad \delta_{\phi,k} \quad \delta_{\phi,k-1} \quad \delta_{\phi,k-2} \quad \delta_{A,k} \quad \delta_{A,k-1} \quad \delta_{A,k-2}]^T \quad (4-43)$$

The corresponding system state model is given as:

$$\mathbf{x}_{AR,k+1} = \mathbf{F}_{AR}\mathbf{x}_{AR,k} + \mathbf{k} + \mathbf{v}_{AR,k} \quad (4-44)$$

where the system noise vector is $\mathbf{v}_{AR,k} = [\mathbf{v}_k \quad \gamma_{\phi,k} \quad \mathbf{0}_{1 \times 2} \quad \gamma_{A,k} \quad \mathbf{0}_{1 \times 2}]^T$, and its covariance matrix is $\mathbf{Q}_{AR} = \text{diag}(\mathbf{Q} \quad \sigma_{\gamma_\phi}^2 \quad \mathbf{0}_{1 \times 2} \quad \sigma_{\gamma_A}^2 \quad \mathbf{0}_{1 \times 2})$. The state transition matrix is formed as follows:

$$\mathbf{F}_{AR} = \begin{bmatrix} \mathbf{F} & \mathbf{0}_{3 \times 3} & \mathbf{0}_{3 \times 3} \\ \mathbf{0}_{3 \times 3} & \mathbf{F}_\phi & \mathbf{0}_{3 \times 3} \\ \mathbf{0}_{3 \times 3} & \mathbf{0}_{3 \times 3} & \mathbf{F}_A \end{bmatrix} \quad (4-45)$$

$$\mathbf{F}_\phi = \begin{bmatrix} \beta_{\phi,1} & \beta_{\phi,2} & \beta_{\phi,3} \\ 1 & 0 & 0 \\ 0 & 1 & 0 \end{bmatrix}$$

$$\mathbf{F}_A = \begin{bmatrix} \beta_{A,1} & \beta_{A,2} & \beta_{A,3} \\ 1 & 0 & 0 \\ 0 & 1 & 0 \end{bmatrix}$$

As shown earlier, the conventional KF-based PLL and the OT both obtain the phase error estimate using a discriminator as the input to the measurement model. For AR, the measurement model is established by linearizing the nonlinear baseband signal model around the different state vector

elements. After wiping off the code component from the received baseband signal, the received baseband complex signal samples during an epoch k can be represented as:

$$\mathbf{z}_{AR,k}(\delta_{A,k}, \phi_k, \delta_{\phi,k}) = \alpha_k \delta_{A,k} \begin{bmatrix} \cos(\phi_k + \delta_{\phi,k}) \\ \sin(\phi_k + \delta_{\phi,k}) \end{bmatrix} + \begin{bmatrix} n_{i,k} \\ n_{q,k} \end{bmatrix} \quad (4-46)$$

By linearizing $\mathbf{z}_{AR,k}(\delta_{A,k}, \phi_k, \delta_{\phi,k})$ w.r.t. to the various state vector elements, the corresponding Jacobian matrix $\hat{\mathbf{H}}_{AR,k}$ can be calculated as:

$$\hat{\mathbf{H}}_{AR,k} = \begin{bmatrix} -\alpha_k \hat{\delta}_{AAR,k} \sin(\hat{\phi}_{SAR,k}) \mathbf{0}_{1 \times 2} & -\alpha_k \hat{\delta}_{AAR,k} \sin(\hat{\phi}_{SAR,k}) \mathbf{0}_{1 \times 2} & \alpha_k \cos(\hat{\phi}_{SAR,k}) \mathbf{0}_{1 \times 2} \\ \alpha_k \hat{\delta}_{AAR,k} \cos(\hat{\phi}_{SAR,k}) \mathbf{0}_{1 \times 2} & \alpha_k \hat{\delta}_{AAR,k} \cos(\hat{\phi}_{SAR,k}) \mathbf{0}_{1 \times 2} & \alpha_k \sin(\hat{\phi}_{SAR,k}) \mathbf{0}_{1 \times 2} \end{bmatrix} \quad (4-47)$$

where $\hat{\phi}_{SAR,k} = \hat{\phi}_{AR,k} + \hat{\delta}_{\phi_{AR,k}}$.

The AR state vector error can then be related to the difference between the incoming signal samples and local generated reference $\hat{\mathbf{z}}_{AR,k}$ in the measurement model as follows:

$$\Delta \mathbf{z}_{AR,k} = \mathbf{z}_{AR,k} - \hat{\mathbf{z}}_{AR,k} = \hat{\mathbf{H}}_{AR,k} \Delta \mathbf{x}_{AR,k} + \mathbf{n}_k \quad (4-48)$$

With the AR state and measurement models, the AR Kalman filter gain can be obtained in a similar fashion as the OT by solving the discrete algebraic Riccati equation. It should be noted that, since the scintillation phase $\delta_{\phi,k}$ is modelled as a separate variable in the AR state vector, the estimate of the phase element ϕ_{0k} in the AR state vector (inside \mathbf{x}_k of equation (4-7)) is effectively the estimate of the signal nominal phase ϕ_k (denoted as $\hat{\phi}_{AR,k}$).

4.6. Simulation Evaluations for SOL, OT, and AR

In this section, the carrier phase estimation performance of the three advanced algorithms is evaluated using simulated data. The simulator presented in Chapter 3 is used to generate realizations of triple-frequency scintillation data under two scenarios: a stationary platform scenario (scenario set 1) and a dynamic platform scenario (scenario set 2). For both sets of data, the receiver location is Ascension Island (7.9°S , 14.4°W), and the simulation start time is 2013/03/10, 23:30:00 UTC. PRN 31 (41° elevation, 347° azimuth) is selected as the scintillation satellite. Realizations for all scenarios share the same nominal C/N_0 and sampling rate setting: 42 dB-Hz and 5MHz for L1, 40.5dB-Hz and 5MHz for L2C, and 42.5 dB-Hz and 25MHz for L5. The differences between the nominal C/N_0 values for the three carrier frequencies are based on the transmitting powers plan for Block IIF satellites, as specified in GPS interface control document (ICD) 200H [US Air Force, 2013] and 705D [US Air Force, 2012]. This section presents the statistical results obtained using the three carrier tracking algorithms to process the two sets of simulation data. A conventional 3rd-order PLL (PIF-based) with a bandwidth of 2Hz was also implemented as a benchmark to track all the realizations in scenario set 1. The bandwidth was chosen because it was shown to be the most robust when tracking real strong scintillation data in [Xu *et al.*, 2014]. The three CLT methods (the conventional PLL, OT, and AR) all use a 10ms integration time, while for SOL, three different moving window integration times are implemented ($N_{MW} = 30\text{ms}$, 40ms , and 60ms).

4.6.1. Stationary Platform Data Set

For the stationary platform data set, three scenarios are created under various combinations of S_4 and τ_0 values, as listed in Table 4-1.

Table 4-1. The S_4 and τ_0 values (on L1) for the three scenarios of scenario set 1

Scenario #	S_4 Index	τ_0 (sec)
1a	0.7	1.5
1b	0.9	1.5
1c	0.7	0.5

As can be seen in Table 4-1, scenario 1a is the mildest case among the three scenarios with a lower S_4 Index and slower decorrelation time, while 1b has stronger amplitude scintillation and 1c has the shortest decorrelation time. A total of 25 realizations of data, each with 300s length, were simulated for each scenario. Figure 4-13 plots examples of triple-frequency signal intensities (SI) (left panels) and δ_ϕ (right panels) of the three scenarios (1a in top row, 1b in middle row, and 1c in bottom row), with L1 in blue, L2 in green, and L5 in red.

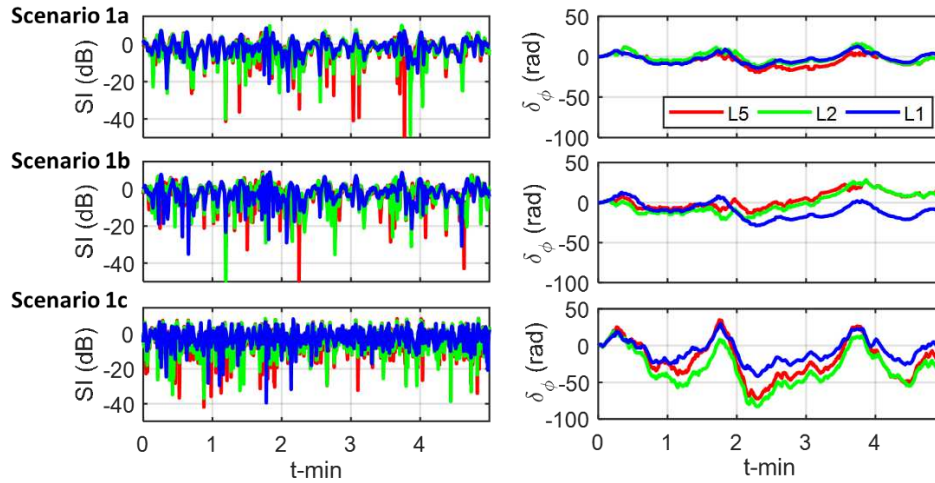


Figure 4-13. Examples of triple-frequency SI (left panels) and δ_ϕ (right panels) of the three scenarios (1a in top row, 1b in middle row, and 1c in bottom row). The results of different frequencies are plotted in different colors: L1 in blue, L2 in green, and L5 in red.

Figure 4-13 shows that among the three frequencies of signals, L1 has the mildest amplitude fading due to its highest carrier frequency [Rino *et al.*, 2018]. Comparing 1a and 1b, the larger S_4 value corresponds to deeper fading and slightly larger variations in δ_ϕ . Comparing 1a and 1c, faster

decorrelation clearly results in more frequent fading and a more rapid varying $\delta\phi$. A zoom-in version of the SI in Scenario 1a is given in Figure 4-14. The asynchronous nature among the fading on the three frequencies is clearly shown in the figure. This is especially true between L1 and the other 2 frequencies, which is the motivation behind the multi-frequency tracking approach for ionospheric scintillation.

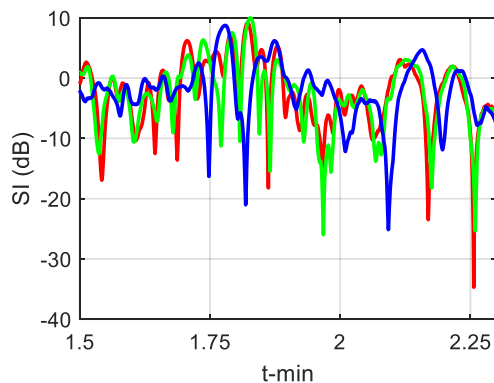


Figure 4-14. Zoom-in of the SI in Scenario 1a.

For each scenario, based on the carrier phase estimation results obtained from the 25 realizations, the RMSE of ϕ_s and average cycle slip occurrence rate (per minute) obtained for the four algorithms (conventional PLL, AR, OT, and SOL) are plotted in Figure 4-15. For SOL, three N_{MW} values (30ms, 40ms, and 60ms) were implemented, which are abbreviated as SL₃₀, SL₄₀, and SL₆₀, respectively, in Figure 4-15.

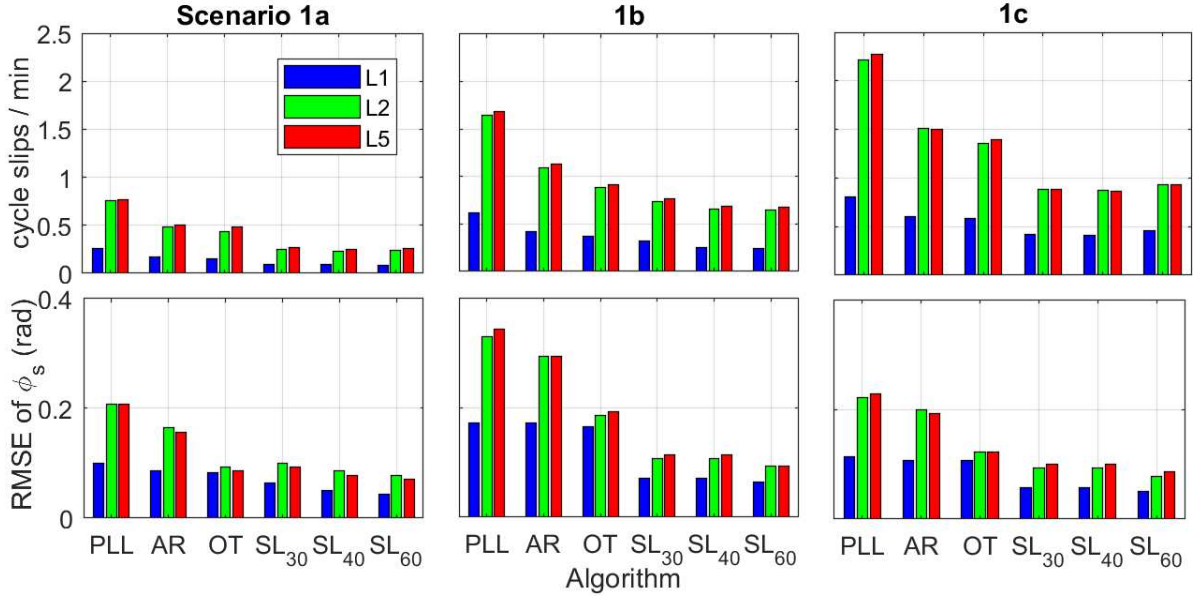


Figure 4-15. Cycle slip occurrence rate (per minute) and RMSE on ϕ_s using different algorithms for Scenario 1a-c.

From Figure 4-15, we observe the following:

1) For all algorithms, the cycle slip rate of L2 and L5 signals are both about 2~3 times of those of the L1 signals. For all algorithms except OT, the RMSE for L2/L5 is also about 2~3 times of that of L1. For OT, its L2 and L5 RMSEs are similar to that of L1. This confirms that with the inter-frequency aiding mechanism of OT, the more severe scintillation fading on L2 and L5 are mitigated with the aiding of the less affected L1 signals.

2) Among the algorithm implementations presented, the SOL showed the best performance in cycle slip rate and RMSE. This finding confirms the benefit of the moving window processing enabled by an open-loop architecture. A larger N_{MW} leads to only a slight improvement in RMSE. The second-best-performing algorithm is the OT. The AR also showed considerable improvement in cycle slip reduction compared to the traditional PLL, whereas its RMSE improvement over the traditional PLL is not as large as that of the OT.

3) Among the three scenarios tested, a shorter decorrelation time results in a higher cycle slip occurrence rate due to the more frequent fading, but it does not have a considerable effect on the RMSE result. A larger S_4 value results in both a larger RMSE and more cycle slip occurrences for all algorithm implementations except the SOL. For the three SOL implementations, the increased S_4 value only causes more cycle slip occurrences, but it does not have considerable impact on the RMSE.

The estimation accuracy of AR on the signal nominal carrier phase ϕ_k is also evaluated, which is of great interest for high precision positioning applications. In all three scenarios, there is no cycle slip occurrence in the nominal phase estimate $\hat{\phi}_{AR,k}$, while the RMSEs are approximately a third of the RMSE values of $\hat{\phi}_{SAR,k}$. This validates AR as a feasible approach to mitigate the scintillation-induced error on carrier phase-based range measurements for positioning.

4.6.2. Dynamic Platform Data Set

Similar to the dynamic platform scenario configuration presented in [Xu et al., 2017], by maintaining the same receiver speed and manipulating the receiver moving direction, dynamic scenarios with a decorrelation time range much wider than that of a stationary platform (typically 0.5s to 1.5s) can be simulated. Table 4-2 lists the receiver velocity vectors, S_4 and τ_0 values on the L1 signal in four simulated dynamic scenarios. These four scenarios all have the receiver moving at the same speed of 150m/s, which is typical for a civil aircraft.

Table 4-2. The receiver velocity vectors, S_4 and resulting τ_0 values on the L1 signal in four simulated dynamic scenarios

Scenario #	[Eastward Northward Upward] velocity in m/s	S_4 Index	τ_0 (sec)
------------	---	-------------	----------------

2a	[-150 0 0]	0.7	3
2b	[-150 0 0]	0.9	2.4
3a	[150 0 0]	0.7	0.28
3b	[150 0 0]	0.9	0.26

In order to have more realistic platform dynamics, a constant acceleration of 0.5g was added to the platform trajectories at 30-65 seconds, increasing the receiver speed from 0 m/s to 150 m/s, and at 270-300 seconds, bringing the receiver speed back to 0 m/s. The resulting Doppler variations for the four scenarios are plotted in Figure 4-16.

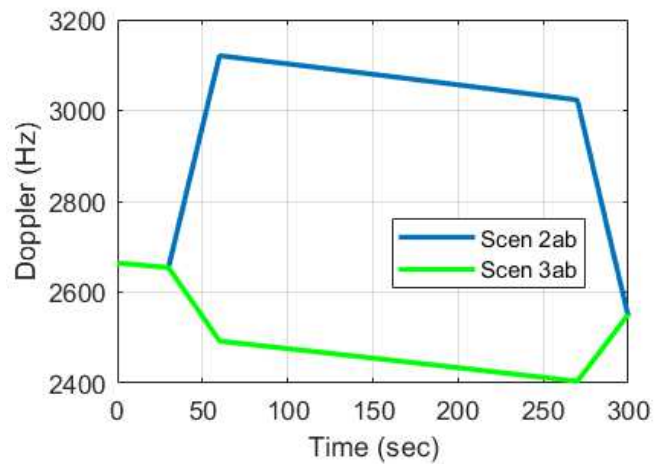


Figure 4-16. Simulated Doppler for the four dynamic scenarios.

Again, for each scenario, 25 realizations of 300s data were generated and processed by the same 4 algorithms as in subsection 4.6.1. The conventional PLL couldn't maintain lock during any of the realizations in Scenario 3b and during 10 realizations in Scenario 2b. Therefore, the average cycle slip occurrence rate (per minute) and RMSE on ϕ_s are obtained for the other 3 algorithms and plotted in Figure 4-17 and Figure 4-18, respectively.

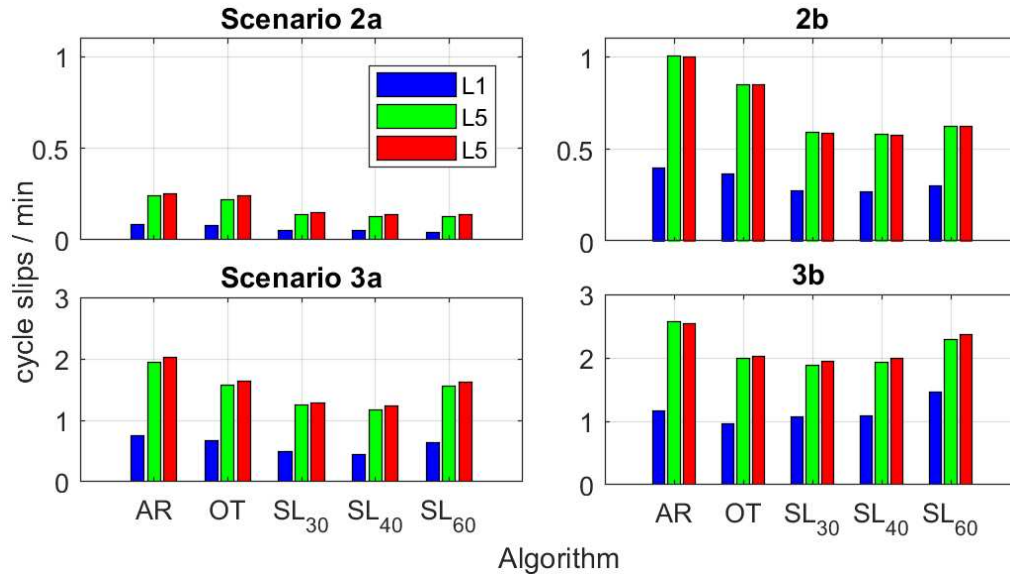


Figure 4-17. Cycle slip occurrence rate (per minute) on the estimation error of ϕ_s using different algorithms for Scenario 2ab and 3ab.

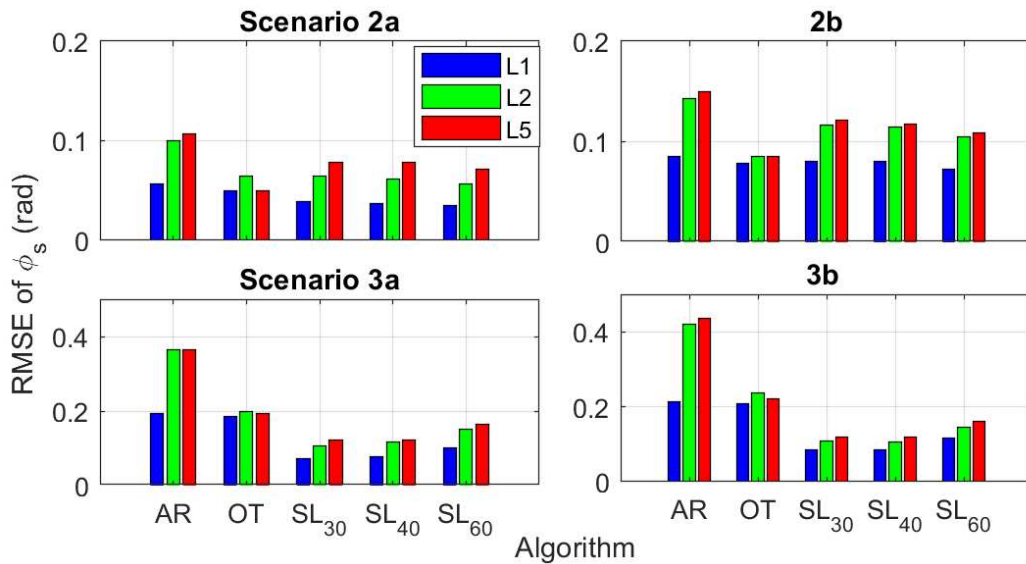


Figure 4-18. RMSE on the estimation error of ϕ_s using different algorithms for Scenario 2ab and 3ab.

Figure 4-17 and Figure 4-18 show that most of the observations made for the stationary platform scenarios discussed earlier are applicable to the dynamic scenarios as well. A notable difference is that the τ_0 values have a considerable effect on the RMSE and the cycle slip occurrences: a

shorter τ_0 corresponds to larger RMSE and more cycle slips. Among the three SOL implementations, the SL₆₀ implementation clearly showed more cycle slip occurrences than the other two implementations in Scenario 3a and b, indicating that a shorter integration time is more suitable for scintillation with a faster decorrelation time.

4.7. Simulation Evaluations for Different VDFLL Implementations

This section evaluates the performance of a VDFLL-based GNSS receiver under different satellite weighing implementations on dynamic platforms while operating during strong equatorial scintillation.

4.7.1. Different Satellite-weighing Implementations

This section describes the three strategies to adjust the weights on the measurements from scintillating and non-scintillating satellites in the VDFLL. Considering the geometry matrix \mathbf{G} (defined in (4-33)) practically invariant between adjacent update and prediction epochs, the calculation of the EKF gain is only dependent on the choice of \mathbf{Q}_γ , \mathbf{R}_E . As mentioned earlier, for a KF with fixed \mathbf{Q}_γ and \mathbf{R}_E , the filter gain will gradually reach a steady state when it converges to a stable gain, which is the so-called steady-state Kalman gain. In this study, the first two implementations (VTL1 and VTL2) utilize a fixed \mathbf{Q}_γ , \mathbf{R}_E in the calculation of Kalman gain. The third implementation (VTL3) uses a fixed \mathbf{Q}_γ , while adaptively updating \mathbf{R}_E based on the real-time C/N_0 estimates of different satellites' signals for Kalman gain calculation at each tracking epoch. The different implementation details are summarized as follows:

- 1) VTL1 excludes the satellites affected by scintillation from the vector tracking. The fixed \mathbf{R}_E is obtained using equation (4-32) based on the simulated nominal C/N_0 values of

all remaining healthy satellites. This implementation prioritizes the quality of the input measurements and the resulting feedback to the VTL over the concern of a bad geometry in navigation performance.

- 2) VTL2 tracks all satellites. However, when calculating the fixed \mathbf{R}_E , different C/N_0 values are used for healthy satellites and scintillation-affected satellites. For the healthy satellites, the corresponding σ_ρ^2 and $\sigma_{\dot{\rho}}^2$ values in \mathbf{R}_E are calculated based on the simulated nominal C/N_0 values. For the scintillation-affected satellites, the corresponding noise variance values are calculated based on a low C/N_0 value of 15 dB-Hz. This will effectively result in constant low weights in the steady-state EKF gain for the measurements from scintillation-affected satellites to reduce the degradation on the measurement quality.
- 3) VTL3 tracks all satellites with an adaptive gain. This is achieved by updating the \mathbf{R}_E according to the real-time, high-rate estimates of the signal C/N_0 values of different satellites. The steady-state EKF gain is then obtained by iterating the Kalman gain update and projection steps 50 times with the updated \mathbf{R}_E at each epoch. This is because the amplitude fading during strong equatorial scintillation introduces large and swift changes in the signal C/N_0 values. In order to promptly adapt to the fast signal C/N_0 changes, it is necessary to apply the iterations to expedite the adjusting of the EKF gain with the updated \mathbf{R}_E .

4.7.2. Simulation Configuration

In this section, Simulated data with multi-satellite scintillation signals observed on a dynamic platform was generated to assess the PVT estimation performance of the different implementations. The model parameters of the ionospheric structures for simulation were obtained from a segment of ground initialization data, which contains strong scintillation observed from multiple satellites spreading a large part of the sky. A sky view of all visible satellites (under an elevation mask of 10°) during 2013/03/10, 23:00:00-00:30:00 UTC at Ascension Island (7.9°S , 14.4°W) is given in Figure 4-19. The tracks are color-coded w.r.t. the S_4 index on the corresponding L1 signals processed by a Septentrio PolaRxS ISM receiver. The satellite track segments defined by the rectangles correspond to the 10-minute duration of the initialization data used in this study (23:30:00-23:40:00 UTC). As can be clearly seen in Figure 4-19, out of the 9 visible satellites, 5 satellites contain strong scintillation of maximum S_4 index over 0.9 during the selected 10 minutes (defined by rectangles in red): PRN 3, 6, 14, 19, and 31. The strong scintillation data of these 5 satellites are used to derive their phase screen model parameters using IPE for scintillation wave field (δ_ϕ and δ_A) simulation.

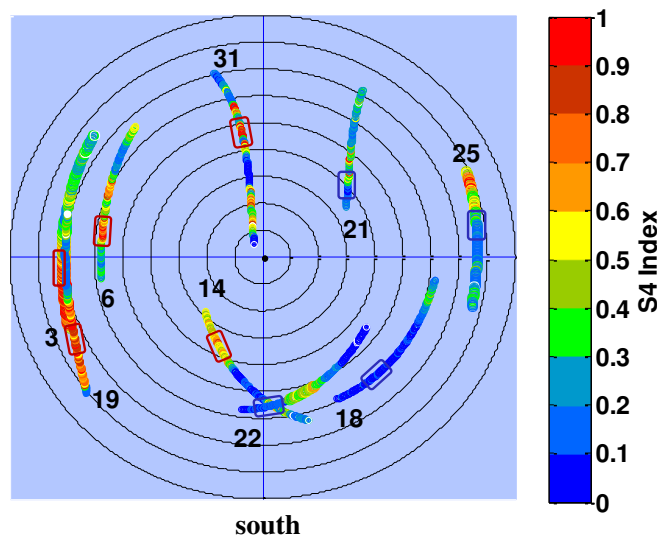


Figure 4-19. Sky view plots of all visible satellite (SV) tracks during 11:00 PM–12:30 AM UTC on March 10 on Ascension Island with an elevation mask of 10°. The tracks are color-coded by the values of the S_4 index on L1. The ends with PRN numbers represent the starting points of the tracks. The track segments defined by the rectangles correspond to the duration of the initialization data.

In the simulated IF data, signals from all 9 visible satellites in the initialization data are simulated using their corresponding satellite orbit information. For the 5 satellites with strong scintillation, scintillation wave fields are simulated based on the derived parameters and the propagation geometries defined by satellite orbit information and platform trajectory. Different configurations of scintillation satellites are then created by selecting different subsets of these five satellites in order to evaluate the VTL implementations with different GDOPs (geometric dilution of precision). For each configuration, only the signal of each satellite within the subset is modulated with the corresponding scintillation wave field. Three configurations of scintillation satellites used in this study is summarized in Table 4-3, with the corresponding GDOPs for VTL1 which discards the scintillation satellite measurements. It should be mentioned for VTL2 and VTL3 that utilize all satellites, the GDOP remains 2.0 for all configurations. For the other 4 satellites with moderate (PRN21) or no scintillation (PRN 18, 22, 25), nominal signals are simulated.

Table 4-3. Three configurations of scintillation satellites used in the simulation of evaluation data

Config. #	scintillation PRNs	VTL1 GDOP
1	3, 6, 19	3.6
2	3, 6, 14, 19	4.2
3	3, 6, 14, 19, 31	6.0

The velocity vector (E-east, N-north, U-up) during the platform trajectory used in this study is plotted in Figure 4-20. As can be seen in Figure 4-20, an eastward constant acceleration of 0.5g was added to the platform trajectory at the 70-120 seconds and 550-600 seconds for platform dynamics simulation, resulting in a maximum speed of 250m/s which is typical for a civil aircraft.

The origin of this platform trajectory is set at the same position of the stationary receiver where the initialization data was collected. During the 10 minutes of trajectory, the variation on the satellite geometry illustrated in Figure 4-19 is considered negligible, because the distance between the origin and the destination is less than a percent of a typical range between GPS satellites and an aircraft receiver.

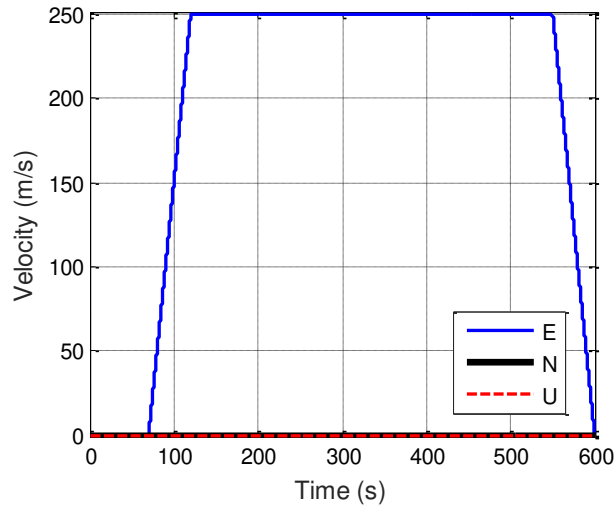


Figure 4-20. The platform velocity vector during the 10-min-trajectory.

Based on the propagation geometry define by the dynamic trajectory and the satellite orbit information, and the extracted model parameters, scintillation phase and SI of the 5 satellites with strong scintillation are simulated and given in Figure 4-21:

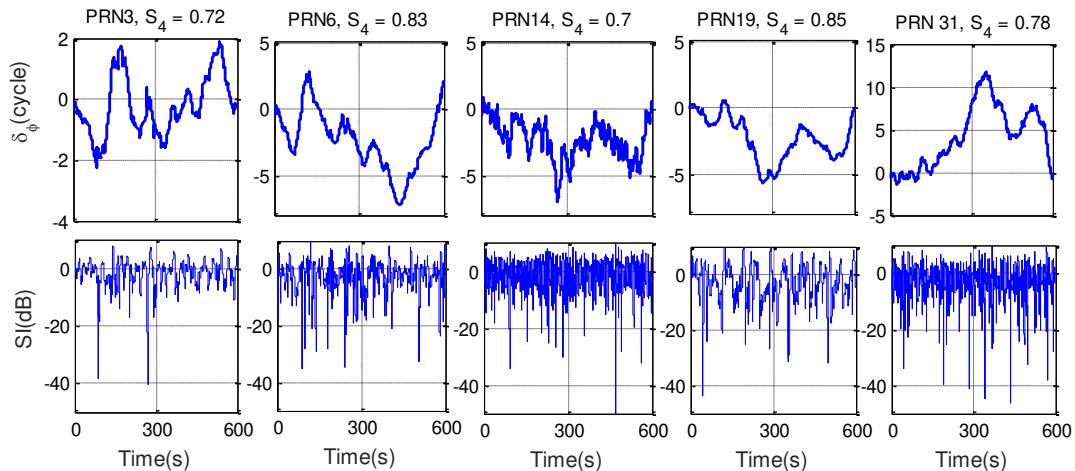


Figure 4-21. The simulated scintillation phase ($\delta\phi$) and SI of the 5 satellites with strong scintillation based on initialization data.

As can be seen in Figure 4-21, the simulated scintillation $\delta\phi$ goes up to 10 cycles on PRN 31, resulting in the largest error of around 2 meters in the ranging code among all 5 satellites, whereas PRN3 has the smallest code error of about 0.3 meters. PRN 6, 14, and 19 have similar code error of around 1 meter. The SI results showed deep fading close to or over -40 dB on all 5 satellites. PRN 3, 6, and 19 are clustered in the far west area of the sky and therefore have comparatively close propagation geometries. They showed amplitude fading of noticeably slower variation than the fading on PRN 14 and PRN 31 which are further apart in the sky.

4.7.3. Evaluation Results

In this section, navigation performance of the three VTL implementations are evaluated using the simulated IF data under different configurations. The comparison between the errors in positioning (in ENU coordinates) and clock bias using the three implementations under configuration 3 is given in Figure 4-22 as an example:

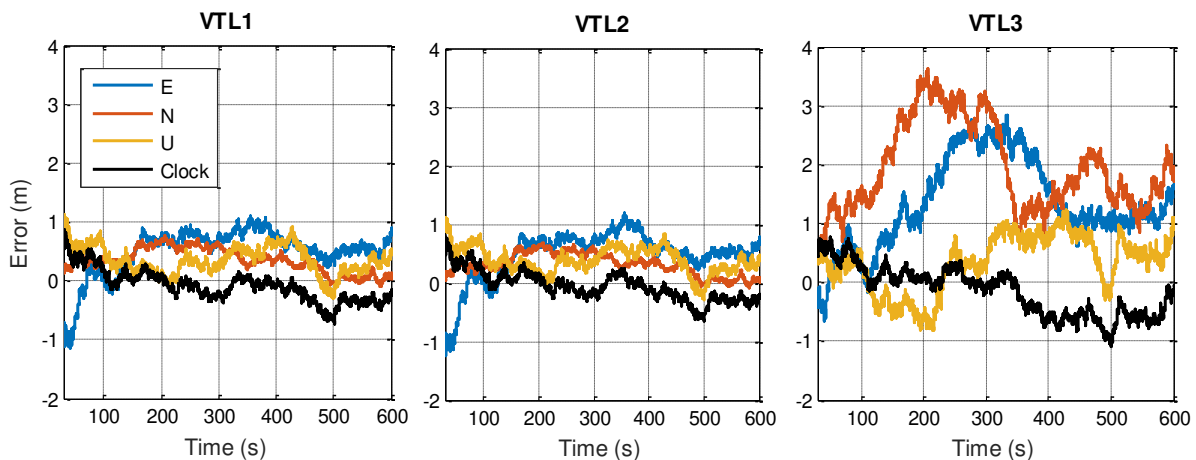


Figure 4-22. Comparison between the errors in positioning (in ENU coordinates) and clock bias using the three implementations under Config. 3.

As can be seen in Figure 4-22, the VTL1 and VTL2 implementations showed similar results of errors bound within -1m ~ 1m on all E, N, U directions and clock bias. This finding suggests that keeping the measurements from scintillation-affected satellites with constant low weight (calculated with a low C/N_0 of 15 dB-Hz) in the VTL tracking is essentially equivalent to simply discarding the measurements. The adaptive approach VTL3 showed the largest error among the three implementations of exceeding 3 meters on the north direction. The RMSE of the position and clock bias results (denoted as $RMSE_P$ in meters) and the velocity and clock drift results (denoted as $RMSE_V$ in meters) are calculated as:

$$RMSE_P = \sqrt{\text{mean}(\Delta E_{RX}^2 + \Delta N_{RX}^2 + \Delta U_{RX}^2 + \Delta \delta t_{RX}^2)} \quad (4-49)$$

$$RMSE_V = \sqrt{\text{mean}(\Delta \dot{E}_{RX}^2 + \Delta \dot{N}_{RX}^2 + \Delta \dot{U}_{RX}^2 + \Delta \delta \dot{t}_{RX}^2)} \quad (4-50)$$

where Δ means differencing the corresponding navigation result with the truth from the simulator.

The RMSE results obtained using all three VTL implementations through the data of three configurations are given in Table 4-4:

Table 4-4. RMSE results using three VTL implementations for three configurations of simulated data

	Config.	1	2	3
	GDOP	3.6	4.2	6.0
$RMSE_P$ (m)	VTL1	0.38	0.41	0.97
	VTL2	0.38	0.40	0.94
	VTL3	0.69	0.80	2.6
$RMSE_V$ (m/s)	VTL1	0.11	0.12	0.13
	VTL2	0.11	0.11	0.13
	VTL3	0.08	0.08	0.10

As can be seen in Table 4-4, the results showed that for all VTL implementations the more satellites affected by strong scintillation, the worse the positioning performance. VTL1 and VTL2 showed

similar positioning performance with $RMSE_p$, whereas the $RMSE_p$ of VTL3 is over twice of those of the VTL1 and VTL2. This is because on the scintillation-contaminated signals, the magnitude of the scintillation-induced errors on the signal code phase are uncorrelated with the amplitude fading pattern, as can be clearly seen in Figure 4-21. This means that during the times when the signal recovers from deep fading to a nominal or even enhanced signal power, the present scintillation-induced code error will harm the positioning accuracy more in VTL3, due to its C/N_0 -based Kalman gain adjusting strategy.

The $RMSE_v$ results of all three implementations indicate that the VTL3 outperforms VTL1 and VTL2 in accuracy of velocity estimation. To explain this finding, a segment of the scintillation induced frequency error (δf in Hz) and SI of the PRN 6 signal in the simulation data is given in Figure 4-23.

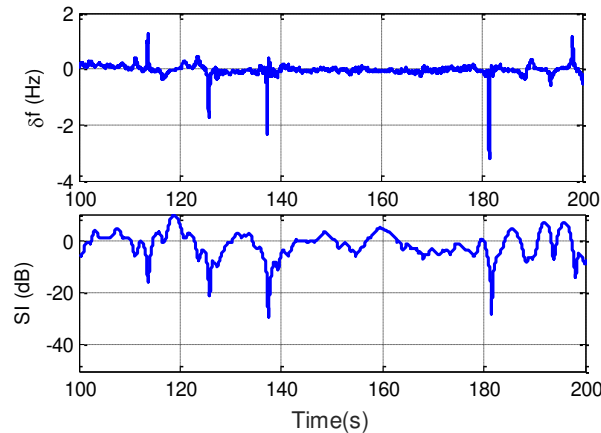


Figure 4-23. A segment of δf and SI results of the PRN 6 signal in the simulation data.

As can be seen in Figure 4-23, the magnitude of the δf is clearly positively correlated with the amplitude fading pattern: the deeper the fading, the larger the scintillation-induced frequency error.

Therefore, in contrast to the positioning performance, the C/N_0 -based adaptive Kalman gain adjusting in VTL3 can benefit the velocity estimation accuracy.

In order to further confirm the explanations given above, another configuration of data is simulated where all five satellites have amplitude fading but no scintillation phase. Only VTL2 and VTL3 are used to track this data, since this data will result in the same results for VTL1 as the Config. 3 data. The results are given in Table 4-5, which showed similar performance between VTL2 and VTL3 in both positioning and velocity estimation and validated the explanations for VTL3's outperformance in $RMSE_V$ and bad performance in $RMSE_P$.

Table 4-5. RMSE results using VTL2 and VTL3 for the simulated data with amplitude fading and no scintillation phase

$RMSE_P$ (m)	VTL2	0.89
	VTL3	0.87
$RMSE_V$ (m/s)	VTL2	0.10
	VTL3	0.10

4.8. Concluding Remarks

This chapter presents and evaluates the performance of SOL, AR, and OT, in terms of cycle slip performance and carrier phase RMSE. Data sets for stationary and dynamic platforms are created for evaluation, each set containing several combinations of S_4 and τ_0 values, in order to comprehensively test these three algorithms and to assess how different values of the input scintillation indicators affect the tracking results.

The results confirmed that all algorithms demonstrated robustness and considerable accuracy improvement over the traditional 3rd-order PLL. The SOL works best in terms of having the lowest cycle slip occurrences and RMSE. The OT works better than the AR. However, the AR estimates

the nominal signal carrier phase separately from the scintillation signal composite phase with reasonable accuracy, which makes it a promising direction to pursue for high accuracy positioning applications under challenging conditions.

In addition, this chapter also evaluated the PVT performance of a vector-based GNSS receiver under different satellite weighing implementations on dynamic platforms while operating during strong equatorial scintillation. The results show during strong equatorial scintillation, simply dropping the scintillation-contaminated measurements achieves a better performance in positioning than the adaptive approach even with its much worsened GDOP.

5. CHAPTER 5 – SIMULATING AND TRACKING SCINTILLATION SIGNALS ON LEO SATELLITES

This chapter first presents simulation results using the developed simulator for the scintillation signals observed on a LEO satellite platform. Two different scenarios were created, where the scintillation signal is received on the zenith-looking POD antenna or received on the limb-scanning radio occultation RO antenna. The simulation results showed different characteristics of scintillation between the two scenarios. The simulation data of these two scenarios were then used to evaluate the AKF algorithm against a conventional PLL of different integration times and bandwidths.

5.1. Scintillation Signal Simulation on LEO Satellites

A segment of initialization data was used in this study to derive the phase screen model parameters and drive the simulator. The data was collected by a Septentrio PolaRxS ISM receiver at Hong Kong (22.21°N, 114.26°E, 59.7 m). The signal used is GPS PRN 24 L1 CA signal collected on 2013/10/05, 12:49:29-12:54:29 UTC. The data showed strong scintillation with deepest fading close to -40dB, average S_4 index of around 0.8, and average σ_ϕ of around 0.1 cycles.

As has been discussed in section 3.1, among the ensemble of parameters that jointly determine a realization of the scintillation wave field in this simulator, only the time scaling factor ρ_F/v_{eff} is affected by the dynamics of the platform and the propagation geometry. ρ_F/v_{eff} can be significantly different between the case of a LEO satellite and that of a ground receiver by a few orders of magnitude. As has been shown in Chapter 3, the time scale factor directly affects the decorrelation time of the scintillation signal. A small ρ_F/v_{eff} corresponds to a small

decorrelation time, which is associated with faster temporal variations in the scintillation signal amplitude and phase.

5.1.1. LEO Propagation Geometry Setup

The platform dynamics and the propagation geometry that directly affect the ρ_F/v_{eff} calculation include: the propagation distance r_p between the IPP and the receiver, the geometric range r between the satellite and the receiver, and different velocities such as the signal LOS scan velocity of at the IPP (v_{IPP}) and the drift velocity of the ionosphere irregularities (v_{drift}). In order to gain an intuitive understanding into the relationship between the ρ_F/v_{eff} and the different scenarios of LEO operation, a one-dimensional illustration of the propagation geometry is given in Figure 5-1. Two scenarios are depicted: the scenario where the scintillation signal is received on a zenith-looking POD antenna (in blue, denoted as Scenario 1), and the scenario where the scintillation signal is received on a RO antenna (in yellow, denoted as Scenario 2).

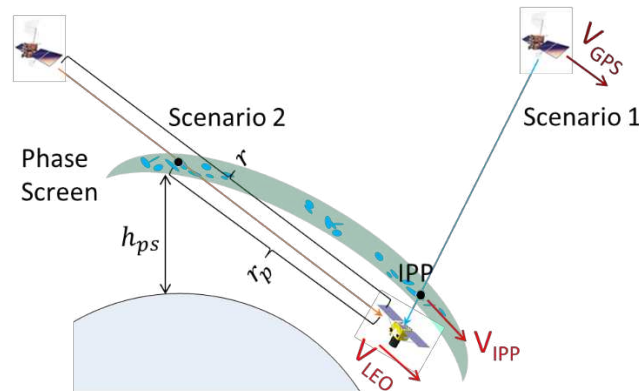


Figure 5-1. One-dimensional illustration of the propagation geometry of the two scenarios of scintillation signals received on LEO satellites. The distance between the GPS satellite and the phase screen is greatly understated for easy visualization.

As can be seen in Figure 5-1, in the propagation geometry of a LEO satellite, there are two user-specified factors, the h_{ps} and the GPS satellite elevation (el), that can be used to manipulate r_p ,

r , and v_{IPP} to yield different values of ρ_F/v_{eff} . When the LEO satellite travels very close to the IPP as in Scenario 1, the high speed of LEO satellite is fully projected onto v_{IPP} as the dominant component. As a result, a ρ_F/v_{eff} much smaller than that of the ground observation is yielded, which will generate a scintillation field with variations in the order of several tens or even hundreds of times faster than those from ground observed scintillation. For Scenario 2, the r_p is much larger than that that of Scenario 1, the scintillation variation will be slower.

In order to quantitatively demonstrate how ρ_F/v_{eff} is influenced by the propagation geometry in these two scenarios, and to set up the scintillation data simulation for later algorithm evaluation, Table 5-1 lists different geometry setups and the resulting ρ_F/v_{eff} values. For all cases, a common eastward v_{drift} of 100m/s is added in the calculation, which is a typical value for equatorial regions.

Table 5-1. Different scenarios of geometric and dynamics setup and the resulting r_p and ρ_F/v_{eff} values.

Scen. #	RX alt. (km)	RX speed (km/s)	Avg. el (deg)	h_{ps} (km)	r_p (km)	Avg. ρ_F/v_{eff} (s^{-1})	
0	0.06	0	46	350	475	1.18	
1	(a)	500	7.6	40	500.05	0.1	0.001
	(b)				505	9.4	0.005
	(c)				700	368	0.02
2	500	7.6	-5	700	1133	0.06	

In Table 5-1, Scenario 0 has the same geometry of the initialization data for comparison with the LEO scenarios: Scenario 1(a)-(c), and 2. For these LEO scenarios, a common altitude of 500km and an eastward speed of 7.6km/s are chosen for the LEO-borne receiver, which are approximately

the altitude and speed of the ESA Swarm satellites. The longitude and latitude of the receiver stay the same as those of the initialization data.

For Scenario 1 (a)-(c), the GPS satellite trajectory remains the same as in Scenario 0, and the difference in the el is due to the difference in receiver altitude. The h_{ps} is manipulated among Scenario 1(a)-(c) to obtain different ρ_F/v_{eff} values. Scenario 1(a) corresponds to the case where the LEO satellite is essentially traveling inside the irregularities, and results in the smallest ρ_F/v_{eff} down to 1/1000 of the ground observed ρ_F/v_{eff} . As the phase screen is moved further above the LEO satellite for (b) and (c), ρ_F/v_{eff} grows to around 1/200 and around 1/60 of the ground ρ_F/v_{eff} , respectively.

As for Scenario 2, the GPS satellite trajectory is selected from PRN 24 during a later time the same day, when PRN24 is setting in order to achieve an average el of -5 degree as the RO scenario. A ρ_F/v_{eff} of 1/20 of the ground ρ_F/v_{eff} is obtained for Scenario 2.

5.1.2. Simulation Results for Different LEO Scenarios

Based on these different geometric setups, scintillation simulation data each of 5 minutes in length were generated for all scenarios. It should be stressed that all user input items other than the geometric and dynamics parameters listed in Table 5-1 are the same for the simulation of all scenarios. The normalized SI results of all the simulated data are plotted in Figure 5-2 (a) with their corresponding average S_4 indices given in the legend, and Figure 5-2 (b) gives a zoomed-in version of Figure 5-2 (a).

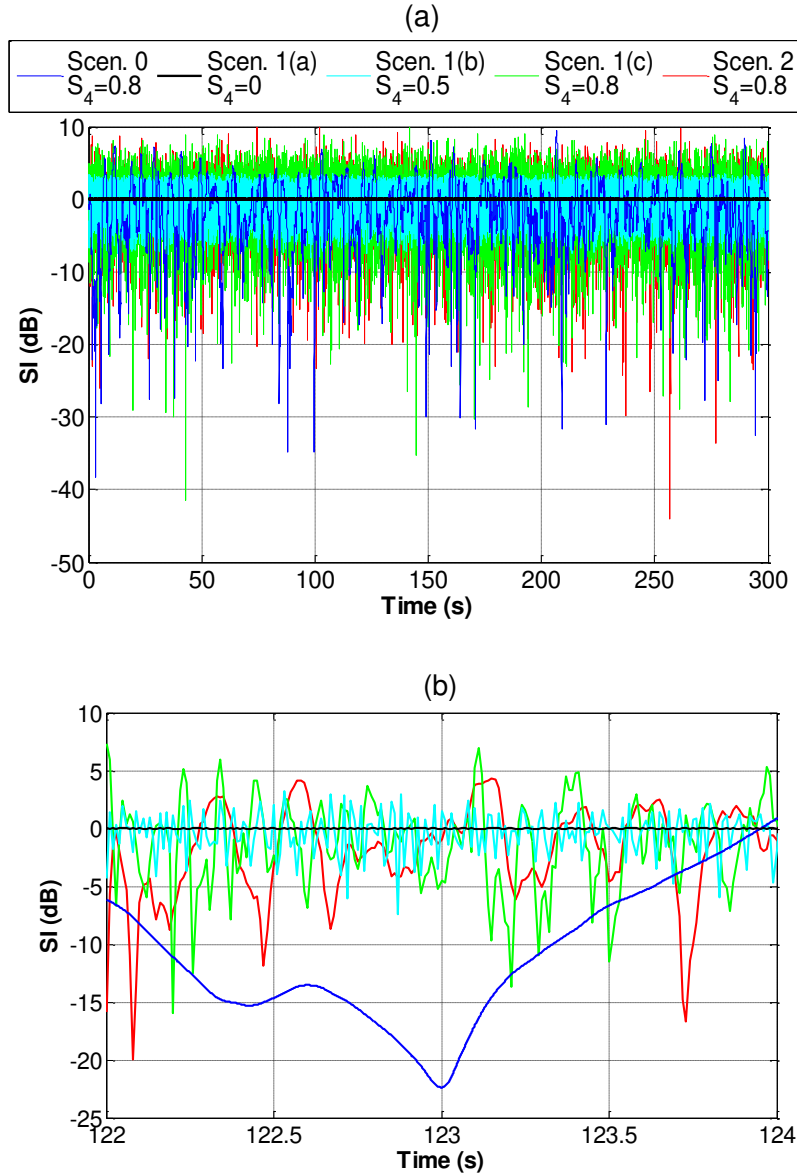


Figure 5-2. Normalized SI results of the simulated data for all cases listed in Table 5-1.

From Figure 5-2 (b), it can be seen that as the ρ_F/v_{eff} decreases (starting from Scenario 0, to Scenario 2, and then Scenario 1 (c) – (a)), the fading becomes shorter and shallower with a higher rate of occurrence. The extreme case is the Scenario 1 (a), where the fading is not discernable. The relationship between r_p and the average S_4 indices of different cases is noteworthy. From Scenario 1(a) to (c), the average S_4 value clearly grows as the r_p grows. However, for the

scenarios with a large r_p , Scenario 1 (c) and Scenario 2 all show similar average S_4 value of 0.8 as the Scenario 0 and the initialization data, despite the considerable differences in r_p among these scenarios. In order to look into this matter, more choices of h_{ps} were added under Scenario 1 to manipulate r_p , and a relationship between the average S_4 and r_p is then obtained and plotted in Figure 5-3.

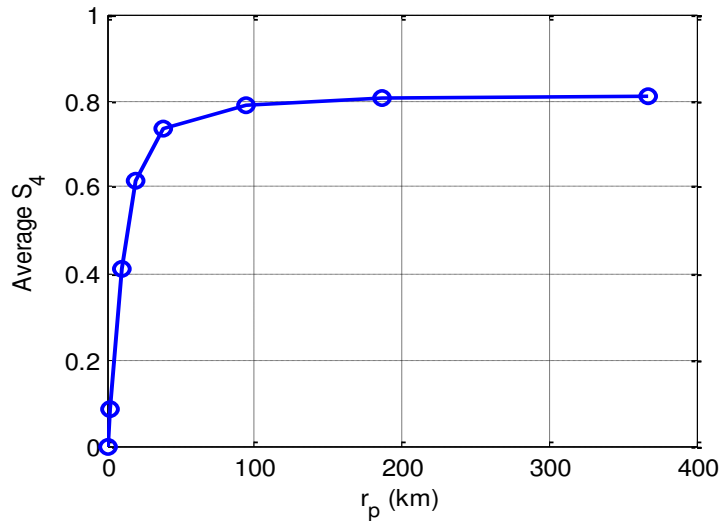


Figure 5-3. Relationship between the average S_4 and r_p under Scenario 1.

Figure 5-3 shows that the average S_4 increases with a growing r_p , but after r_p grows above 200km, the average S_4 reaches a saturating value of 0.8 close to that of the initialization data. This finding clearly suggests that the phase screen spectral parameters from the initialization data places an upper bound on the simulated amplitude scintillation intensity. The r_p value where the S_4 index saturates is likely to be dependent on both the propagation geometry and the ionospheric structure. More research is required to investigate this matter.

The scintillation induced phase (δ_ϕ) for all scenarios are plotted in Figure 5-4. In order to see better how fast the phase changes, the phase change rate $\Delta\delta_\phi/\Delta t$ (in Hz) is obtained from the scintillation induced phase, and a segment of the $\Delta\delta_\phi/\Delta t$ result is plotted in Figure 5-5.

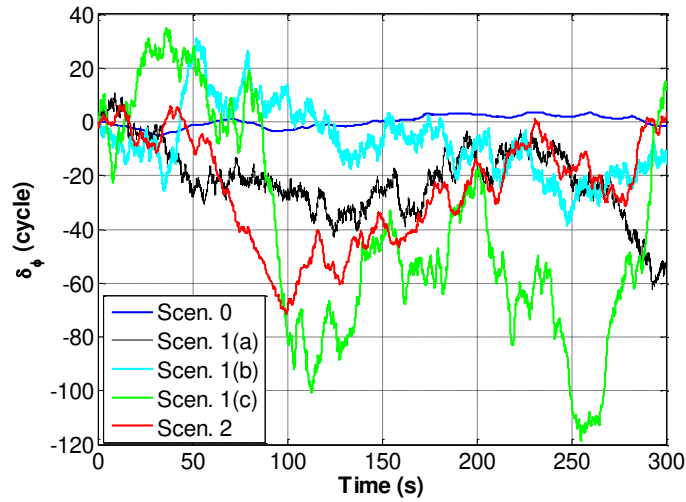


Figure 5-4. δ_ϕ of the simulated data for all cases listed in Table 5-1.

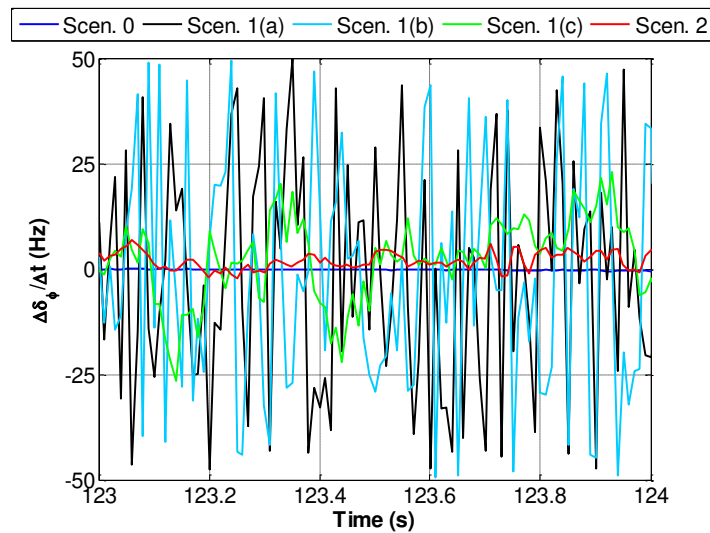


Figure 5-5. The scintillation phase change rate of the simulated data for all cases listed in Table 5-1. Zoomed in between 123s and 124s.

As can be seen in Figure 5-5, as the ρ_F/v_{eff} decrease, the phase rate shows more violent variations and a larger range. For Scenario 1 (a)(b) with an extremely small ρ_F/v_{eff} , the phase rate constantly varies between down to -50Hz and up to 50Hz.

Combining the amplitude scintillation results from Figure 5-2 (a)(b) and the scintillation phase change results in Figure 5-5, it can be reasonably deduced that the most severe challenging scenario should be the Scenario 1 (b)(c), both containing simultaneous violent phase changes and amplitude fading. The Scenario 1 (a) essentially shows no amplitude scintillation, therefore the phase scintillation can be handled with a large carrier tracking loop bandwidth. The same suggestion can be made from the report in [Xiong *et al.*, 2016] that the loss of lock of signals from Swarm satellites POD antenna was resolved by increasing the receiver carrier tracking bandwidth.

Ten realizations of GPS L1 data of 300s in length are simulated for each of Scenario 1(b)(c) and Scenario 2. A nominal C/N_0 of 42 dB-Hz is achieved in the simulation data by adding white Gaussian noise. The sampling rate is set to 5MHz. The three sets of data will be used in the next section to evaluate the AKF algorithm and a conventional PLL with different loop parameters.

5.2. Scintillation Signal Tracking on LEO Satellites

This section presents the evaluation results on two different carrier tracking algorithms based on the three sets of simulation data mentioned earlier. The two carrier tracking algorithms are both 3rd-order PLLs implemented with different types of PLL filter. The first filter design is the AKF approach described in section 4.1.4. The simulator used in this study does not include the oscillator effects. However, phase scintillation effects are known to be similar to oscillator noise effects. In order to include the scintillation induced carrier dynamics into the AKF models, the scintillation

phase variations are treated as equivalent oscillator noise effects by using heuristically chosen h parameters to model scintillation phase and frequency noise terms in the system noise covariance matrix. The h parameters for the phase scintillation in Scenario 1 (b)(c) are close to the typical values of a low-quality temperature compensated crystal oscillator (TCXO) listed in [Curran *et al.*, 2012]. For Scenario 2, the h parameter values are close to those of a moderate TCXO.

The second filter is the PIF, two choices of PLL bandwidths (2Hz and 10Hz) are implemented for the PIF in the evaluation. The 2Hz bandwidth reflects a high priority in filter performance consideration on the amplitude fading over the fast phase change, whereas 10Hz is a typical value used on LEO receivers and a moderate choice between the considerations for the fast phase change and for the amplitude fading.

Three different choices of integration time (1ms, 5ms, and 10ms) are implemented for the evaluations of both the PIF and the AKF approaches, resulting in 6 combinations of PIF-PLL parameters.

5.2.1. Tracking Results of Scenario 1 (b)(c)

Among the 10 realizations of data for each of Scenario 1(b) and (c), all 6 implementations of the conventional PIF-PLL lost lock of the signals. The AKF with 1ms and 5ms integration time showed successful tracking through the whole 300s of data for all 10 realizations of both Scenario 1 (b) and (c), whereas the one with 10ms lost lock for all realizations. Figure 5-6 plots the tracked C/N_0 and phase error results using AKF with 1ms and 5ms integration from one realization of Scenario 1 (b) and (c).

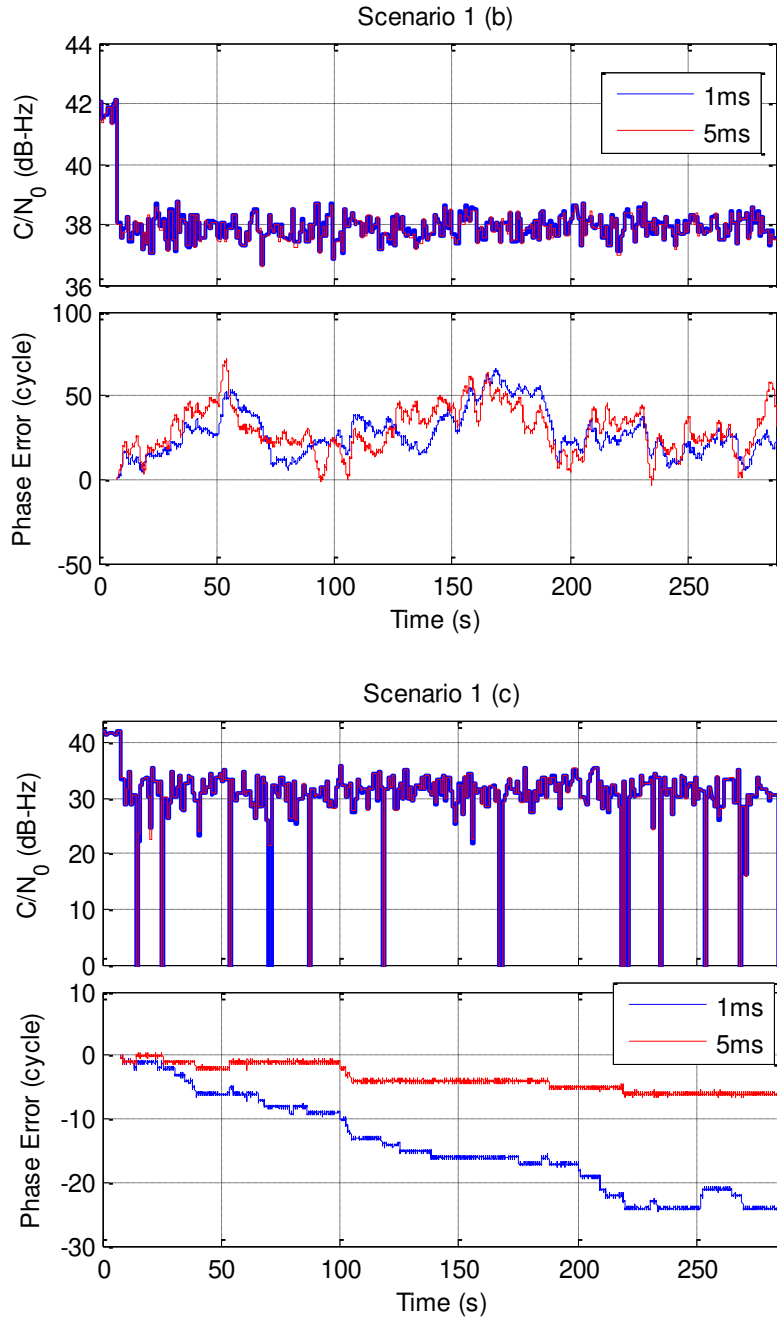


Figure 5-6. Tracked C/N_0 and phase error results using AKF with 1ms and 5ms integration time from one realization of Scenario 1 (b) and (c).

As can be seen in Figure 5-6, both AKF implementations showed very similar C/N_0 results of around 38 dB-Hz for Scenario 1 (b) due to its minor scintillation fading. It should be noted that the scintillation effects were added to the data after the first 8s, which is why the C/N_0 is at around

42dB-Hz at the beginning. Due to the fast variations of amplitude fading and the averaging effect in C/N_0 estimation method, the tracked C/N_0 seems rather flat. The tracked C/N_0 in Scenario 1 (c) are mostly around 30 dB-Hz with larger fluctuations from below 0 dB-Hz to 35dB-Hz due to its deeper amplitude fading. The phase error results in Scenario 1 (b) showed frequent occurrence of cycle slips for both implementations due to its violent phase changes as can be seen in Figure 5-5, whereas for Scenario 1 (c) with a much milder phase changes, AKF-5ms showed 10 occurrences of cycle slip and AKF-1ms showed about 2 times more. Table 5-2 provides the summary of total occurrences of cycle slip and RMSE in the carrier tracking of 10 realizations of data of Scenario 1 (b) and (c) using AKF-1ms and AKF-5ms. The RMSE results are obtained as the standard deviation of the phase error after the cycle slips are repaired.

Table 5-2. Summary of occurrences of cycle slip and RMSE for the tracking results using AKF-1ms and 5ms in all 10 realizations of data of Scenario 1 (b) and (c).

Scenario	1 (b)		1(c)	
	1	5	1	5
RMSE (cycle)	0.24	0.27	0.12	0.15
Cycle slip	8414	10158	454	130

As can be seen in Table 5-2, overall the tracking results in Scenario 1(b) showed a much worse carrier tracking performance than those in 1(c), with twice the RMSE and up to 2 orders of magnitude of occurrences of cycle slip, which suggests for the scintillation signal tracking of LEO under the geometry of Scenario 1, the violent phase scintillation is the dominant factor that requires a higher priority in the tracking loop design. For both Scenario 1(b) and (c), the AKF-1ms implementation showed a slightly better RMSE than that of AKF-5ms, indicating that the fast phase changes demand a faster update rate of the carrier tracking in order to better keep track, despite the signal power accumulation gain brought by the longer integration time. For Scenario 1

(c), the AKF-5ms showed a much less occurrences of cycle slip than the AKF-1ms, which is likely because the slower update rate of the carrier tracking will also decrease the chances of the carrier tracking loop making wrong adjustments during the frequent deep fades. Scenario 1(b) showed AKF-1ms has slightly fewer occurrences cycle slips than that of AKF-5ms implementation. However, with a cycle slip occurrence of around 10000 per 3000s of data for both implementations, the tracked carrier phase measurements quality is unreliable in analysis.

5.2.2. Tracking Results of Scenario 2

Among the 10 realizations of data for each of Scenario 2, all PIF implementations with a 2Hz bandwidth lost lock of the signals, whereas the ones with a 10Hz bandwidth maintained lock. This finding again collaborates the inference from the last subsection that the scintillation phase variations require a higher priority in carrier filter loop design. All AKF implementations showed successful tracking for all 10 realizations. Table 5-3 provides the summary of total occurrences of cycle slip and RMSE in the carrier tracking of 10 realizations of data of Scenario 2 using the 10Hz PIF implementations and AKF implementations with all three integration times.

Table 5-3. Summary of total occurrences of cycle slip and RMSE in the carrier tracking of 10 realizations of data of Scenario 2 using the 10Hz-PIF implementations and the AKF implementations with all three integration times

Algorithm	AKF			PIF		
	1	5	10	1	5	10
RMSE (cycle)	0.055	0.055	0.07	0.12	0.12	0.12
Cycle slip	81	60	55	490	304	300

As can be seen from Table 5-3, the AKF implementations overall showed a much better tracking performance than that of the PIF implementations in reducing the RMSE by half and the

occurrences of cycle slip by a factor of around 5. Between the implementations of different integration times, the finding is similar to the results in Scenario 1 (c) that a longer integration time will reduce the occurrences of cycle slips, while potentially cause a larger RMSE.

5.3. Concluding Remarks on LEO Scintillation Signal Simulation

This chapter presents simulation results of two scenarios of scintillation signal when received on the different antennas of LEO scintillation are obtained by manipulating different geometric parameters. The simulation results showed that for the POD antenna scenario with a nominal satellite elevation, when the receiver is travelling inside the ionosphere, the amplitude scintillation is negligible, but the scintillation induced phase changes are violent. As the phase screen gets higher, the resulting increase in propagation distance will raise the amplitude scintillation intensity with deeper fades, while the scintillation phase induced dynamics will be milder. However, the average S_4 index will saturate after the propagation distance reaches a certain value. The saturating value of the S_4 index is the same as the ground initialization data. As for the RO antenna scenario, since the propagation distance is much larger than the in the POD antenna scenario, the phase scintillation is mild comparing to the POD scenario with a strong amplitude scintillation of the same S_4 index as the initialization data.

6. CHAPTER 6 – RESULTS ON SCINTILLATION SIGNALS CHARACTERIZATION

In this section, characterization is performed on two kinds of signal processing results: the fast phase changes concurrent with signal amplitude fading and the GPS L1 navigation bit decoding error. For the fast phase changes characterization, SOL was used to process a subset of the four days of IF data collected in Ascension Island, 2013 March, in order to ensure carrier phase estimation accuracy with a high resolution. The data subset contains only strong scintillation events, which are by having σ_ϕ or S_4 index on GPS L1 signal exceeding 0.15 cycles or 0.75, respectively. Based on statistical analysis of the processing results, we established the probability distributions of concurrent deep signal fading and fast carrier phase changes and the duration of the fast phase changes on GPS triple-frequency signals. For the GPS L1 BDE, the processing results were obtained based on a larger subset of the same Ascension Island data using a conventional 3-order PLL (PIF-based), in order to assess the BDE typically experienced by commercial receivers in the field. Based on statistical analysis of the processing results, we established correlations between the BDE distributions and the amplitude scintillation and fading characteristics such as fading level and duration.

6.1. Scintillation Data Collection System

Both IF data subsets used in this study were collected during the same experimental campaign on Ascension Island in March 2013. Figure 6-1 depicts the reconfigurable multi-GNSS SDR data collection system used in this campaign, which contains five RF front ends each configured to collect signals within one frequency band: GPS L1/Galileo E1, GPS L2C, GPS L5/Galileo E5a, GLONASS L1, and BeiDou B1 signals [Peng and Morton, 2011]. All front-ends share the same wideband antenna input and are driven by the same low phase noise OCXO with zero IF and 4-bit

resolution. The front-ends collected data for five hours (20:00-01:00 UTC) on March 7 to 10, resulting in a total of 20 hours of IF data.

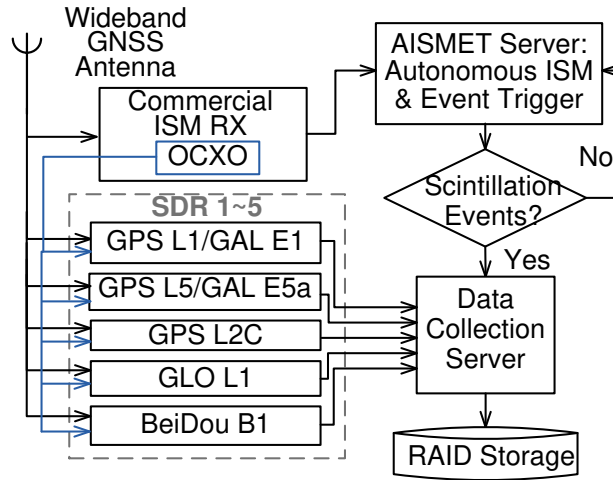


Figure 6-1. Schematic diagram of the wideband reconfigurable multi-GNSS data collection system setup at Ascension Island on March 7-10, 2013 [Xu and Morton, 2017].

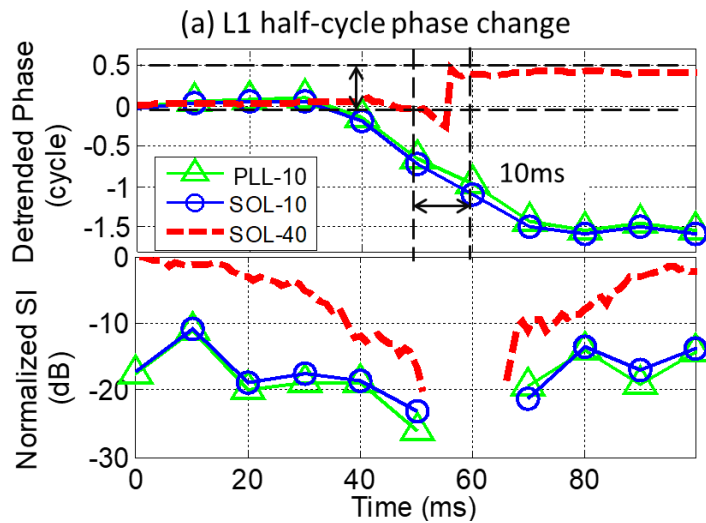
6.2. Characterization on Deep Fading and Fast Phase Changes

In this section, the SOL algorithm was first applied to real GPS L1 and L5 IF data collected on March 8th. Tracking result examples will be given that show fast phase changes of half and full cycles concurrent with deep fading on both frequencies. The data was also processed using a conventional 3rd-order PLL with a bandwidth of 2Hz as a comparison with that of SOL. The choice of the bandwidth 2Hz has been explained in section 4.6. The comparison confirmed the superior carrier phase estimation performance of the SOL over the conventional PLL algorithm in real data with strong equatorial scintillation. Then triple-frequency processing results are obtained using SOL based on a total of 174 minutes of strong scintillation events selected from the four days of IF data. Based on the detrended phase and $C/N_{0,SI}$ measurements during these events, statistical results are obtained to establish the probability distributions of concurrent deep signal fading and fast carrier phase changes and the duration of the fast phase changes.

6.2.1. Comparison of Real Data Tracking Results Using SOL and Conventional PLL

This section presents comparison between the performances of the SOL and conventional PLL algorithms with different integration times based on GPS L1 and L5 scintillation data collected on March 8th. The processing results show numerous fast phase changes of combinations of half and full cycles concurrent with deep fades on both frequencies during strong scintillation events. In Figure 6-2, three examples of deep fades concurrent with fast phase changes are plotted. The two examples in (a) and (b) are from the L1 signal on PRN 31 at UTC 23:18:13 and 23:15:05, respectively, while the one in (c) is from the L5 signal on PRN 24 at UTC 20:58:41. In these figures, results using three different tracking loop implementations are plotted:

- PLL-10: conventional PLL with 10-ms integration time;
- SOL-10: SOL with 10-ms integration time without the moving window integration;
- SOL-40: SOL with moving window integration of 40 ms with 1-msec time step.



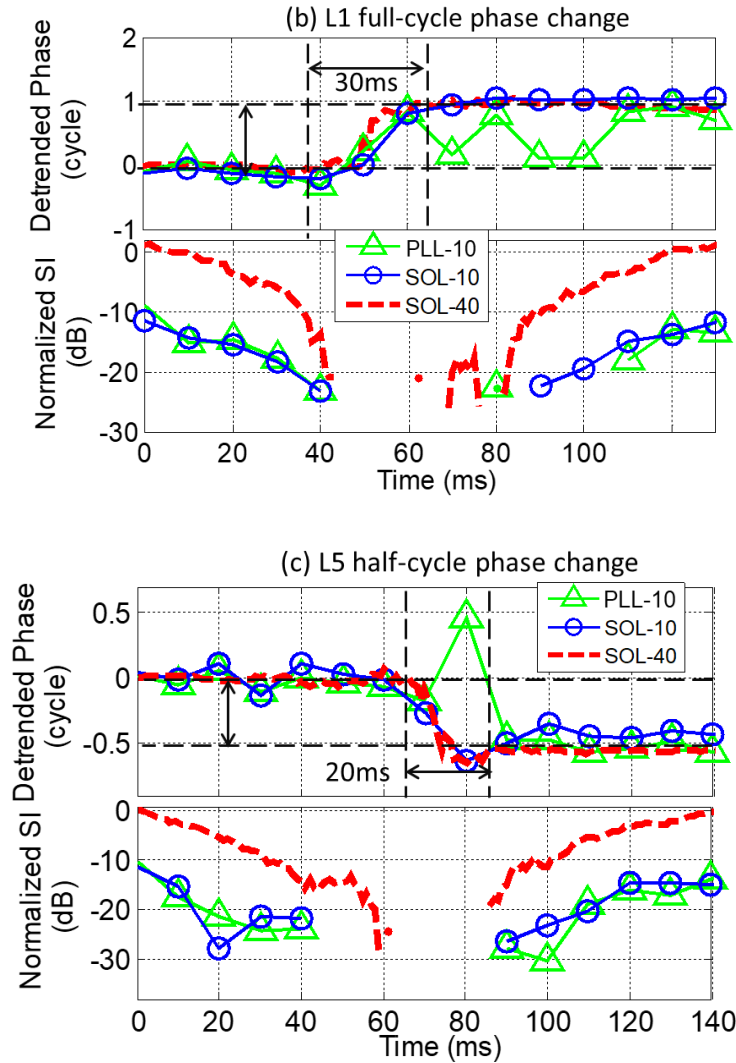


Figure 6-2. March 8th data tracking result examples using three tracking methods, showing deep fades associated with different kinds of fast phase changes. Results in (a) and (b) are from L1 signal on PRN 31, occurred at UTC 23:18:13 and 23:15:05, respectively, while (c) shows L5 results on PRN 24, occurred at UTC 20:58:41.

These three methods generated different phase estimations during deep fading. It should be noted that when calculating the normalized SI for SOL-40 using (4-18), its SI_{raw} is normalized over the SI_{trend} of SOL-10 in order to show the enhancement on signal intensity introduced by applying a longer integration time. In Figure 6-2 (a), the SOL-40 showed fast carrier phase jumps of half cycle within a 10-ms interval during a deep fade, whereas the SOL-10 and PLL-10 both

generated a half-cycle phase change with a full cycle slip over a 30-ms interval. All three implementations indicated deep fading in signal intensity that cannot be reliably estimated. For the deep fade in Figure 6-2 (b), both SOL-10 and SOL-40 showed a full-cycle phase change during a 30-ms interval, while the PLL-10 produced large phase oscillations that eventually settled down to a net full-cycle phase change 37 ms after the signal emerged from the deep fade. This is obviously caused by the PLL filter response to the large sudden phase change. As for the deep fade on L5 signal in Figure 6-2 (c), both SOL-10 and SOL-40 showed a half-cycle phase change that lasted around 20 ms, whereas the PLL-10 showed similar phase oscillations before settling down to a net half-cycle phase change but with a shorter duration than in Figure 6-2 (b).

It should be noted that, the noise-like large phase oscillations of the PLL-10 results in Figure 6-2 (b) and (c) occurred frequently (~60% probability whenever fast phase change occurred) throughout the processing results of the remaining Ascension Island data. This is due to its filter response to large, abrupt phase changes. Compared to SOL-40, the SOL-10 results produced 35% additional full-cycle changes during deep fades due to the insufficient signal energy accumulated with a shorter integration time during deep fading. This confirmed that the SOL with longer integration times and small steps is a better approach for the estimation of the carrier phase during deep fades.

6.2.2. Fast Phase Changes and Deep Fading Statistical Summary

Based on the detrended phase and $C/N_{0,SI}$ measurements during the 174-minute strong scintillation events, we obtained the number of fades and the number of fast phase changes. The fading duration is defined as the time interval during which $C/N_{0,SI}$ drops below a threshold value $C/N_{0,threshold}$. In this study, $C/N_{0,threshold}$ is set to 20 dB-Hz. The results are listed Table 6-1.

Half-cycle phase changes, full-cycle changes, and phase changes of a combination of full and half cycles are indicated in the table.

Table 6-1. Summary of number of fades and fast phase changes occurred in the Ascension Island data

Date	PRN		Nominal C/N_0 (dB-Hz)	Number of fades	Number of fast phase changes			Scintillation event length
					Half cycle	Full cycle	Half + Full cycle	
3/7	6	L1	38	252	16	2	1	22m 31s
	14	L1	44	78	19	2	0	21m 55s
3/8	24	L1	38	230	6	4	1	34m 10s
		L2	38	243	16	3	0	
		L5	44	102	22	4	0	
	31	L1	41	96	15	2	1	14m 03s
L2		41	129	24	2	0		
3/9	14	L1	43	98	25	2	0	13m 44s
	29	L1	45	64	9	2	1	23m 24s
		L2	45	95	12	0	2	
3/10	24	L1	38	104	0	3	0	17m 01s
		L2	38	124	4	1	0	
		L5	44	59	6	4	0	
	31	L1	42	99	24	4	0	27m 01s
		L2	42	146	31	1	0	
Total				1919	229	36	6	173m 49s

The following statistical results are derived from Table 6-1:

(1). *Number of deep fades.* The data contain a total of 1919 fades below the threshold values during the entire 174 minutes of scintillation on 5 satellite signals. This corresponding to approximately 11 deep fades per minute. Among them, 271 fades, or 14%, are accompanied by fast phase changes. For the same satellite, the L1 and L2 signals have the same nominal C/N_0 , whereas the nominal C/N_0 on L5 is 6 dB higher. This is mainly caused by the data collection hardware, as the GPS ICD

200H [US Air Force, 2013] and 705C [US Air Force, 2013] specified that the L1 transmitting power is 1 dB lower than the L5Q power and the L2C power is 1.5 dBs lower than the L1 power. There are considerably more deep fades on L2 than L1, which is consistent with earlier studies that signals at lower frequencies are usually more adversely affected by scintillation [Rino, 1979; Carrano et al., 2012b]. The number of L5 deep fades is less than 50% of that of L1 and L2 due to the 6 dB enhancement of its nominal C/N_0 .

(2). *Fast phase changes.* The number of fast phase changes is the highest on L5 and lowest on L1, which agrees with the conclusions of [Rino, 1979] and [Carrano et al., 2012b]. This observation, together with the fewer number of observed deep fades on L5 further confirms that the fast phase changes are indeed associated with the signal, instead of receiver signal processing artifacts. This is because the fading levels are a result of a combination of factors: real signal fades, hardware configuration, and satellite elevations, etc., whereas the large fast phase changes are unlikely associated with the hardware issues and satellite elevations in this study.

Of the 271 rapid phase changes observed, 229 are half-cycle, 36 are full-cycle, and 6 are full-plus-half-cycle. The duration distributions of half-cycle phase changes on signals of all three frequencies are plotted in Figure 6-3. The figure shows that for all three frequencies, the half-cycle phase changes occur in less than 100 ms. Over 80% of half-cycle phase changes occur during the 30~50 ms interval. The durations of the various types of phase changes larger than a half cycle are summarized in Table 6-2.

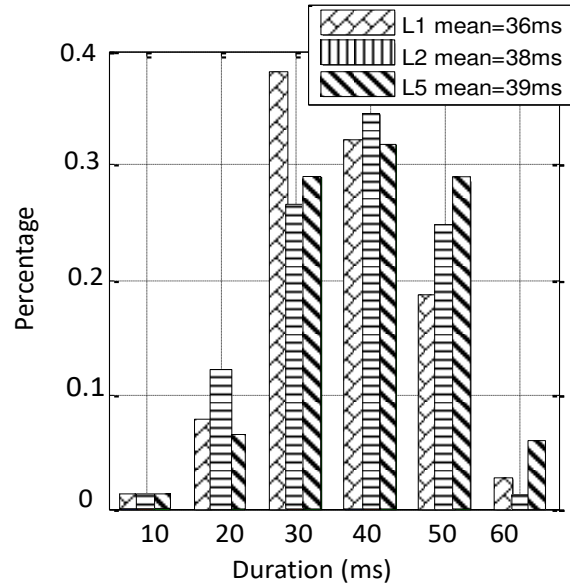


Figure 6-3. Comparison of duration distributions of half-cycle phase changes between signals across GPS bands.

Table 6-2 Duration of phase changes of full cycles and of combined full and half cycles

Duration (ms)	Number of Cycles	Number of Occurrence
30 - 45	1	31
55, 64, 65, 70, 90	1	1 each
25, 37, 41, 46, 50	1.5	1 each
88	2.5	1

(3) *Minimum C/N_0 value.* In order to further quantify the deep amplitude fades listed in Table 6-1 and establish a closer correlation between deep fading and concurrent phase changes, we compute the minimum C/N_0 based on $C/N_{0,SI}$ estimations for cases where the carrier phase estimations can be obtained using SOL. For the tracking results listed in Table 6-1, the percentages of fade occurrences with minimum C/N_0 levels at four different ranges are listed in Table 6-3. Also listed in Table 6-3 are the percentages of fast phase changes associated with these four levels of fades.

Table 6-3 Percentage of fades and concurrent fast phase changes within four different ranges of minimum C/N_0 values for the scintillation data listed in Table 6-1

Minimum C/N_0 (dB-Hz)	Percentage of fades	Percentage of concurrent phase changes
20 ~ 15	39.0%	0.4%
15 ~ 10	12.5%	2.2%
10~5	5.4%	0
<5	43.1%	97.4%

Table 6-3 shows that the fades have a rather polarized distribution in terms of fading levels. The majority of the signal either drop by a moderate amount to C/N_0 level of 20~15 dB-Hz (39.0%) or to an extremely deep fading level with C/N_0 below 5 dB-Hz (43.1%). Nearly all of the fast phase changes occurred during the latter case when extremely deep fade occurs. Below, the analysis of the relationship between deep fading durations and fast phase changes will focus on the fades in this category with a minimum C/N_0 below 5 dB-Hz.

(4) *Relationship between the deep fading durations and rapid phase change.* Figure 6-4 compares fading duration distributions for the deep fades that have and do not have concurrent phase changes. As can be seen in Figure 6-4, the rapid phase changes occurred mainly during extremely deep fades with durations less than 120 ms and mostly around 60 ms, whereas the duration distribution of the fades without concurrent phase changes ranges from 30 ms to 240 ms. Despite the limited amount of data used in the analysis, the results indicate that most fast phase changes accompany relatively steep fades.

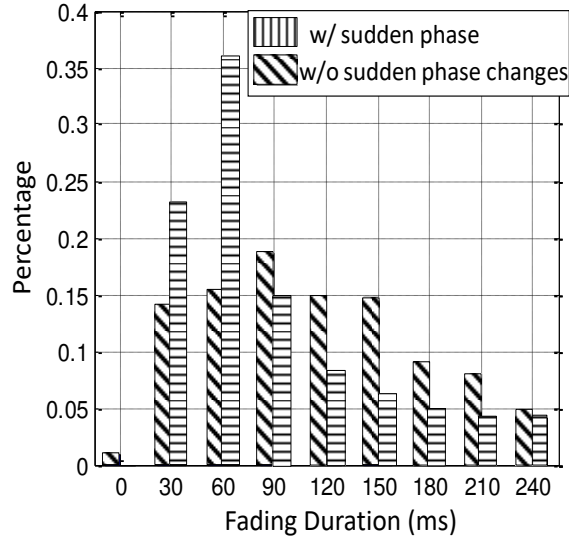


Figure 6-4. Comparison of fading duration distributions between extremely deep fades (minimum C/N_0 below 5 dB-Hz) with and without phase changes.

6.3. Characterization on GPS L1 BDE

This section presents the statistical analysis on GPS L1 BDE based on about 14 hours of GPS L1 processing results captured on six satellites during scintillation periods with the S_4 index over 0.5.

6.3.1. GPS L1 Bit Decoding Error Example

For GPS L1 signals, the navigation data bits are directly estimated based on the sign of I_p , whose representation has been given in equation (4-1).

When the tracking loop reaches steady-state under a nominal signal condition, the signal power should dominate over the noise power and dictate the sign of I_p in (4-1). In addition, the term $\text{sinc}(\pi\Delta fT) \cdot R(\Delta\tau)$ is positive. Therefore, the sign of I_p is determined by the sign of the product $D \cdot \cos(\Delta\phi)$.

The bit difference ΔD is the product of the decoded data bits and a truth reference. In this study, the product from the Bit Grabber Network (bitArc) of Constellation Observing System for Meteorology, Ionosphere, and Climate (COSMIC) [UCAR, 2013] is used as the data bit truth.

For conventional receivers, the carrier tracking loop implements the Costas discriminator when tracking signals with data modulation, which is insensitive to the data bit. As $\Delta\phi$ settles down to close to 0 or $\pm\pi$, ΔD can output either continuous “1” or “-1” for each data bit depending on the actual steady-state value of $\Delta\phi$. The navigation message decoding will not be affected regardless of the sign of the ΔD output because the GPS L1 navigation message encoding scheme is designed to overcome this ambiguity. This is enabled during bit encoding by making the polarity of the information bits (the first 24 bits) of a certain word dependent on the 30th bit of the last word: the polarity of the information bits of a certain word is reversed if the polarity of the 30th bit of the last word is “-1” [US Air Force, 2013]. This way, the reversion, which is introduced by $\cos(\Delta\phi)$ when $\Delta\phi$ settles at $\pm\pi$ and shared between words, can be removed during message decoding word-by-word. Therefore, the case when ΔD is continuously being “-1” should not be considered a decoding error. For more details, please refer to the GPS ICD [US Air Force, 2013].

However, during equatorial scintillation, large phase disturbances during signal amplitude fading will affect the bit decoding process by corrupting the relationship between I_p and D . As a result, ΔD may oscillate between “1” and “-1”, which will prevent correct decoding of the navigation message. After the signal recovered from a fade, ΔD may settle at a value that is reversed from the one before the fading (from “1” to “-1” or vice versa). Therefore, the number of bit errors is counted as the number of reversals of ΔD between “1” and “-1” during a fading event.

An example of such ΔD oscillations during a deep fade (PRN 6, starting time 22:29:16 UTC) using the PIF and AKF algorithms is given in Figure 6-5:

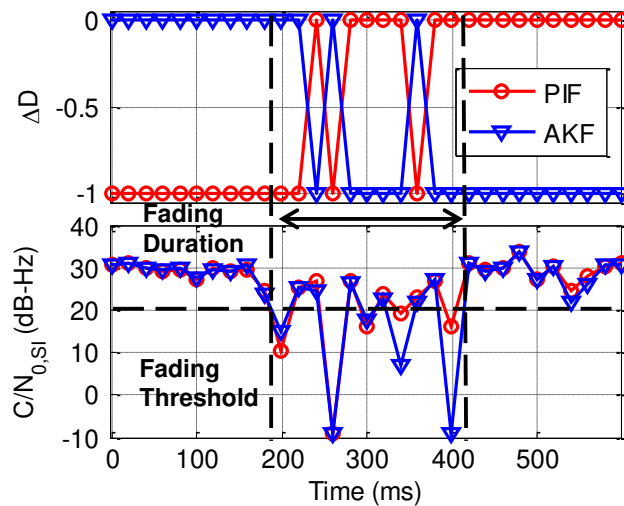


Figure 6-5. BDE example processed using PIF and AKF-based algorithms on GPS PRN 6 L1 signal at Ascension Island, starting at 22:29:16 UTC.

Figure 6-5 illustrates the fading duration and the associated data bit decoding error. The fading duration definition was given previously in section 6.2. During the fading duration, both algorithms produced oscillations on the ΔD results. Both ΔD results indicate 5 occurrences of bit reversions.

It should be mentioned that an alternative bit decoding approach is the differential bit decoding method described in [Van Dienrendonck, 1996] for a FLL. This approach detects the bit sign changes by examining the signs of the dot-products of the I and Q correlator outputs from two consecutive epochs. It is applicable to receivers utilizing FLL as it does not require the lock of carrier phase and is, therefore, suitable for applications on platforms undergoing high dynamics. However, the strong equatorial scintillation scenario discussed in this study is characterized with

both fast phase changes (which has an equivalent effect of high signal dynamics) and concurrent signal deep fading. Application of FLL to the data set indicated that it encountered difficulties maintaining lock to the signal and therefore prevented further assessment of the differential bit decoding performance.

6.3.2. BDE Processing Results and Statistical Analysis

This section presents the statistical correlations between the BDE occurrences and various amplitude scintillation indicators (average S_4 levels, fading occurrence frequency, fading depths and durations). Table 6-4 summarizes the durations, average S_4 indices, the number of fades and fading frequency of occurrences (per minute), the number of BDE occurrences (in bits) and its frequency of occurrence (per minute) for each scintillation event.

Table 6-4. Summary of the number of BDE and the amplitude scintillation parameters during the selected scintillation periods in the Ascension Island data

Date	PRN	Event Duration (hr)	Avg. S_4	# of Fades	# of Fades /min	# of BDE (bit)	# of BDE /min
3/7	6	0.94	0.59	177	3.13	436	7.73
	14	1.12	0.49	121	1.80	69	1.03
	22	1.09	0.41	23	0.35	22	0.34
	29	0.83	0.45	7	0.14	7	0.14
3/8	6	0.33	0.60	46	2.32	99	5.00
	14	0.22	0.57	8	0.61	15	1.14
	24	0.85	0.73	373	7.3	744	14.6
	29	0.98	0.65	228	3.88	494	8.40
	31	0.35	0.89	141	6.71	320	15.2
3/9	6	1.31	0.56	75	0.95	118	1.50
	29	0.41	0.78	85	3.46	162	6.59
	31	0.53	0.45	3	0.09	7	0.22
3/10	6	1.74	0.57	223	2.14	429	4.11

14	0.93	0.53	17	0.30	36	0.65
24	1.04	0.53	184	2.95	233	3.73
29	1.14	0.54	189	2.76	529	7.73
Sum	13.81		1900		3720	4.49

The following subsections present the statistical results derived from Table 6-4.

6.3.2.1. BDE Occurrence Frequency Dependence on Average S_4 value and Fading Occurrence Frequency

A total of 3720 bits of BDE occurred during 13.8 hours of the scintillation periods, resulting in an average frequency of occurrence of around 4.5 bits per minute. Figure 6-6 plots the number of fades per minute and average S_4 values listed in Table 6-4 and clearly showed nearly linear correlations between BDE frequency of occurrence with the average S_4 values and the average number of fades.

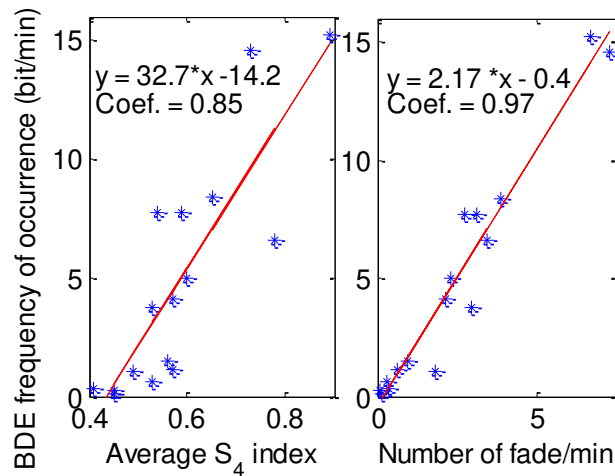


Figure 6-6. Relationships between the BDE frequency of occurrence and the average S_4 results (left panel) and the number of fades per minute (right panel) derived from the processing results of 14 hours of scintillation data.

6.3.2.2. Percentage of BDE occurrences with respect to S_4 levels

To examine the correlation between the occurrence of BDE and amplitude scintillation levels on a finer temporal scale, the S_4 estimations (obtained every second, as described after equation (1-1)) were categorized into 3 segments shown in Table 6-5. Also listed in Table 6-5 are the number and percentage of the S_4 samples for each segment and corresponding BDE occurred during each segment. The probability of BDE occurrence listed in the rightmost column is obtained by dividing the number of S_4 samples that experience BDE by the total number of S_4 samples within the segment. Table 6-5 indicates that during the selected scintillation durations the probability of BDE occurrence increases as the amplitude scintillation intensity increases.

Table 6-5. Number and percentage of the S_4 estimate samples and of the BDE, and the probability of BDE occurrence under different S_4 levels

S_4 level	# of S_4 samples / percentage	# of BDE / percentage	Probability of occur.
<0.7	36700 / 74%	667 / 18%	0.01
0.7~0.9	7985 / 16%	1326 / 36%	0.05
>0.9	4887 / 10%	1727 / 46%	0.12

6.3.2.3. Percentage of BDE occurrences w.r.t fading levels

The fading depth is determined by the minimum $C/N_{0,SI}$ value during the fading duration. Table 6-6 summarized the number and corresponding percentage of the fades under different fading depth ranges and those of the BDE concurrent with these fades. The probability of BDE occurrence listed in the rightmost column is obtained by dividing the number of fades that are associated with BDE occurrences by the total number of fades within each fading depth range. Table 6-6 shows

that the majority of BDE occurred during fades with extremely deep fading of below 5 dB-Hz with a probability of occurrence up to 0.81, while these extremely deep fades comprise 45% of the total number of fades.

Table 6-6. Number and percentage of the fades and of the BDE, and the probability of occurrence under different fading levels

Minimum $C/N_{0,SI}$ (dB-Hz)	# of fades / percentage	# of BDE / percentage	Probability of occur.
15~20	224 / 12%	31 / 0.8%	0.06
10~15	163 / 9%	10 / 0.3%	0.03
5~10	644 / 34%	266 / 7%	0.15
<5	869 / 45%	3413 / 91.9%	0.81

6.3.2.4. Correlation between BDE occurrence and extremely deep fade duration

Based on the number of BDE occurred during each extremely deep fade ($C/N_{0,SI} < 5$ dB-Hz), these fades are divided into 5 groups with the corresponding percentages plotted in Figure 6-7. It shows that the larger number of BDE within a fade is much less likely compared to the smaller number of BDE within a fade. More than 70% of the cases involve less than 5 BDE occurrences within one fade. The mean number of BDE occurred during one fade is 4.9 bits for these extremely deep fades.

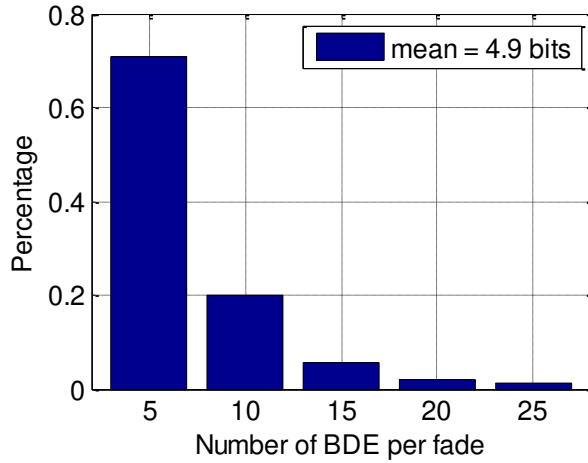


Figure 6-7. Distribution of the extremely deep fades ($C/N_{0,SI} < 5\text{B-Hz}$) w.r.t. the number of BDE occurred during each of them.

The correlation between the number of BDE occurred during a certain fade and the duration of the corresponding fade is plotted in Figure 6-8. The data shows that the number of BDE during one fade grows almost linearly with the duration of the concurrent fade, with a ratio of 8.5 (bit per second) and a correlation coefficient of 0.7.

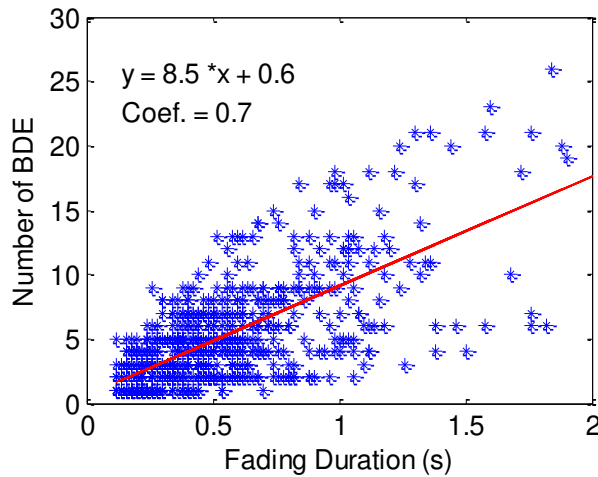


Figure 6-8. Relationship between the number of BDE occurred during an extremely deep fade and the corresponding fading duration

6.4. Concluding Remarks on Scintillation Signal Characterization

In this section, statistical analysis is first performed to characterize the fast phase changes concurrent with signal amplitude fading based on the processing results of the 174-minute strong scintillation data (S_4 and σ_ϕ on L1 signals exceeded 0.15 cycles and 0.75, respectively). The results showed that the average frequency of deep fades (< 20 dB-Hz) is around 11 per minute and 14 % of these deep fades are associated with fast phase changes. While L1 and L2 signals have the same nominal C/N_0 , the L2 signal has more fades than L1. The L5 signal has the fewest fades among the three bands, most likely due to its 6 dB higher nominal C/N_0 over L1 and L2. Most of the phase changes are half-cycle variations. L5 has the largest number of fast phase changes, while L1 has the smallest number. Half-cycle phase changes on triple-frequency signals mostly occur over 30~50 ms interval. And finally, the overwhelming majority of the phase changes occur during extremely deep fades with C/N_0 below 5 dB-Hz. The average duration of these fades is ~60 ms.

In addition, the statistical relationship between the GPS L1 navigation BDE occurrences and the intensity of amplitude scintillation were obtained based on processing results of 14-hour scintillation data ($S_4 > 0.5$). A total of 3720 bits of BDE were identified, indicating an overall rate of occurrence of 4.5 bits per minute. The results also indicated that the number of BDE occurrence is linearly related to the average S_4 index and the number of fades per minute. Up to 92% of the BDE occurred during extremely fades with minimum $C/N_{0,SI}$ below 5 dB-Hz. Among these extremely deep fades, most contains around 5 bits of BDE, while the maximum number of BDE during one fade can exceed 25 bits.

7. CHAPTER 7 – CONCLUSION

This dissertation presented equatorial ionospheric scintillation simulation, processing, and characterization on GPS signals, using real and simulated GPS scintillation data. The work conducted in this dissertation includes three parts of contributions.

A two-parameter, physics-based, strong scintillation simulator is presented and validated with real scintillation data. Numerical mappings from the user input parameter set to the phase screen model parameter subset is obtained through numerical evaluation. Based on these numerical mappings, the scintillation model can be controlled by specifying the expected S_4 and τ_0 values from scintillation measurements obtained from a stationary ground-based receiver. The simulator can generate statistically equivalent realizations of the scintillation effects. Using this basic two-parameter set, the simulator can also generate realistic scintillation effects that are observed on platforms with user-defined dynamics under the same ionospheric phase screen responsible for producing the ground received scintillation.

A SOL algorithm has been developed to improve the carrier phase estimation during deep fading. For a stationary platform, the prior surveyed receiver position is used instead of the receiver-generated position, and the time solution is the only feedback to the carrier tracking loop for signal parameter prediction. In addition, the SOL approach benefits the carrier phase estimation, as its open-loop architecture allows correlation to be performed over a moving window spanning a relatively long integration period with small time increments. This moving window procedure reduces noise contribution while preserving the fine temporal structures of carrier phase estimates

during a deep fade. For a dynamic platform, the PVT solutions are first obtained from a VDFLL using healthy satellites to update the scintillation satellite parameters. The moving window procedure can then be applied in the same manner as for the stationary platform.

Making use of the scintillation signal simulator developed, the SOL algorithm was evaluated and compared with two other advanced carrier tracking algorithms in terms of cycle slip occurrences and phase RMSE. The evaluation results confirmed the advantage of such a semi-open architecture for accurate scintillation phase estimation.

Finally, the scintillation signal characterization conducted is based on the processing results of real scintillation data collected from Ascension Island, including 1) the temporal characteristics of fast phase changes and deep fades, and their correlation during concurrence; 2) the statistical relationship between the GPS L1 navigation BDE occurrences and the scintillation S_4 values and fading characteristics.

REFERENCES

- Arras, C., J. Wickert, G. Beyerle, S. Heise, T. Schmidt, and C. Jacobi (2008), A global climatology of ionospheric irregularities derived from GPS radio occultation, *Geophysical Research Letters*, 35(14), doi: 10.1029/2008GL034158.
- Aarons, J. (1982), Global morphology of ionospheric scintillation, *Proc. IEEE*, 70(4), 360-378, doi: 10.1109/PROC.1982.12314.
- Aarons, J., and S. Basu (1994), Ionospheric amplitude and phase fluctuations at the GPS frequencies, Proc. ION GPS, 1569 – 1578, Salt Lake City, UT.
- Akala, A. O., L. L. N. Amaeshi, E. O. Somoye, R. O. Idolor, E. Okoro, P. H. Doherty, K. M. Groves, C. S. Carrano, C. T. Bridgwood, P. Baki, F. M. D’ujanga, and G. K. Seemala (2015), Climatology of GPS amplitude scintillations over equatorial Africa during the minimum and ascending phases of solar cycle 24, *Astrophysics and Space Science*, 357(17), doi: 10.1007/s10509-015-2292-9.
- Aquino, M., T. Moore, A. Dodson, S. Waugh, J. Souter, and F. S. Rodrigues (2005), Implications of ionospheric scintillation for GNSS users in northern Europe, *The Journal of Navigation*, 58(2), 241–256, doi: 10.1017/S0373463305003218.
- Breitsch, B., D. Xu, Y. Morton, and C. Rino (2019), GNSS carrier phase transitions due to ionospheric diffraction: simulation and characterization, submitted to *IEEE Transactions on Aerospace and Electronic Systems*.
- Basu, S., K. M. Grove, S. Basu, and P. J. Sultana (2002), Specification and forecasting of scintillations in communication and navigation links: current status and future plans, *Journal of Atmospheric and Solar-Terrestrial Physics*, 64(16), 1745-1754, doi: 10.1016/S1364-6826(02)00124-4.
- Bar-Shalom, Y., X. R. Li, and T. Kirubarajan (2004), Estimation for kinematic models, Chapter 6 in *Estimation with applications to tracking and navigation: theory algorithms and software*, 267-299, John Wiley and Sons Ltd, Hoboken, NJ.
- Brown, R. G., and P. Hwang (1996), *Introduction to random signals and applied Kalman filtering*, John Wiley & Sons Ltd, Hoboken, NJ.
- Buchert, S., F. Zangerl, M. Sust, M. André, A. Eriksson, J. Wahlund, and H. Opgenoorth (2015), SWARM observations of equatorial electron densities and topside GPS track losses, *Geophysical Research Letters*, 42(7), 2088-2092, doi: 10.1002/2015GL063121.

Carrano, C. S., C. E. Valladares, and K. M. Groves (2012a), Latitudinal and local time variation of ionospheric turbulence parameters during the conjugate point equatorial experiment in Brazil, *International Journal of Geophysics*, Art. No. 103963, doi:10.1155/2012/103963.

Carrano, C. S., K. M. Groves, W. J. McNeil, and P. H. Doherty (2012b), Scintillation characteristics across the GPS frequency band, Proc. ION GNSS, 1972-1989, Nashville, TN.

Carrano, C. S., and C. L. Rino (2016), A theory of scintillation for two-component power law irregularity spectra: I. Overview and numerical results, *Radio Science*, 51(6), 789-813, doi: 10.1002/2015RS005903.

Carrano, C. S., and C. L. Rino (2019), Irregularity parameter estimation for interpretation of scintillation Doppler and intensity spectra, Proc. USNC-URSI NRSM, Boulder, CO. <http://www.ursi.org/proceedings/MC-USA/USNC-NRSM2019/papers/G4-4.pdf>

Carroll, M., and Y. Morton (2014), Triple frequency GPS signal tracking during strong ionospheric scintillations over Ascension Island, Proc. IEEE/ION PLANS, 43-49, Monterey, CA.

Cervera, M. A., and M. F. Knight (1998), Time series modelling of intensity and phase scintillation at GPS frequencies, *Acta Geodaetica et Geophysica Hungarica*, 33(1), 25-40, doi: 10.1007/BF03325520.

Chartier, A., B. Forte, K. Deshpande, G. Bust, and C. Mitchell (2016), Three-dimensional modeling of high-latitude scintillation observations, *Radio Science*, 51(7), 1022–1029, doi: 10.1002/2015RS005889.

Chiou, T. Y., J. Seo, T. Walter, and P. Enge (2008), Performance of a Doppler-aided GPS navigation system for aviation applications under ionospheric scintillation, Proc. ION GNSS, 1139-1147, Savannah, GA.

Christiansen, G. S (1994), Modeling of a PRML timing loop as a Kalman filter, *Proc. IEEE GLOBECOM*, Vol. 2, doi: 10.1109/GLOCOM.1994.512839.

Conker, R. S., M. B. El-Arini, C. Hegarty, and T. Hsiao (2003), Modelling the effects of ionospheric scintillation on GPS/SBAS availability, *Radio Science*, 38(1), 1-23, doi: 10.1029/2000RS002604.

Curran, J. T., G. Lachapelle, and C. C. Murphy (2012), Digital GNSS PLL Design Conditioned on Thermal and Oscillator Phase Noise, *IEEE Transactions on Aerospace and Electronic Systems*, 48(1), 180-196, doi: 10.1109/TAES.2012.6129629.

Curran, J. T., M. Bavaro, J. Fortuny-Guasch, and A. Morrison (2014), Developing an ionospheric scintillation monitoring receiver, *Inside GNSS*, 9(5), 60-72.

Deshpande, K. B., G. S. Bust, C. R. Clauer, W. A. Scales, N. A. Frissell, et al. (2016), Satellite-beacon Ionospheric-scintillation Global Model of the upper Atmosphere (SIGMA) II: Inverse modeling with high-latitude observations to deduce irregularity physics, *Journal of Geophysical Research: Space Physics*, 121(9), 9188-9203, doi: 10.1002/2016JA022943.

Driessen, P. F. (1994), DPLL bit synchronizer with rapid acquisition using adaptive Kalman filtering techniques, *IEEE Transactions on Communications*, 42(9), 2673–2675, doi: 10.1109/26.317406.

Fremouw, E. J., R. C. Livingston, and D. A. Miller (1980), On the statistics of scintillating signals, *Journal of Atmospheric and Terrestrial Physics*, Vol. 42, 717-731, doi: 10.1016/0021-9169(80)90055-0.

Ghafoori, F., and S. Skone (2015), Impact of equatorial ionospheric irregularities on GNSS receivers using real and synthetic scintillation signals, *Radio Science*, 50(4), 294–317, doi: 10.1002/2014RS005513.

Groves, P. D. (2008a), Satellite navigation processing, errors, and geometry, Chapter 7 in *Principles of GNSS, Inertial, and Multisensor Integrated Navigation Systems*, 225-226, Artech House, Boston/London.

Gleason, S., V. Zavorotny, and S. Lowe (2009), Remote sensing using bistatic GNSS reflections, Chapter 16 in *GNSS Applications and Methods*, 399-436, Artech House, Boston/London.

Hegarty, C., M. B. El-Arini, T. Kim, and S. Ericson (2001), Scintillation modeling for GPS-wide area augmentation system receivers, *Radio Science*, 36(5), 1221-1231, doi: 10.1029/1999RS002425

Henkel, P., K. Giger, and C. Gunther (2009), Multifrequency, multisatellite vector phase-locked loop for robust carrier tracking, *Journal of Selected Topics in Signal Processing, IEEE*, 3(4), 674-681, doi: 10.1109/JSTSP.2009.2025637.

Humphreys, T. E., M. L. Psiaki, J. C. Hinks, and P. M. Kintner (2009), Simulating ionosphere-induced scintillation for testing GPS receiver phase tracking loops, *Journal of selected topics in signal processing, IEEE*, 3(4), 707–715, doi: 10.1109/JSTSP.2009.2024130.

Humphreys, T. E., M. L. Psiaki, B. M. Ledvina, A. P. Cerruti, and P. M. Kintner (2010), Data-driven testbed for evaluating GPS carrier tracking loops in ionospheric scintillation, *IEEE Transactions on Aerospace and Electronic Systems*, 46(4), 1609-1623, doi: 10.1109/TAES.2010.5595582.

Jacobsen, K. S., and S. Schäfer (2012), Observed effects of a geomagnetic storm on an RTK positioning network at high latitudes, *Journal of Space Weather and Space Climate*, Vol. 2, A13, doi: 10.1051/swsc/2012013.

- Jiao, Y., Y. T. Morton, S. Taylor, and W. Pelgrum (2013), Characterization of high latitude ionospheric scintillation of GPS signals, *Radio Science*, 48(6), 698-708, doi: 10.1002/2013RS005259.
- Jiao, Y., and Y. Morton (2015), Comparison of the effect of high-latitude and equatorial ionospheric scintillation on GPS signals during the maximum of solar cycle 24, *Radio Science*, 50(9), 886–903, doi: 10.1002/2015RS005719.
- Jiao, Y., D. Xu, Y. Morton, and C. L. Rino (2016), Equatorial scintillation amplitude fading characteristics across the GPS frequency bands, *Navigation*, 63(3), 267-281, doi: 10.1002/navi.146.
- Jiao, Y., C. L. Rino, and Y. T. Morton (2018), Ionospheric Scintillation Simulation on Equatorial GPS Signals for Dynamic Platforms, *Navigation*, 65(2), 263-274, doi: 10.1002/navi.231.
- Jwo, D. J. (2001), Optimisation and sensitivity analysis of GPS receiver tracking loops in dynamic environments, *IEE Proceedings-Radar, Sonar and Navigation*, 148(4), 241-250, doi: 10.1049/ip-rsn:20010429.
- Kaplan, E., and C. Hegarty (2005), *Understanding GPS: Principles and Applications*, Artech house, Boston, USA/London, UK.
- Kassabian, N., and Y. Morton (2013), Galileo tracking performance under ionosphere scintillation, Proc. International Colloquium Scientific and Fundamental Aspects of the Galileo Programme, Prague, Czech Republic.
- Kay, S. M. (1993), *Fundamentals of Statistical Signal Processing: Estimation Theory*, Prentice-Hall, Englewood Cliffs, NJ.
- Kintner, P. M., B. M. Ledvina, E. R. de Paula, and I. J. Kantor (2004), Size, shape, orientation, speed, and duration of GPS equatorial anomaly scintillations, *Radio Science*, 39(2), 1-23, doi: 10.1029/2003RS002878.
- Kintner, P. M., B. M. Ledvina, and E. R. de Paula (2007), GPS and ionospheric scintillations, *Space Weather*, 5(9), doi: 10.1029/2006SW000260.
- Kuusniemi, H. (2005), User-level reliability and quality monitoring in satellite-based personal navigation, PhD Thesis, Tampere University of Technology, Finland.
- Kuusniemi, H. and T. Jokitalo (2009), Indoor and Weak Signal Navigation, Chapter 12 in *GNSS applications and methods*, Artech House, Boston, London.

- Lashley, M., D. M. Bevly, and J. Y. Hung (2009), Performance analysis of vector tracking algorithms for weak GPS signals in high dynamics, *Journal of Selected Topics in Signal Processing, IEEE*, 3(4), 661-673, doi: 10.1109/JSTSP.2009.2023341.
- Lee, J., Y. Morton, J. Lee, H.-S. Moon, and J. Seo (2017), Monitoring and mitigation of ionospheric anomalies for GNSS-based safety critical systems: A review of up-to-date signal processing techniques, Special Issue on Advances in Signal Processing for Global Navigation Satellite Systems, *IEEE Signal Processing Magazine*, 34(5), 96-110, doi: 10.1109/MSP.2017.2716406.
- Li, X., M. Ge, X. Dai, X. Ren, M. Fritsche, J. Wickert, and H. Schuh (2015a), Accuracy and reliability of multi-GNSS real-time precise positioning: GPS, GLONASS, BeiDou, and Galileo, *Journal of Geodesy*, 2015, 89(6), 607-635, doi: 10.1007/s00190-015-0802-8.
- Li, X., X. Zhang, X. Ren, M. Fritsche, J. Wickert, and H. Schuh (2015b), Precise positioning with current multi-constellation global navigation satellite systems: GPS, GLONASS, Galileo and BeiDou, *Scientific reports* 5, 2015, Art. No. 8328, doi: 10.1038/srep08328.
- Liu, Y., Y. J. Morton, and Y. Jiao (2018), Application of machine learning to the characterization of GPS L1 ionospheric amplitude scintillation, Proc. IEEE/ION PLANS, 1159-1166, Monterey, CA.
- Mao, X., and Y. Morton (2013), GNSS receiver carrier tracking loop designs for robust navigation application and for ionosphere studies, Proc. ION GNSS+, 3248–3254, Nashville, TN.
- Misra, P., and P. Enge (2011), *Global Positioning System: Signals, Measurements, and Performance, Revised 2nd Version*, Ganga-Jamuna Press, Lincoln, MA.
- Morton, R. (2014), Investigation of the impact of solar storms on the Global Positioning System receivers at high latitudes, Proc. ION ITM, 700 – 708, San Diego, CA.
- Morton, Y., Y. Jiao, and S. Taylor (2015a), High-latitude and equatorial ionospheric scintillation based on an event-driven multi-GNSS data collection system, Proc. Ionospheric Effects Symposium, Alexandria, VA.
- Morton, Y., Y. Jiao, F. van Graas, E. Vinande, and N. Pujara (2015b), Analysis of receiver multi-frequency response to ionospheric scintillation in Ascension Island, Hong Kong, and Singapore, Proc. ION PNT, 10-16, Honolulu, HI.
- Myer, G., and Y. Morton (2018), Ionosphere scintillation effects on GPS measurements, a new carrier-smoothing technique, and positioning algorithms to improve accuracy, Proc. ION ITM, 420-439, Reston, VA.

- Nakagami, M. (1960), Statistical methods, in *Radio Wave Propagation*, 3-36, Pergamon, Elmsford, New York.
- Niu, F. (2012), Performance of GPS Signal Observables Detrending Methods for Ionosphere Scintillation Studies, M.S. thesis, Department of Electrical and Computer Engineering, Miami University, Oxford, OH.
- O'Driscoll, C., and G. Lachapelle (2009), Comparison of traditional and Kalman filter based tracking architectures, Proc. European navigation conference, Naples, Italy.
- Oliveira, K., A. Moraes, E. Costa, M. Muella, E. R. de Paula, and W. Perrella (2014), Validation of the alpha-mu model of the power spectral density of GPS ionospheric amplitude scintillation, *International Journal of Antennas and Propagation*, A573615, doi: 10.1155/2014/573615.
- Pelgrum, W., Y. Morton, F. van Graas, P. Vikram, and S. Peng (2011), Multi-domain analysis of the impact on natural and man-made ionosphere scintillations on GNSS signal propagation, Proc. ION GNSS, 617-625, Portland, OR.
- Peng, S., and Y. Morton (2011), A USRP2-based multi-constellation and multi-frequency GNSS software receiver for ionosphere scintillation studies, Proc. ION ITM, 1033-1042, San Diego, CA.
- Peng, S., Y. Morton, and R. Di (2012), A multiple-frequency GPS software receiver design based on a vector tracking loop, Proc. IEEE PLANS, 495-505, Myrtle Beach, SC.
- Peral-Rosado, D., J. A. Lopez-Salcedo, G. Seco-Granados, et al. (2010), Kalman filter-based architecture for robust and high-sensitivity tracking in GNSS receivers, *Proc. Satellite Navigation Technologies and European Workshop on GNSS Signals and Signal Processing (NAVITEC)*, IEEE, Noordwijk, Netherlands, doi: 10.1109/NAVITEC.2010.5708005.
- Psiaki, M., T. Humphreys, A. Cerruti, S. Powell, and P. Kintner (2007), Tracking L1 C/A and L2C signals through ionospheric scintillations, Proc. ION GNSS, 246-268, Fort Worth, TX.
- Razavi, A., D. Gebre-Egziabher, and D. M. Akos (2008), Carrier loop architectures for tracking weak GPS signals, *IEEE Transactions on Aerospace and Electronic Systems*, 44(2), 697-710, doi: 10.1109/TAES.2008.4560215.
- Remodi, B. M. (2004), GPS Tool Box: Computing satellite velocities using the broadcast ephemeris, *GPS Solutions*, 8(3), 181-183, doi: 10.1007/s10291-004-0094-6.
- Rino, C. L. (1979), A power law phase screen model for ionospheric scintillation: 1. weak scatter, *Radio Science*, 14(6), 1135-1145, doi: 10.1029/RS014i006p01135.

Rino, C. L. (1980), Transionospheric radiowave propagation and signal statistics, Agard. Conf. Proc. No. 284, Propagation Effects in Space/Earth Paths, London, UK.

Rino, C. L. (2011), *The theory of scintillation with applications in remote sensing*, John Wiley & Sons, Inc., Hoboken, NJ.

Rino C. L., and C. S. Carrano (2013), A compact strong-scatter scintillation model, Proc. The International Beacon Satellite Symposium, Bath, U.K. [online] Available at: <https://pdfs.semanticscholar.org/1af6/97b5e4b96355174fbd1cce524ebb68f5651c.pdf>

Rino, C. L., C. S. Carrano, and P. Roddy (2014), Wavelet-based analysis and power law classification of C/NOFS high-resolution electron density data, *Radio Science*, 49(8), 680–688, doi: 10.1002/2013RS005272.

Rino, C. L., B. Breitsch, Y. Morton, Y. Jiao, D. Xu, and C. Carrano (2018), A compact multi-frequency GNSS scintillation model, *Navigation*, 65(4), 563-569, doi: 10.1002/navi.263.

Seo, J., T. Walter, T. Y. Chiou, and P. Enge (2009), Characteristics of deep GPS signal fading due to ionospheric scintillation for aviation receiver design, *Radio Science*, 44(1), doi: 10.1029/2008RS004077.

Seo, J., T. Walter, and P. Enge (2011a), Availability impact on GPS aviation due to strong ionospheric scintillation, *IEEE Transactions on Aerospace and Electronic Systems*, 47(3), 1963-1973, doi: 10.1109/TAES.2011.5937276.

Seo, J., T. Walter, and P. Enge (2011b), Correlation of GPS signal fades due to ionospheric scintillation for aviation applications, *Advances in Space Research*, 47(10), 1777-1788, doi: 10.1016/j.asr.2010.07.014.

Shanmugam, A., and R. MacLeod (2013), GNSS ionospheric scintillation and TEC monitoring using GPStation-6, *Proc. IEEE International Conference on Space Science and Communication (IconSpace)*, 207-212, Melaka, Malaysia, doi: 10.1109/IconSpace.2013.6599466.

Spilker, J. J. (1995), Vector Delay Lock Loop Processing of Radiolocation Transmitter Signals, U.S. Patent 5398034.

Spilker, J. J. (1996). Fundamentals of signal tracking theory, Chapter 4 in *Global Positioning System: Theory and Applications, Volume 1*, American Institute of Aeronautics and Astronautics, Washington, DC.

Skone, S., K. Knudsen, and M. de Jong (2001), Limitations in GPS receiver tracking performance under ionospheric scintillation conditions, *Physics and Chemistry of the Earth, Part A: Solid Earth and Geodesy*, 26(6-8), 613-621, doi: 10.1016/S1464-1895(01)00110-7.

Steigenberger, P., O. Montenbruck, and U. Hessel (2015), Performance evaluation of the early CNAV navigation message, *Navigation*, 62(3), 219-228, doi: 10.1002/navi.130.

Susi, M., M. Aquino, R. Romero, F. Dosis, and M. Andreotti (2014), Design of a robust receiver architecture for scintillation monitoring, Proc. IEEE PLANS, 73–81, Monterey, CA.

Sust, M., F. Zangerl, O. Montenbruck, S. Buchert, and A. Garcia-Rodriguez (2014), Spaceborne GNSS-receiving system performance prediction and validation, *Proc. Satellite Navigation Technologies and European Workshop on GNSS Signals and Signal Processing (NAVITEC)*, IEEE, Noordwijk, Netherlands.

Takahashi, H., C. M. Wrasse, C. M. Denardini, M. B. Pádua, E. R. Paula, S. M. A. Costa, Y. Otsuka, et al. (2016), Ionospheric TEC weather map over South America, *Space Weather*, 14(11), 937-949, doi: 10.1002/2016SW001474.

Taylor, S., Y. Morton, Y. Jiao, J. Triplett, and W. Pelgrum (2012), An improved ionosphere scintillation event detection and automatic trigger for a GNSS data collection system, Proc. ION ITM, 1563–1569, Newport Beach, CA.

Tran, M. and C. Hegarty (2002), Receiver Algorithms for the New Civil GPS Signals, Proc. ION NTM, 778-789, San Diego, CA.

Tran, M. (2004), Performance evaluations of the new GPS L5 and L2 Civil (L2C) signals, *Navigation*, 51(3), 199-212, doi: 10.1002/j.2161-4296.2004.tb00351.x.

Tsui, J. (2005), *Fundamentals of Global Positioning System Receivers: A Software Approach*, 2nd edition, John Wiley & Sons, Inc., Hoboken, NJ.

UCAR (2013), GPS data bits hourly archive files, <http://cosmic-io.cosmic.ucar.edu/cdaac/login/fidrt/level1a/bitArc/>

US Air Force (2012), Interface specification IS-GPS-705C, NAVSTAR GPS Space Segment/navigation User Interfaces.

US Air Force (2013), Interface specification IS-GPS-200H, NAVSTAR GPS Space Segment/Navigation User Interfaces.

Van Dierendonck, A. J., J. A. Klobuchar, and Q. Hua (1993), Ionospheric scintillation monitoring using commercial single frequency C/A code receivers, Proc. ION ITM, 1333-1342, Salt Lake City, UT.

Van Dierendonck, A. J. (1996), GPS receivers, Chapter 8 in *Global Positioning System: Theory and Applications, Volume 1*, American Institute of Aeronautics and Astronautics, Washington, DC.

Van Dierendonck, A. J. (2005), How GPS receivers measure (or should measure) ionospheric scintillation and TEC and how GPS receivers are affected by the ionosphere, Proc. Ionosphere Effects Symposium, Alexandria, VA.

Van Diggelen, F. (2009), *A-GPS: assisted GPS, GNSS, and SBAS*, Artech House Publishers, Boston, US/London, UK.

Vilà-Valls, J., P. Closas, and C. Fernández-Prades (2015), Advanced KF-based methods for GNSS carrier tracking and ionospheric scintillation mitigation, *Proc. IEEE Aerospace Conference*, Big Sky, MT, doi: 10.1109/AERO.2015.7118930.

Vilà-Valls, J., P. Closas, C. Fernández-Prades, and J. T. Curran (2018), On the Mitigation of Ionospheric Scintillation in Advanced GNSS Receivers, *IEEE Transactions on Aerospace and Electronic Systems*, 54(4), 1692-1708, 10.1109/TAES.2018.2798480.

Wang, J., and Y. Morton (2015), High-latitude ionospheric irregularity drift velocity estimation using spaced GPS receiver carrier phase time-frequency analysis, *IEEE Transactions on Geoscience and Remote Sensing*, Vol. 53, 6099-6113, doi: 10.1109/TGRS.2015.2432014.

Ward, P. W., J. W. Betz, and C. J. Hegarty (2005), GPS satellite signal acquisition and tracking, Chapter 5 in *Understanding GPS: Principles and Applications, 2nd edn*, 153-240, Artech House Publishers, Boston, US/London, UK.

Won, J. H., T. Pany, and B. Eissfeller (2012), Characteristics of Kalman filters for GNSS signal tracking loop, *IEEE Transactions on Aerospace and Electronic Systems*, 48(4), 3671–3681, doi: 10.1109/TAES.2012.6324756.

Xiong, C., C. Stolle, and H. Lühr (2016), The Swarm satellite loss of GPS signal and its relation to ionospheric plasma irregularities, *Space Weather*, 14(8), 563-577, doi: 10.1002/2016SW001439.

Xu, D., Y. Morton, and S. Taylor (2014), Algorithms and results of tracking BeiDou signals during strong ionospheric scintillation over Ascension Island, Proc. ION ITM, 730-735, San Diego, CA.

Xu, D., Y. Morton, D. Akos, and T. Walter (2015), GPS multi-frequency carrier phase characterization during strong equatorial ionospheric scintillation, Proc. ION GNSS+, 3787-3796, Tampa, FL.

Xu, D., and Y. Morton (2015), GPS carrier parameters characterization during strong equatorial ionospheric scintillation, Proc. ION ITM, 521-529, Dana Point, CA.

Xu, D., Y. Morton, Y. Jiao, and C. Rino (2017), Robust GPS carrier tracking algorithms during strong equatorial scintillation for dynamic platforms, Proc. ION GNSS+, 4112-4121, Portland, OR.

Xu, D., Y. Morton, Y. Jiao, and C. L. Rino (2018a), Simulation and tracking algorithm evaluation for scintillation signals on LEO satellites traveling inside the ionosphere, Proc. IEEE/ION PLANS, 1143-1150, Monterey, CA.

Xu, D., Y. Morton, Y. Jiao, C. Rino, and R. Yang (2018b), Implementation and Performance Evaluation of a Vector-based Receiver during Strong Equatorial Scintillation on Dynamic Platforms, Proc. ION GNSS+, 3611-3622, Miami, Florida.

Xu, D., and Y. Morton (2018), A Semi-Open Loop GNSS Carrier Tracking Algorithm for Monitoring Strong Equatorial Scintillation, *IEEE Transactions on Aerospace and Electronic Systems*, 54(2), 722-738, doi: 10.1109/TAES.2017.2764778.

Xu, D., Y. T. Morton, and R. Yang (2019a), A two-parameter multi-frequency GPS signal simulator for strong equatorial ionospheric scintillation: modeling and parameter characterization, submitted to *Navigation*.

Xu, D., Y. T. Morton, C. L. Rino, C. S. Carrano, and Y. Jiao (2019b), A comparative performance analysis of advanced GNSS carrier tracking algorithms during strong equatorial ionospheric scintillation, submitted to *IEEE Transactions on Aerospace and Electronic Systems*.

Yang, R., K. V. Ling E. K. Poh, and Y. Morton (2017a), Generalized GNSS signal carrier tracking: part I- modelling and analysis, *IEEE Transactions on Aerospace and Electronic Systems*, 53(4), 1781-1797, doi: 10.1109/TAES.2017.2673998.

Yang, R., Y. Morton, K. Ling, and E. Poh (2017b), Generalized GNSS signal carrier tracking - part II: optimization and implementation, *IEEE Transactions on Aerospace and Electronic Systems*, 53(4), 1798-1811, doi: 10.1109/TAES.2017.2674198.

Yang, R., D. Xu, and Y. Morton (2018), An improved adaptive multi-Frequency GPS carrier tracking algorithm for navigation in challenging environments, Proc. of IEEE/ION PLANS, 899-907, Monterey, CA.

Yang, R. D. Xu, and Y. Morton (2019), Generalized multi-frequency GPS carrier tracking architecture: design and performance analysis, submitted to *IEEE Transactions on Aerospace and Electronic Systems*.

Yeh, K. C., and C. H. Liu (1982), Radio wave scintillations in the ionosphere, *Proc. IEEE*, 70(4), 324-360, doi: 10.1109/PROC.1982.12313.

Yin, H., Y. Morton, and M. Carroll (2014), Implementation and performance analysis of a multi-frequency GPS signal tracking algorithm, Proc. ION GNSS+, 2747–2753, Tampa, FL.

Yin, H., Y. Morton, M. Carroll, and E. Vinande (2015), Performance analysis of L2 and L5 CNAV broadcast ephemeris for orbit calculation, *Navigation*, 62(2), 121-130, doi: 10.1002/navi.84.

Yue, X., W. S. Schreiner, Y. H. Kuo, J. J. Braun, Y. C. Lin, and W. Wan (2013). Observing system simulation experiment study on imaging the ionosphere by assimilating observations from ground GNSS, LEO-based radio occultation and ocean reflection, and cross link, *IEEE Transactions on Geoscience and Remote Sensing*, 52(7), 3759-3773, doi: 10.1109/TGRS.2013.2275753.

Yue X., W. S. Schreiner, N. M. Pedatella, and Y. H. Kuo (2016), Characterizing GPS radio occultation loss of lock due to ionospheric weather, *Space Weather*, 14(4), 285-299, doi: 10.1002/2015SW001340.

Zhang, L., Y. Morton, Q. Zhou, F. van Graas, and T. Beach (2010a), Characterization of GNSS signal parameters under ionosphere scintillation conditions using software-based tracking algorithms, Proc. IEEE/ION PLANS, 264-275, Indian Wells, CA.

Zhang, L., Y. Morton, and M. Miller (2010b), A variable gain adaptive Kalman filter-based GPS carrier tracking algorithm for ionosphere scintillation signals, Proc. ION GNSS, 3107-3114, Portland, OR.

Zhang, L., and Y. Morton (2013), GPS carrier phase spectrum estimation for ionospheric scintillation studies, *Navigation*, 60(2), 113-122, doi: 10.1002/navi.33.

APPENDIX: SIMULATOR PROGRAM CONFIGURATION AND EXECUTION

A MATLAB implementation of the two-parameter scintillation simulator presented in Chapter 3 can be downloaded from https://github.com/cu-sense-lab/gnss-scintillation-simulator_2-param. The program folder contains the .m file of function Main and the folder named ‘Libraries’. The ‘Libraries’ subfolder contains the supporting functions for function Main.

The user-input parameters to be specified are all included in Main.m:

- 1) Simulation start date and time in UTC;
- 2) Simulation length in seconds;
- 3) Satellite PRN number;
- 4) S_4 index and τ_0 ;
- 5) Platform position in latitude-longitude-height (LLH) coordinate and velocity vector in ENU coordinate; (To generate stationary scintillation data, simply assign the velocity vector to all zeros.)
- 6) Number of frequencies to be simulated: 1 – GPS L1 only || 2 – L1 and L2 || 3 – L1, L2, and L5;
- 7) Figure plotting switch; (If on, figures to be plotted include satellite sky plot, IPP LLH 3-D plot, simulated scintillation intensity and phase)

The variables for each input parameter are named in function Main in a self-explanatory manner and stored in the struct ‘userInput’. Comments are also provided above the value assignment of each variable to explain each variable and the correct input format. After specifying each parameter,

run the Main function, and the scintillation amplitude and phase time series of specified length with an update rate of 100Hz will be recorded in the variables 'Scin_amp' and 'Scin_phi'.

For Windows or Mac users, if the program reports an error during the function ExtractRINEXeph.m which downloads the RINEX ephemeris file and extracts ephemeris parameters for satellite orbit computation, simply go to the simulator program folder and unzip the downloaded brdc****.**n ephemeris file by hand and then rerun the program.